RIMS-1737

Asymptotic analysis of long-time behaviour of zonal flows in two-dimensional turbulence on a β plane

By

Kiori OBUSE

January 2012

京都大学　数理解析研究所

RESEARCH INSTITUTE FOR MATHEMATICAL SCIENCES

KYOTO UNIVERSITY, Kyoto, Japan

Asymptotic analysis of long-time behaviour of zonal flows in two-dimensional turbulence on a β plane

Kiori Obuse

Research Institute for Mathematical Sciences, Kyoto University

Abstract

In forced two-dimensional turbulence on a rotating sphere, it is well known that a multiple zonal-band structure, *i.e.* a structure with alternating eastward and westward jets, emerges in the course of time development. The multiple zonal-band structure then experiences intermittent mergers and disappearances of zonal jets, and a structure with only a few large-scale zonal jets is realised as an asymptotic state (Obuse *et al.*, 2010). With the view of understanding the long-time behaviour of the zonal jets in two-dimensional turbulence in rotating systems, we consider large-scale zonal flows superposed upon a homogeneous zonal flow and a small-scale sinusoidal transversal flow on a β plane, which is the model originally introduced by Manfroi and Young (1999), and investigate the merging and disappearing processes of zonal jets. First, we analytically obtain solutions of steady isolated zonal jet of the evolution equation of such zonal flows. Then it is shown that these steady zonal jet solutions are all linearly unstable. The numerical time integration of the evolution equation also confirms that the final state of a perturbed unstable steady solution is a uniform flow. These results suggest that mergers and disappearances of zonal jets in two-dimensional turbulence on β plane and on a rotating sphere might be due to the instability of the zonal jets caused by the effect of turbulence. Utilising the analytical solution of steady isolated zonal jet, the weak interaction between two neighbouring zonal jets is also studied. The time derivative of the distance between two identical zonal jets is estimated by a perturbation method, confirming that two zonal jets placed apart attract each other, and the attraction becomes stronger as the distance between them gets shorter. The estimated time derivative of the distance between two zonal jets is in agreement with that obtained from the numerical time integration of the evolution equation. It is also found by numerical simulation that the two zonal jets then merge to a new steady isolated zonal jet of different parameters. Because of the linear instability of the new steady zonal jet, the final state is expected to be a uniform flow. These results are consistent with gradual mergers and disappearances of zonal jets seen in forced two-dimensional turbulence on β plane and on a rotating sphere, and implies the importance of the weak interaction between neighbouring zonal jets for the long-time behaviour of zonal jets in forced two-dimensional turbulence in rotating systems. Finally, we modify the Manfroi-Young model by

taking account of the spatial variation of the disturbance in the zonal direction, and the surface variation of the fluid layer, in order to make the model a little more realistic. The linear stability analysis of analytical solutions of steady isolated zonal jet in these models suggests that the instability of zonal jets is widely common in turbulence on β plane.

Contents

1 Introduction **8**

2 Long-time asymptotic states of forced two-dimensional turbulence on a rotation sphere **14**
2.1 Introduction 14
2.2 Equation of motion and numerical method 15
2.3 Results of numerical experiments 19
2.3.1 Zonal-mean zonal angular momentum 19
2.3.2 Energy of zonal flow 23
2.3.3 The Rhines wavenumber 26
2.3.4 The total energy 29
2.3.5 Stream function 31
2.4 Stability of the 3-jet structure 33
2.5 Discussions and Conclusions 37

3 Asymptotic analysis of long-time development of zonal flow **39**
3.1 Introduction 39
3.2 Long-time behaviour of forced two-dimensional turbulence on a β plane 42
3.2.1 Equation of motion and numerical method 42
3.2.2 Results of numerical experiments 44
3.3 Weakly nonlinear model and its steady isolated jet solution . . 48
3.3.1 Model and the Manfroi-Young equation 48
3.3.2 Steady isolated zonal jet solution U_0 51
3.4 Disappearing processes of zonal jets – Linear stability of U_0 . . 58
3.4.1 Characteristic equation and eigenvalues 58
3.4.2 The analytical evaluation of the eigenvalues 63

3.4.3 The growth of an unstable eigenfunction and the final flow field 68
3.5 Merging processes of zonal jets – Weak interaction between two zonal jets 70
3.5.1 Estimation of a weak interaction between two zonal jets 70
3.5.2 Numerical evaluation of the time derivative of the distance between two zonal jets 75
3.5.3 Strongly nonlinear stage and the final state 77
3.6 Modifications to the Manfroi-Young model 82
3.6.1 Two-dimensional barotropic model; x-dependent case . 82
3.6.2 Quasi-Geostrophic model; x-independent case 88
3.6.3 Quasi-Geostrophic model; x-dependent case 94
3.7 Discussions and Conclusions 99

4 Conclusion **103**

Appendix **107**
A.1 Treatment of liner terms in the governing equation (2.1) in numerical calculations in §2 107
A.2 Convergence of the numerical calculations in §2 109
A.3 Treatment of liner terms in the governing equation (3.1) in numerical calculations in §3.2 111
A.4 Convergence of the numerical calculations in §3.2 113
A.5 Symmetry of the characteristic equation (3.38) 115
A.6 Linear stability of an uniform flow in a Manfroi-Young model . 117

Acknowledgements **118**

Bibliography **118**

List of Figures

2.1 Vorticity forcing field. 17
2.2 Temporal development ($t = 0 - 1000$) of zonal-mean zonal angular momentum $\overline{[L_{lon}]}$. 21
2.3 Long-time development of the zonal-mean zonal angular momentum $\overline{[L_{lon}]}$ 22
2.4 Temporal variation of spectral distribution of the energy of zonal flow $\langle \mathcal{E}_z \rangle$ in run 2. 23
2.5 Temporal variation of spectral distribution of the energy of zonal flow $\langle \mathcal{E}_z \rangle$. 25
2.6 Temporal variation of the Rhines wavenumber n_β and the characteristic wavenumber n_{mean}. 28
2.7 Temporal variation of spherical-mean energy $\langle \mathcal{E} \rangle$. 30
2.8 Stream function ψ and zonal velocity u_{lon} on a sphere at the final integral time. 32
2.9 Spectral distribution of the stream function at $t = 4.5 \times 10^5$ at in run 17. 33
2.10 Temporal development of zonal-mean zonal angular momentum $\overline{[L_{lon}]}$, started from perturbed 3-jet states. 35
2.11 Temporal variation of the spectral distribution of the stream function of a perturbed 3-jet state. 36

3.1 Vorticity forcing field. 43
3.2 Long-time development of the $x-$mean $x-$velocity $\overline{[u_x]}$. 45
3.3 Temporal variation of the Rhines wavenumber k_β and the characteristic wavenumber k_{mean}. 47
3.4 Examples of the shape of potential $V(U_0)$ which realises a steady isolated zonal jet solution U_0. 53
3.5 Regions of (γ, U_W) which realise steady isolated zonal jet solution U_0. 55

3.6 Examples of steady isolated zonal solutions with an eastward jet. 56
3.7 Real parts of leading eigenvalues. 61
3.8 Square roots of real part of leading eigenvalues. 62
3.9 Real parts of numerically calculated leading eigenvalues and analytically expected curves 65
3.10 Temporal variation of a perturbed steady isolated zonal jet solution U_0. 69
3.11 Examples of time derivative of the distance between two jets $\dot{h}_P$. 75
3.12 Two-jet state at $\tau = 0$ and $\tau = 20.0$. 77
3.13 Comparison between $\dot{h}_N$ and $\dot{h}_P$. 78
3.14 Strongly nonlinear stage and the final state of weakly-unstable case. 79
3.15 New steady isolated jet U_{0new} obtained after a merger of two zonal jets. 80
3.16 Strongly nonlinear stage and the final state of strongly-unstable case. 81
3.17 Real parts of leading eigenvalues. 87
3.18 Real parts of leading eigenvalues. 92
3.19 Real parts of leading eigenvalues. 93
3.20 Real parts of leading eigenvalues. 96
3.21 Real parts of leading eigenvalues. 98

A.1 Convergence of long-numerical calculation on a rotating sphere.110
A.2 Convergence of long-numerical calculation on a β plane. 114

List of Tables

2.1 Ω, n_f, $\| F \|$, and integration time in each run of long-time integrations on a rotating sphere. 18

Chapter 1

Introduction

Many studies on fluid dynamics in an irrotational system have been carried out in relation to fluid phenomena in daily life. The fluid dynamics in a rotating system is also attracting much interest in respect, for instance, of observations in geoscience and of environmental problems. In these areas, there are plenty of mathematical models with a wide range of complexity, in terms of the treatments of the physical processes. With the great progress in computer's performance these days, more and more realistic numerical simulations are performed by use of such complex models.

One of the features seen in a rotating system which has been attracted people's interest may be an existence and the robustness of multiple zonal-band structures, *i. e.*, a structure consists of alternating eastward and westward jets, observed on many giant planets. The atmosphere in a surface or in an outer shell of a planet is believed to be in turbulent state induced by, for example, a heat convection caused by an inner heating system or heat injection from the sun. A large-scale zonal-band structure is commonly observed and maintained for a very long time, almost keeping their shapes in many giant planets. The emergence of the multiple zonal-band structure is interesting not only because it may have emerged from and maintained in a perturbed small-scale flow filed, but also because it possesses a strong anisotropic structure.

One of the mainstream researches for the origin of the multiple zonal-band structure started from Busse [1], who argued that the structure is a surface manifestation of three-dimensional circulation deep inside of a planet. This appealing theory is difficult to prove though, especially because of the lack of the knowledge we have for the interior of a planet, and because of

the lack of computational power. Nevertheless many three-dimensional researches including heavy numerical calculations have been done (Sun *et al.* [2], Heimpel *et al.* [3]), and Busse's idea [1] is considered to be reasonable and possesses strong support in a wide area of geoscience these days. Unfortunately however, it is difficult to extract the essence of the physics in the complex mathematical models used there, and in fact, even the basic nature of simple mathematical models, being the foundation of such complex models, are not yet well understood.

A simpler model for the origin of multiple zonal-band structure was proposed by Rhines [4] with a pioneering numerical study of two-dimensional turbulence on a tangent plane of a rotating sphere with a linear approximation of Coriolis parameter with respect to the meridional direction ($y-$ coordinate), namely, a β plane. He found that a multiple zonal-band structure is built up as the turbulent motion evolves, and robustly maintained for quite a long time. The formation and the robustness of the multiple zonal-band structure was explained by introducing the Rhines scale, where the β effect, *i.e.* the effect of differential rotation, and the advective effect in the governing equation become comparable. It is well known that two-dimensional turbulence in an irrotational system is characterised by the inverse energy cascade (Kraichinan [5]), in contrast to the energy transfer to smaller-scale structure in three-dimensional system. The kinetic energy injected at small scales is then transferred to larger scales, which brings about a statistically isotropic larger-scale structure as time progresses. The β effect retards this inverse energy cascade at scales smaller than the Rhines scale, and causes the anisotropic zonal features whose width is roughly the same as the Rhines scale.

Many succeeding studies have confirmed the emergence of the multiple zonal-band structure on both β plane and two-dimensional sphere (Vallis and Maltrud [6], Williams[7]). The multiple zonal-band structure suggests many fascinating problems including the mechanism of energy's concentration to zonal jets (Chekhlov *et al.* [8], Huang and Robinson [9], Balk [10]), and the asymmetry of the eastward and westward jets' profiles. However, the long-time asymptotic state of zonal flows observed in two-dimensional turbulence in rotating systems is not yet fully known, and the physics of their long-time behaviour is not well understood, either.

Yoden and Yamada [11] investigated the long-time asymptotic states of freely decaying two-dimensional barotropic incompressible flows on a rotating sphere. Interestingly, the long-time asymptotic states are not necessarily

characterised by the multiple zonal-band structure but by strong westward circumpolar jets, which become prominent after long-time integration, although there remains weak multiple zonal-band structure in the low and middle latitudes. The scaling laws for this circumpolar jets are obtained by Takehiro *et al.* [12]; when the rotation rate of the sphere Ω increases, the strength of the jets increases as $\Omega^{\frac{1}{4}}$ and the width of the jets decreases as $\Omega^{-\frac{1}{4}}$.

On the other hand, for a forced two-dimensional barotropic incompressible flow on a two-dimensional sphere, Nozawa and Yoden [13] performed numerical simulations, with a Markovian random forcing of constant strength, of 18 cases with different combinations of a rotation rate of the sphere and a forcing wavenumber. There, they showed that the generated flow fields are characterised by a multiple zonal-band structure or a structure with westward circumpolar jets. They also pointed out that the two different structures arise according to the relative magnitude between the Rhines wavenumber (the inverse of the Rhines scale) of the flow and the forcing wavenumber, and also that when the forcing wavenumber is higher than the Rhines wavenumber, the inverse energy cascade continues until the characteristic wavenumber of the flow reaches around the Rhines wavenumber to form the multiple zonal-band structure; but when the forcing wavenumber is lower than the Rhines wavenumber, the inverse energy cascade hardly occurs, and the circumpolar jets appear as a result. In contrast, Huang *et al.* [14] performed simulations with a white noise forcing of constant energy input to the system, and obtained an asymptotic state consisting of zonal jets whose representative wavenumber is lower than the Rhines wavenumber. They then inferred that the Markovian random forcing in Nozawa and Yoden [13] may be regarded as a strong drag of low wavenumbers dissipation which maintains the formed multiple zonal-band structure.

A recent numerical experiment of forced two-dimensional turbulence on a rotating sphere shows, however, that when the time integration is carried much further than the previous studies, including Nozawa and Yoden [13], multiple zonal jets merge passing over the Rhines scale, and as a result, two or three large-scale alternating zonal jets remain at the final stage, even under the use of Markovian random forcing of constant strength (Obuse *et al.* [15]). This, together with the result of Huang *et al.* [14], suggests that the long-time asymptotic states of two-dimensional turbulence on a rotating sphere may be a structure with only two or three large-scale alternating zonal jets.

This result suggests that long-time behaviour of zonal flows on a rotating sphere is beyond Rhines' theory, and therefore the insight into the process of mergers and disappearances of zonal jets is essential when we consider the long-time behaviour of zonal jets in forced two-dimensional turbulence on a rotating sphere. Unfortunately, the process cannot be explained in a simple framework of laminar flows because of the linear stability of karge laminar zonal jets. As a consequence, it is inevitable to take the effect of turbulence into the theory for zonal jets in an analytically treatable way when we hope to understand the long-time behaviour of zonal jets on a rotating sphere and β plane.

One thing we have to notice here from the results of Huang *et al.* [14] and Obuse *et al.* [15] is that the two-dimensional model may not be very suitable for a planetary atmosphere because of the decrease of the number of zonal jets in its long-time evolution. Nevertheless, as this is one of the most fundamental models for planetary atmospheres, the insight of the basic nature of this model will bring a good understanding for more realistic models. Therefore, we clear out the idea of the applicability of this model to planetary atmosphere for a while, and treat it as one of the ideal mathematical models, and investigate its basic properties. Hence, this thesis is dedicated to the investigation of the long-time behaviour of forced two-dimensional barotropic incompressible flows on a rotating sphere.

A long-time behaviour of a large-scale flow, including structure with zonal jets, under the influence of small-scale turbulence is a fascinating and important subject to know, from the viewpoints of dynamics of planetary atmospheres and fluid dynamics. However, it contains great amount of difficulties in both analytical and numerical aspects. One of the strongest reasons for the difficulties may originates from the randomness and stochastic nature of the turbulence. There, the deterministic methods to forecast the future is powerless. Length of the time scale we need to deal with is also one of the factors of the difficulties when we hope to understand the long-time behaviour of the flow. Even an infinitesimal deviation from an assumed state, caused from the randomness of the turbulence or numerical errors, can be critical since the small deviation may grow to make the flow filed completely different. In addition to these factors, the spherical geometry of the domain, the existence of curvature and north and south poles for instance, makes the analytical treatment of the problem more complicated.

To avoid the difficulties stated above, we assume a small-scale deterministic forcing instead of a stochastic forcing, and also utilise β-plane ap-

proximation in the main part of this thesis. We consider a situation that large-scale zonal flows are superposed upon a deterministic small-scale sinusoidally transversal background base flow on an infinite β plane, where the flow is confined in a plane with no curvature, and where the Coriolis parameter is approximated linearly with respect to the meridional direction ($y-$coordinate).

Zonal flows superposed upon a small-scale deterministic non-zonal background base flow was originally considered by Manfroi and Young [16]. They have considered the situation where homogeneous zonal flow and a small-scale sinusoidal transversal steady flow are realised as a base flow under the existence of a suitable forcing. Then assuming the Reynolds number of the flow to be slightly larger than the critical Reynolds number, *i. e.* the situation where the base flow is slightly unstable, they considered a time evolution of a large-scale zonal disturbance flow. The model contains the interaction between the zonal disturbance flows and the background non-zonal flow, and therefore treating a weakly nonlinear theory. Manfroi and Young [16] derived the time evolution amplitude equation of the zonal flows by employing a multiple-scale expansion technique. This equation is a special case of Cahn-Hilliard equation [17], and we call it the Manfroi-Young equation for clarity. In numerical experiments of the Manfroi-Young equation, when the bottom drag is absent, a multiple zonal-band structure emerges, and then the gradual disappearances of the zonal jet occur one by one, forming a thin eastward jet and a broad westward jet in the considered periodic domain (Manfroi and Young [16]). They also pointed out that the structure with one set of alternating zonal jets is the final state, by using a Lyapunov functional analysis. Since the evolution of the zonal-band structure seen in their numerical experiment is similar to long-time behaviour of zonal jets on a rotating sphere mentioned above, we may deduce some physical insight about the dynamics of zonal flows induced by small-scale stochastic forcing by examining the system derived by Manfroi and Young more precisely. Therefore in the main part of this thesis, by utilising an analytical solution of steady isolated zonal jet of the Manfroi-Young equation, we investigate the merging and disappearing processes observed on a rotating sphere and on β plane.

In this thesis, first we summarise the results of long-time asymptotic states of forced two-dimensional barotropic incompressible turbulence obtained in Obuse *et al.* in §2. There, mergers and disappearances of zonal jets are observed as one of the most the outstanding properties of long-time behaviour of zonal flow. Then in §3, we investigate the merging and dis-

appearing processes by utilising the Manfroi-Young model. Showing that the merging and disappearing processes are also observed as an outstanding property of long-time behaviour of forced two-dimensional turbulence on β plane in §3.2, we give a brief derivation of the Manfroi-Young equation, and then analytically derive its steady isolated zonal jet solutions in §3.3. The disappearing process of zonal jets seen in a Manfroi and Young's numerical experiment and in forced two-dimensional turbulence both on β plane and on rotating sphere, is discussed by examining the linear stability of steady isolated zonal jet solutions and their nonlinear time evolution in §3.4. The Merging process of zonal jets seen in forced two-dimensional turbulence both on β plane and on a rotating sphere, on the other hand, is investigated by considering the weak interaction between two steady isolated zonal jet solutions placed apart (two-jet state) in §3.5. There, the time derivative of the distance between two zonal jets is estimated by a perturbation method and compared with that obtained from a numerical time integration of Manfroi-Young equation, and then the final state of the two-jet state is numerically examined. Finally in §3.6, we modify the Manfroi-Young model by taking account of the spatial variation of the disturbance in the zonal direction, and the surface variation of the fluid layer, in order to make the models a little more realistic, and examine the linear stability of steady isolated zonal jets in these models. In §3.7, discussions and conclusions are given.

Chapter 2

Long-time asymptotic states of forced two-dimensional turbulence on a rotation sphere

[1]

2.1 Introduction

A Larger-scale flow on a planet is often treated as two-dimensional flow because of the effect of the rotation of the planet and a stratification of the fluid. Forced two-dimensional barotropic incompressible flow on a rotating sphere is one of the most basic models used under such assumption. However, in rotating systems, even the basic properties of simple mathematical models is not necessarily clear. One of such unclear characteristics is a long-time asymptotic state of the system, which is one of the most interesting properties from the viewpoints of dynamics of planetary atmospheres and fluid dynamics. Although a great deal of study have been carried out in order to investigate a long-time asymptotic state of a forced two-dimensional barotropic incompressible flow on a rotating sphere, as discussed in §1, it is not yet well clarified. One of the biggest reasons for this is that numerical time integrations of the previous studies seem not to be long enough to obtain long-time asymptotic states. Therefore, in this chapter, by following the

[1]Published in Obuse *et al.* [15]

settings of Nozawa and Yoden [13], which is one of the most systematic studies of the asymptotic states, we reexamine the long-time asymptotic states of two-dimensional barotropic incompressible flows on a rotating sphere with a small-scale, homogeneous, isotropic, and Markovian random forcing to certify the asymptotic state, the outstanding properties of long-time behaviour of zonal flows, and whether the dependence of the settings of the forcing exists.

2.2 Equation of motion and numerical method

The model equation considered in here is a non-dimensionalised vorticity equation for a forced two-dimensional barotropic incompressible flow on a rotating sphere, given in longitude ϕ and sine latitude μ : [2]

$$\frac{\partial \zeta}{\partial t} + J(\psi, \zeta) + 2\Omega \frac{\partial \psi}{\partial \phi} = F + \nu \left(\nabla^2 + 2\right) \zeta. \tag{2.1}$$

Here, t is time, ψ is the stream function and $\zeta \equiv \nabla^2 \psi$ is the vorticity, where ∇^2 is the horizontal Laplacian on a sphere. Ω is a dimensionless constant rotation rate of the sphere, ν is the dimensionless kinematic viscosity coefficient, and $F = F(\phi, \mu, t)$ is the vorticity forcing function. $J(A, B)$ is the Jacobian operator: $J(A, B) \equiv (\partial A/\partial\phi)(\partial B/\partial\mu) - (\partial A/\partial\mu)(\partial B/\partial\phi)$. The term $2\nu\zeta$ in the viscosity term is necessary for the conservation of total angular momentum of the system, as discussed in, for example, Silberman [18].

The vorticity forcing function F is taken to be the same as that in Nozawa and Yoden [13]; small-scale, homogeneous, isotropic, Markovian random function is given by

$$F(\phi, \mu, j\Delta t) = RF(\phi, \mu, (j-1)\Delta t) + \sqrt{(1-R^2)}\hat{F}(\phi, \mu, j\Delta t), \tag{2.2}$$

where Δt is the time step interval, j is the number of time steps, and $R = 0.982$ is the memory coefficient. $\hat{F}$ is a random vorticity source generated at

[2] In the case of Jovian atmosphere, Eq.(2.1) has been obtained $a_J = 7.00 \times 10^7$ m, as length scale and one Jovian day, 1J.day $= 3.57 \times 10^4$ sec, as time scale, and thus the non-dimensional rotation rate is $\Omega_J = 2\pi$.

each time step as

$$\hat{F}(\phi,\mu,j\Delta t)=\sum_{n=n_f-\Delta n}^{n_f+\Delta n}\sum_{\substack{m=-n\\ m\neq 0}}^{n}\hat{F_n^m}(j)Y_n^m(\phi,\mu), \tag{2.3}$$

where $\hat{F_n^m}$ is the expansion coefficient of $\hat{F}$ and Y_n^m is the spherical harmonic with total wavenumber n and zonal wavenumber m. The phase of $\hat{F_n^m}$ $(m\geq 0)$ are random and uniformly distributed on $[0,\ 2\pi]$. The amplitude of $\hat{F_n^m}$ $(m\geq 0)$ are also random with $\parallel F \parallel=\sqrt{\langle\hat{F}^2\rangle}$ being a prescribed value, where $\langle\cdots\rangle$ denotes the spherical mean. Then $\hat{F_n^{-m}}$ $(m>0)$ are the complex conjugate of $\hat{F_n^m}$ $(m>0)$, since $\hat{F}$ is real. This vorticity forcing is given in a narrow band in the wavenumber space: $n_f-\Delta n\leq n\leq n_f+\Delta n$ with $\Delta n=2$. Fig.2.1 shows the examples of the vorticity forcing fields with $n_f=20, 40,$ and 79 and $\Delta t=0.05$.

For numerical calculations, the parameters in the governing equation (2.1) are all set equal to those used in Nozawa and Yoden [13]. The kinematic viscosity coefficient is $\nu=3.46\times 10^{-6}$. The rotation rate of the sphere Ω takes five different values; $\Omega/\Omega_J=0.25,\ 0.5,\ 1.0,\ 2.0,$ and $4.0,$ with $\Omega_J\equiv 2\pi$. The central total wavenumber of the forcing n_f takes three different values $n_f=20, 40,$ and 79, and for each of n_f, the rms amplitude of $\hat{F}$ *i.e.* $\parallel F \parallel$ is given as shown in table 2.1 [3].

A spectral method with the spherical harmonics is used for the calculation. The stream function ψ is expanded as

$$\begin{aligned}\psi(\phi,\mu,t)&=\sum_{n=0}^{N_T}\sum_{m=-n}^{n}\psi_n^m(t)Y_n^m(\phi,\mu)\\ &=\sum_{n=0}^{N_T}\sum_{m=-n}^{n}\psi_n^m(t)P_n^m(\mu)\exp(im\phi).\end{aligned}$$

Here, ψ_n^m is the expansion coefficient. We set the truncation wavenumber to be $N_T=199$, then we take 600 and 300 spatial grid points in longitudinal

[3] As Nozawa and Yoden [13] used different normalising coefficients of the spherical harmonics for vorticity forcing from those for other variables, $\parallel F \parallel$ has to correspond to the value $\sqrt{2}$ times larger than those used in Nozawa and Yoden [13] in our calculation using the same normalising coefficients for all variables. We greatly thank Dr. Nozawa for having kindly shown us his simulation code.

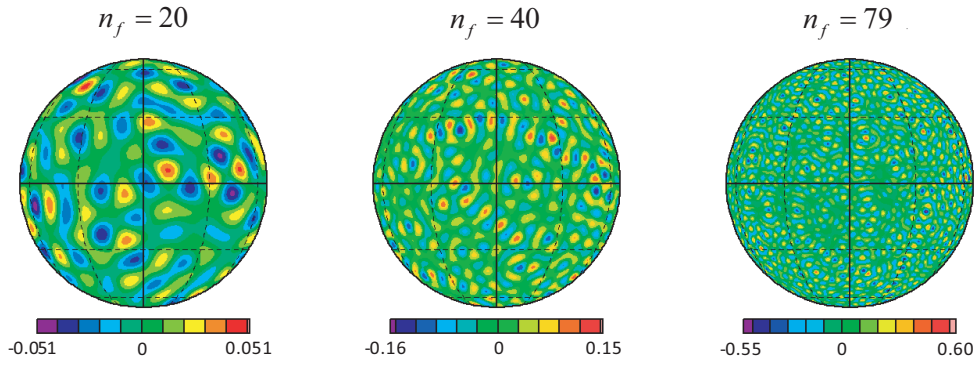

Figure 2.1: Vorticity forcing field at dimensionless time $t = 1000$. n_f of the left, the middle and the right panels are $20, 40,$ and 79, respectively. The top of the sphere, the bottom of the sphere, and the centre line correspond to the North Pole (90° N), the South Pole (90° S), and the equator, respectively.

and latitudinal direction, which are sufficiently large to eliminate the aliasing errors. Linear terms in the governing equation are analytically treated by using exponential function (See §A.1). The time integration is performed with the 4th order Runge-Kutta method with a time step $\Delta t = 0.05$ from the initial condition $\zeta = 0$. The integration time is extended to about 100 to 500 times of that of Nozawa and Yoden [13](table 2.1). With the conditions above, 15 simulations with different combinations of Ω and n_f (table 2.1) are performed [4] Note that the run numbers are $2-6$, $8-12$, and $14-18$, which keep the numbering correspondence between the simulations of Nozawa and Yoden [13] and ours.

[4]The convergence of the numerical simulations in this section has been checked by performing calculations with different parameters; $\Delta t = 0.025$, which is half of the one used here; the truncation wavenumber $N_T = 341$ and the spatial grid points 1024×512 which realise almost twice higher resolution than the one here. See §A.2

Table 2.1: Ω, n_f, $\| F \|$, and integration time in each run. Run numbers correspond to those in Nozawa and Yoden [13].

run number	Ω	n_f	$\| F \|$	integration time
2	$0.5\ \pi$			1.0×10^5
3	π			1.0×10^5
4	$2\ \pi$	20	1.412×10^{-2}	1×10^5
5	$4\ \pi$			1.0×10^5
6	$8\ \pi$			1.0×10^5
8	$0.5\ \pi$			1.0×10^5
9	π			1.0×10^5
10	$2\ \pi$	40	3.929×10^{-2}	1.2×10^5
11	$4\ \pi$			2.5×10^5
12	$8\ \pi$			1.6×10^5
14	$0.5\ \pi$			1.0×10^5
15	π			1.0×10^5
16	$2\ \pi$	79	1.415×10^{-1}	5.3×10^5
17	$4\ \pi$			5.2×10^5
18	$8\ \pi$			5.7×10^5

2.3 Results of numerical experiments

2.3.1 Zonal-mean zonal angular momentum

We first observe temporal development of zonal-mean zonal angular momentum $\overline{[L_{lon}]}$ in $0 \leq t \leq 1000$. Here, $\overline{[\cdots]}$ denotes the zonal mean, and $\overline{[L_{lon}]}$ is given by

$$\overline{[L_{lon}]} \equiv \frac{1}{2\pi}\int_0^{2\pi} u_{lon}\ \sqrt{1-\mu^2}\ d\phi,$$

where $u_{lon} = -\sqrt{1-\mu^2}\,(\partial\psi/\partial\mu)$ is the longitudinal component of velocity.

Fig.2.2 corresponds to the main result of Nozawa and Yoden [13], who discussed the flow pattern by using the numerical integration from $t = 0$ to 1000. On runs $2, 3, 8-11$, and $14-18$, a structure with alternating eastward and westward zonal jets, which we call a multiple zonal-band structure, is formed, while westward circumpolar jets and the weak eastward flow at low − mid latitude appear on runs $4-6$, and 12. These results are in agreement with those of Nozawa and Yoden [13].

Then we continue the time integrations further to $t = 1.0 \times 10^5$ or more, which is at least 100 times as long as the integration time in Nozawa and Yoden [13]. Fig.2.3 shows the temporal development of zonal-mean zonal angular momentum $\overline{[L_{lon}]}$. It is apparent that, in all cases, in spite of the classification made at $t = 1000$ by Nozawa and Yoden [13], a multiple zonal-band structure appears in the course of time development, and then enters a quasi-steady state with little change in its flow pattern, followed by a sudden merger and disappearance of the jets. In most cases, two prograde jets merge and a retrograde jet between the two prograde jets disappears. At the final stage of the time integration, a zonal-band structure with only a few broad zonal jets is realised; two jets remain in runs $2-6, 8-12, 14$and 15, and three jets in runs $16-18$. The structure with two broad jets, which consists of a eastward and a westward jets, shows no correlation with whether the eastward jet covers the Northern hemisphere or the Southern hemisphere.

There is a tendency that the integration time needed to reach the structure with a few zonal jets becomes longer as the forcing wavenumber n_f becomes higher and the rotation rate Ω becomes larger. For example, when $n_f = 20$, the case with $\Omega = 4\pi$ (run 5) and the case with $\Omega = 8\pi$ (run 6) require 4×10^4 and 8×10^4 dimensionless time to get to the structure with 2 broad jets respectively. Also for instance, when $\Omega = 4\pi$, the case with $n_f = 20$ (run5) , 40 (run 11) require $4 \times 10^4, 2 \times 10^5$ dimensionless time to

form the structures with two broad jets, and the case $n_f = 79$ (run 17) takes 3×10^5 dimensionless time even to get to the structure with three broad jets.

It is interesting to note that, in most of the cases, eastward jets merge whilst a westward jet disappears. In the process of the merger and disappearance of the jets, only one of the two merging jets becomes very strong and intrudes into the other, intercepting the development of the middle jet.

It is widely known, when the state is still with a multiple zonal-band structure, there exist significant asymmetries between eastward and westward jets in terms of their strength and width. Nevertheless, at sufficiently large time, there are no apparent asymmetries between the two (or three) broad jets.

The structure with two broad zonal jets is one of the long-time asymptotic states of the system. The inverse cascade does not proceed any more, and the two zonal jets cannot merge to one zonal jet because of the conservation law of the total angular momentum of the system. Therefore, according to our numerical results, the asymptotic states of the flow in runs $2-6, 8-12, 14$, and 15 consists of two broad zonal jets dominating over the whole sphere. On the other hand, the final states in runs $16, 17$, and 18 consists of three broad zonal jets, but it is not clear whether or not the three jets further merge or disappear at a later time. This will be discussed again in §2.4.

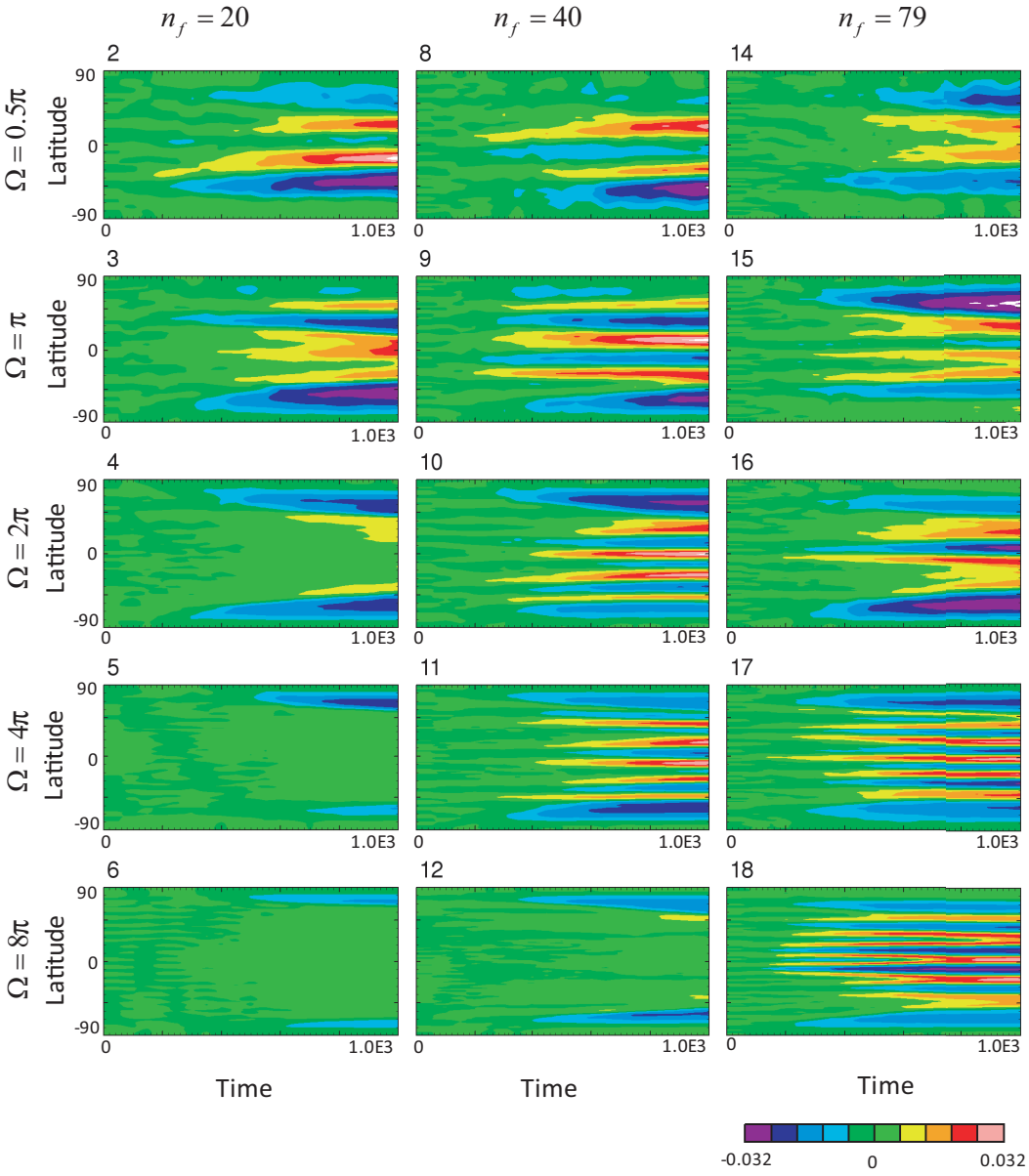

Figure 2.2: Temporal development ($t = 0-1000$) of zonal-mean zonal angular momentum $\overline{[L_{lon}]}$. The horizontal and the vertical axes in each panel are time and latitude in linear scale, respectively. This corresponds to Fig.3 in Nozawa and Yoden [13]

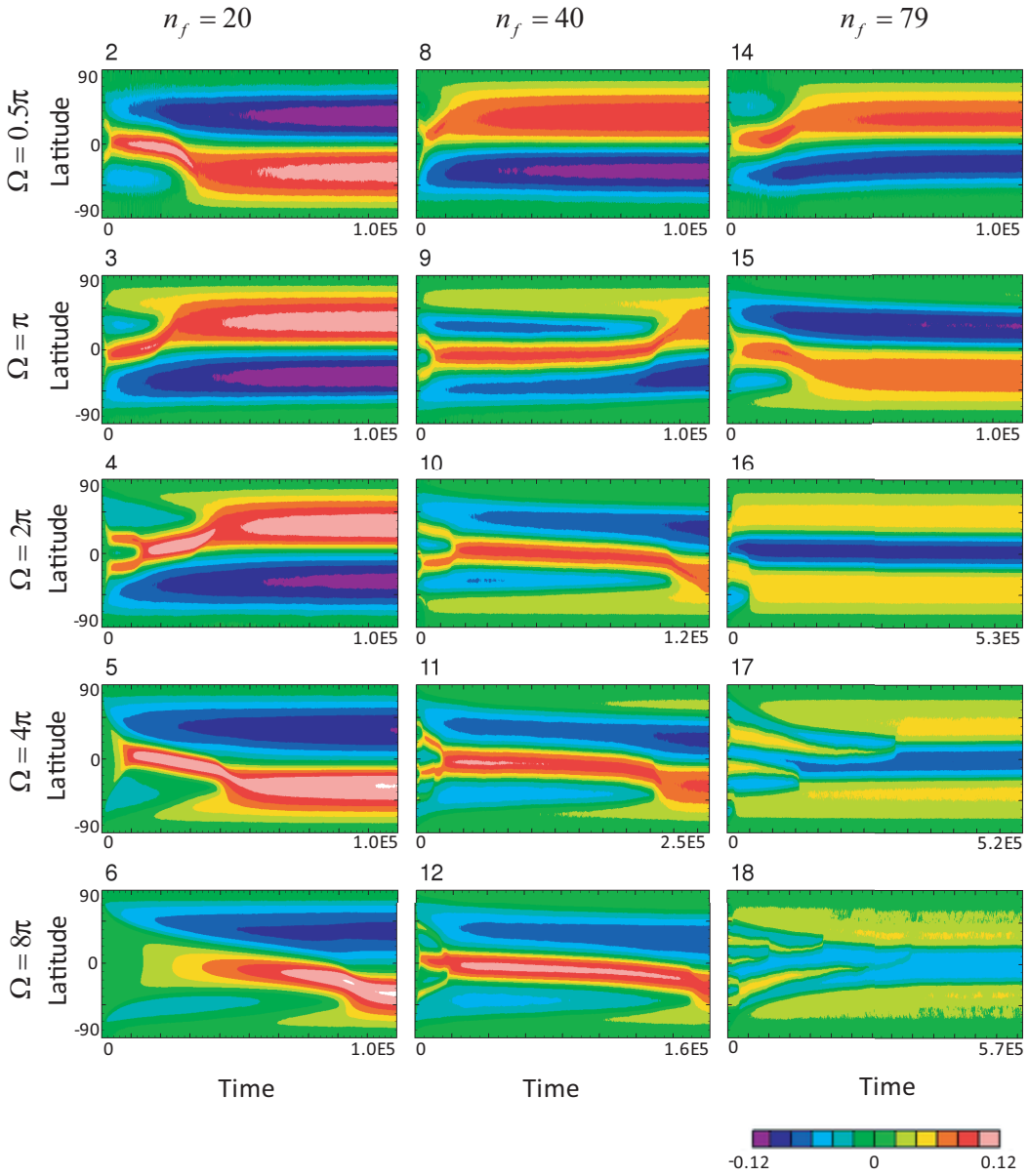

Figure 2.3: Long-time development of the zonal-mean zonal angular momentum $[\overline{L_{lon}}]$. The horizontal and the vertical axes in each panel are time and latitude in linear scale, respectively. The temporal integrations have been performed $t = 0 - 1 \times 10^5$ in runs $2 - 6, 8, 9, 14$, and 15, $t = 0 - 1.2 \times 10^5$ in run 10, $t = 0 - 2.5 \times 10^5$ in run 11, $t = 0 - 1.6 \times 10^5$ in run 12, $t = 0 - 5.3 \times 10^5$ in run 16, $t = 0 - 5.2 \times 10^5$ in run 17, and $t = 0 - 5.7 \times 10^5$ in run 18.

2.3.2 Energy of zonal flow

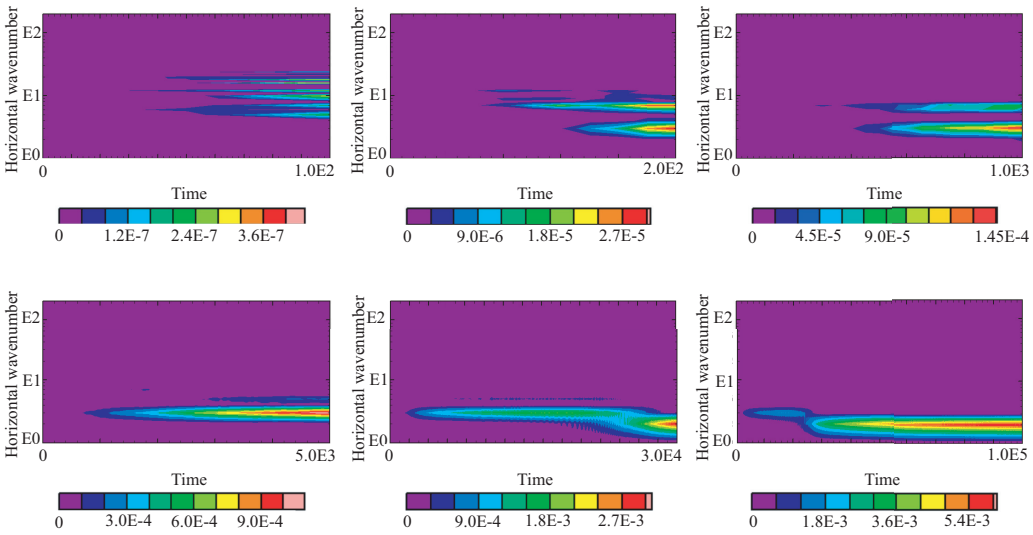

Figure 2.4: Temporal variation of spectral distribution of the energy of zonal flow $\langle \mathcal{E}_z \rangle$ in run 2. The horizontal and the vertical axes in each panel are time in linear scale and the total wavenumber n in log scale, respectively. The left, the middle, and the right panels in the upper row show the integrations $t = 0 - 100, 500$, and 1000 respectively. The left, the middle, and the right panels in the lower row show the integrations $t = 0 - 5 \times 10^3, 3 \times 10^4$, and 1×10^5 respectively.

The details of the formation of a structure with a few zonal jets is observed in the temporal variation of the spectral distribution of the energy of zonal flow

$$\langle \mathcal{E}_z(n,t) \rangle \equiv \frac{1}{2} n(n+1) \ |\psi_n^0(t)|^2$$

Note that the total wavenumber n of the stream function corresponds to the number of the zonal jets. For instance, from the temporal development of $\langle \mathcal{E}_z \rangle$ in run 2 (Fig.2.4), it is confirmed that at an early stage of the time integration ($t \sim 100$), wavenumbers around the forcing wavenumber ($n_f = 20$) mainly possess the zonal energy. The energy-containing wavenumbers then decrease, and at $t \sim 500$, the total wavenumbers $n = 3$ and 7 mainly possess the zonal

energy. At $t \sim 1000$, the zonal energy at $n = 3$ is the strongest, and this state remains stable until $t \sim 2.4 \times 10^4$, when most of the zonal energy speedily cascade to $n = 2$. The temporal variations of $\langle \mathcal{E}_z \rangle$ from $t = 0$ to the final integral times in all runs are shown in Fig.2.5, where the colour is in such a way that the final stage of the energy transfer is stressed. Although energy-containing wavenumbers experience a long quasi-steady period at $n \geq 3$, they resume to transfer the energy to lower wavenumbers and eventually reach to 2 (runs $2-6, 8-12, 14,$ and 15) or 3 (run 16). The energy transfer to lower n is not clearly seen in runs 17 and 18 as $\langle \mathcal{E}_z \rangle$ is very weak compared to other runs.

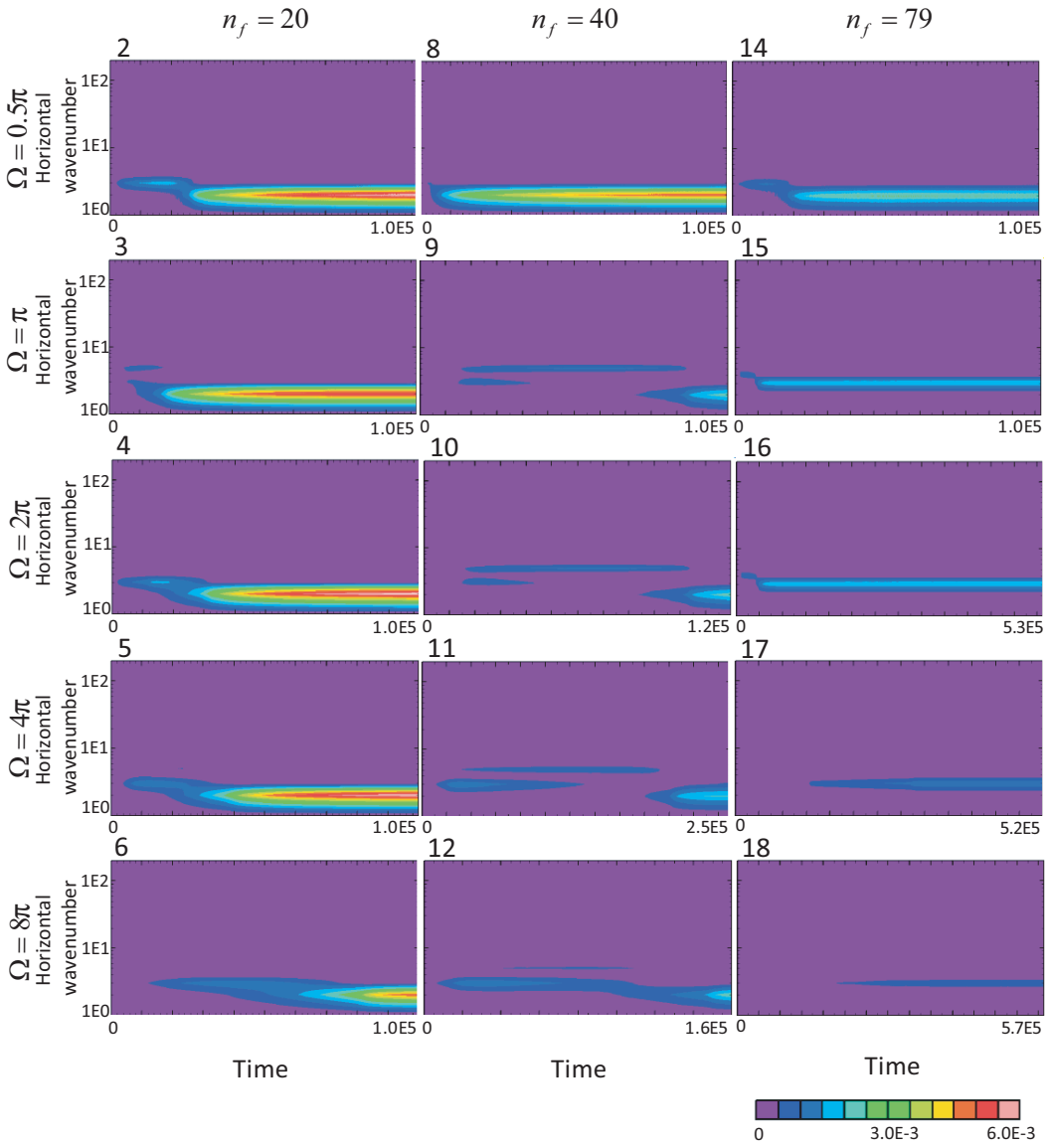

Figure 2.5: Temporal variation of spectral distribution of the energy of zonal flow $\langle \mathcal{E}_z \rangle$. The horizontal and the vertical axes in each panel are time in linear scale and the total wavenumber n in log scale, respectively. The temporal integrations have been performed $t = 0 - 1 \times 10^5$ in runs $2-6, 8, 9, 14$, and 15, $t = 0 - 1.2 \times 10^5$ in run 10, $t = 0 - 2.5 \times 10^5$ in run 11, $t = 0 - 1.6 \times 10^5$ in run 12, $t = 0 - 5.3 \times 10^5$ in run 16, $t = 0 - 5.2 \times 10^5$ in run 17, and $t = 0 - 5.7 \times 10^5$ in run 18.

2.3.3 The Rhines wavenumber

In Nozawa and Yoden [13], the main total wavenumbers n of the energy of the zonal flow $\langle \mathcal{E}_z \rangle$ spread over a quite wide range $2 \lesssim n \lesssim n_\beta$ at $t = 1000$, where n_β is the Rhines wavenumber. Since, in all runs, the inverse energy cascades proceed further than those in Nozawa and Yoden [13], we examine the temporal change of the Rhines wavenumber n_β on a sphere which is defined by

$$n_\beta(t) \equiv \sqrt{\frac{\langle \beta \rangle}{2U_{rms}(t)}}. \tag{2.4}$$

Here, $U_{rms}(t)$ is the rms velocity of the fluid:

$$U_{rms}(t) \equiv \sqrt{2\mathcal{E}(t)},$$

and $\langle \beta \rangle = \pi\Omega/2$ denotes the spherical mean of β, the latitudinal gradient of the Coriolis parameter. Also, we define the energy-weighted mean total wavenumber n_{mean} as the characteristic total wavenumber of the flow;

$$n_{mean}(n,t) \equiv \frac{\sum_{n=1}^{N_T} n\langle \mathcal{E}_{tot}(n,t) \rangle}{\sum_{n=1}^{N_T} \langle \mathcal{E}_{tot}(n,t) \rangle},$$

where $\langle \mathcal{E}_{tot} \rangle$ is given by

$$\langle \mathcal{E}_{tot}(n,t) \rangle \equiv \frac{1}{2} \sum_{m=-n}^{n} n(n+1)|\psi_n^m(t)|^2,$$

which means the energy at the total wavenumber n.

The temporal variation of n_β and n_{mean} is shown in Fig.2.6. The characteristic wavenumber n_{mean} becomes lower than the Rhines wavenumber n_β in a very early stage of the time integration (before $t = 1000$) and decreases to reach finally a fairly low wavenumber (2 to 6) at the final stage. Note that n_{mean} does not reach 2 precisely even when the fully developed two broad jets are dominating over the sphere.

The above results suggest that the inverse energy cascade or the energy transfer to lower wavenumbers continues even when $n_{mean} < n_\beta$, for the flow

field finally to consist of only a few (two or three) broad zonal jets. This also suggests that the Rhines wavenumber does not give an estimation of the characteristic wavenumber of the asymptotic flow field.

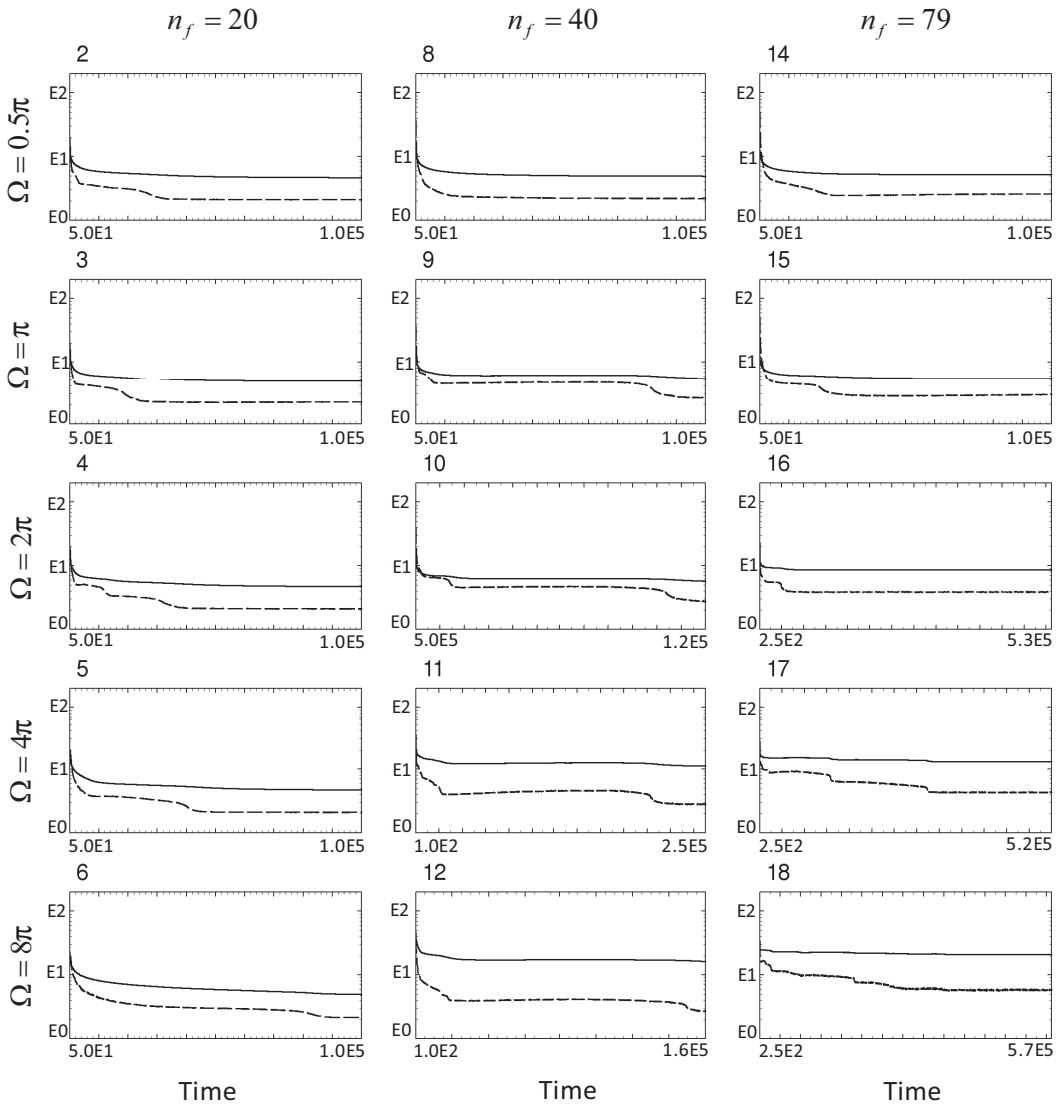

Figure 2.6: Temporal variation of the Rhines wavenumber n_β (solid line) and the characteristic wavenumber n_{mean} (dashed line). The horizontal and the vertical axes in each panel are time in linear scale and the Rhines wavenumber and the mean wavenumber in log scale, respectively. Note that both n_β and n_{mean} are infinity at $t = 0$ because $\mathcal{E}(0) = \langle \mathcal{E}_{tot}(0) \rangle 0$. The temporal integrations have been performed $t = 0 - 1 \times 10^5$ in runs $2-6, 8, 9, 14,$ and 15, $t = 0 - 1.2 \times 10^5$ in run 10, $t = 0 - 2.5 \times 10^5$ in run 11, $t = 0 - 1.6 \times 10^5$ in run 12, $t = 0 - 5.3 \times 10^5$ in run 16, $t = 0 - 5.2 \times 10^5$ in run 17, and $t = 0 - 5.7 \times 10^5$ in run 18.

2.3.4 The total energy

Fig.2.7 shows the temporal variation of the spherical-mean energy,

$$\begin{aligned} \langle \mathcal{E}(t) \rangle &\equiv \frac{1}{4\pi} \int_0^{2\pi} \int_{-1}^{1} \frac{u_{lon}^2 + u_{lat}^2}{2} \, d\mu \, d\phi \\ &= \frac{1}{2} \sum_{n=0}^{N_T} \sum_{m=-n}^{n} n(n+1) \, |\psi_n^m(t)|^2, \end{aligned} \tag{2.5}$$

where N_T is the truncation wavenumber. The most impressive feature is the stepwise increase of $\langle \mathcal{E} \rangle$ seen in runs $9-12$, and $15-18$. As Huang *et al.* [14] pointed out, $\langle \mathcal{E} \rangle$ experiences quasi-steady states with no apparent energy increase in these runs. However, the quasi-steady state is followed by a sudden increase of energy (except the last stairs in runs $16-18$). This implies that the standstill of the energy increase is not an effective sign of the realisation of an asymptotic state. It is interesting that the temporal variation of energy and the temporal development of jets have almost perfect correspondence in two aspects; the period in which the energy shows little increase coincides with the period in which the number of the jets remains constant; the time when the energy suddenly restarts increasing coincides with the time when the jets suddenly merge/disappear [5]. On the other hand, in runs $2-6, 8$, and 14, where the zonal-mean zonal angular momentum $\overline{[L_{lon}]}$ shows a gradual formation of two broad jets in Fig.2.3, $\langle \mathcal{E} \rangle$ also increase gradually, and the stepwise behaviour is not observed. These results imply that the merger and disappearance of jets bring about the energy increase.

Concerning the asymptotic states of the flow, in the run where two broad jets are finally formed (runs $2-6, 8-12, 14$, and 15), we can see a tendency that after the two broad jets are formed, $\langle \mathcal{E} \rangle$ keeps increasing for a while, and then slowly relaxes. This implies that it is still not obvious whether the 3-jet state at its final integral time in runs $16-18$ is the asymptotic state, or still a transient state before the next merger and disappearance.

[5] We note that this correspondence is also found in the temporal variation of the characteristic wavenumber n_{mean} in Fig.2.6.

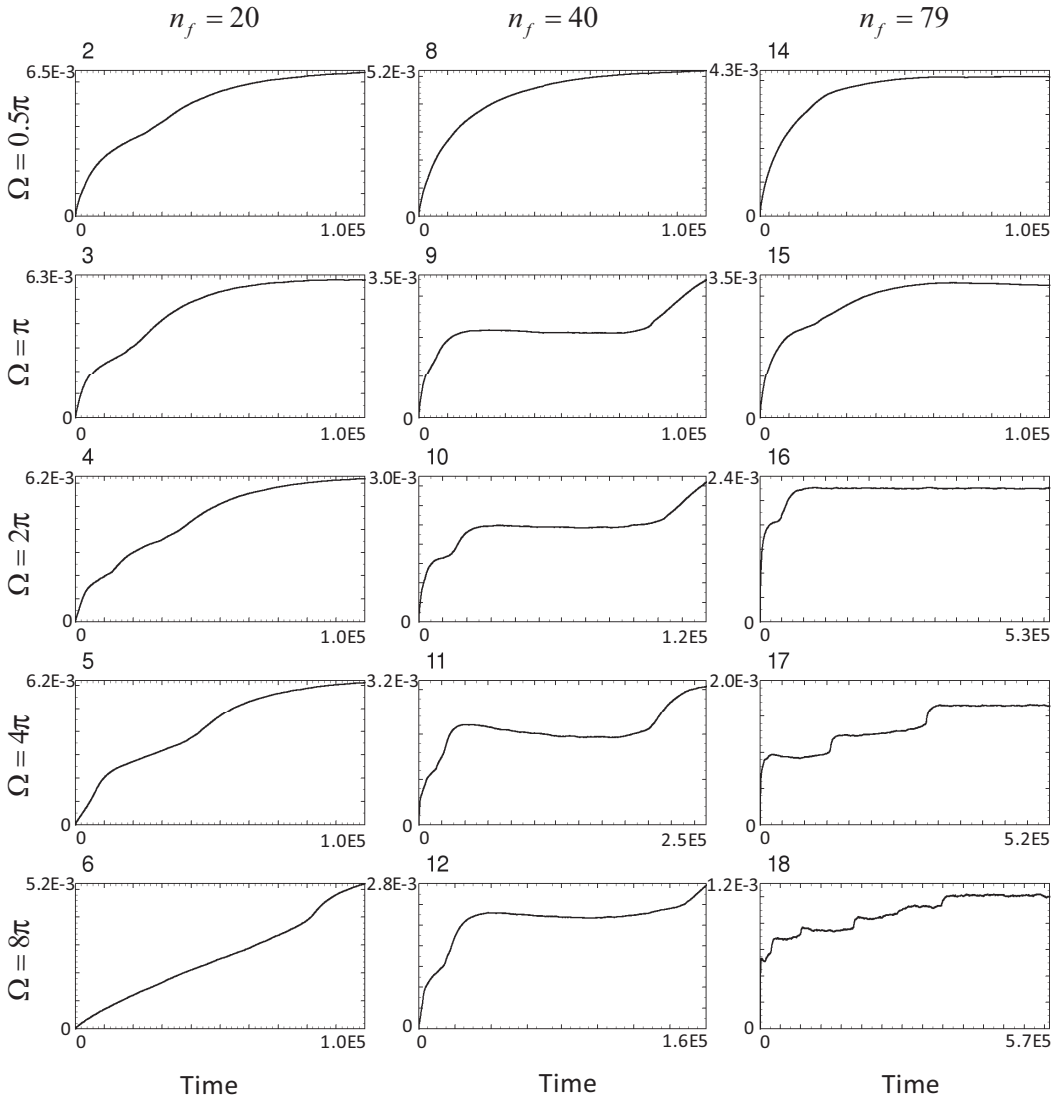

Figure 2.7: Temporal variation of spherical-mean energy $\langle \mathcal{E} \rangle$. The horizontal and the vertical axes in each panel are time and the energy in linear scale, respectively. The temporal integrations have been performed $t = 0 - 1 \times 10^5$ in runs $2 - 6, 8, 9, 14$, and 15, $t = 0 - 1.2 \times 10^5$ in run 10, $t = 0 - 2.5 \times 10^5$ in run 11, $t = 0 - 1.6 \times 10^5$ in run 12, $t = 0 - 5.3 \times 10^5$ in run 16, $t = 0 - 5.2 \times 10^5$ in run 17, and $t = 0 - 5.7 \times 10^5$ in run 18.

2.3.5 Stream function

Lastly, we observe the stream function and the zonal velocity on the sphere. In all runs, the zonal flow structure becomes dominant from an early stage of time development. At around the time of the appearance of the zonal-band structure in Fig.2.3, the structure with alternating rather eastward and westward flows are already formed on a sphere (not shown). As time goes on, these flows become more zonal undergoing their mergers and disappearances, and fairly zonal flows have been formed by the final integration times in most of runs (Fig.2.8), though some large-scale and non-zonal equatorial flows, which are spoiling the zonal flows, are seen (runs $2, 8,$ and 14), and there are several small non-zonal flows in the regions between the eastward and the westward flows (runs 15 and 16). The early emergence of the zonal-band structure and the realisation of the asymptotic with fewer zonal jets through the mergers and disappearances of the jets may tempt us to interpret the mergers and disappearances of the jets as a consequence of a barotropic instability of them. However, it should be remarked that, as pointed out by Rhines[4], a laminar zonal jet with a meridional scale larger than the Rhines scale is linearly stable owing to Rayleigh's condition. Therefore, non-zonal flows superimposed on the zonal jets appear to be necessary for the merger and disappearance of the jets.

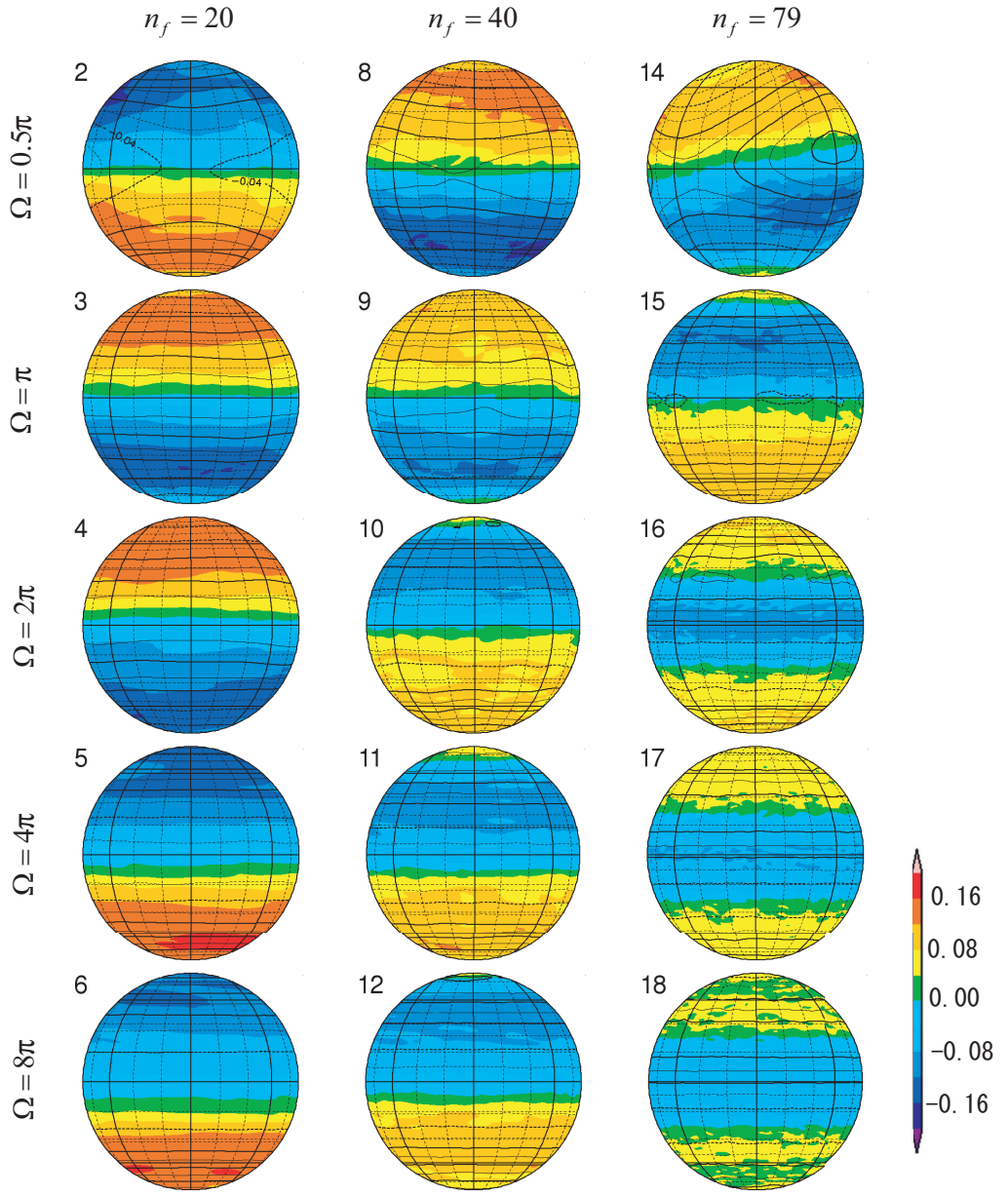

Figure 2.8: The stream function (contour lines) and zonal velocity (coloured) on a sphere at the final integral time: $t = 1\times10^5$ in runs $2-6, 8, 9, 14$, and 15, $t = 1.2 \times 10^5$ in run 10, $t = 2.5 \times 10^5$ in run 11, $t = 1.6 \times 10^5$ in run 12, $t = 5.3 \times 10^5$ in run 16, $t = 5.2 \times 10^5$ in run 17, and $t = 5.7 \times 10^5$ in run 18. The top of the sphere, the bottom of the sphere, and the centre line in each panel correspond to the North Pole (90° N), the South Pole (90° S), and the equator, respectively.

2.4 Stability of the 3-jet structure

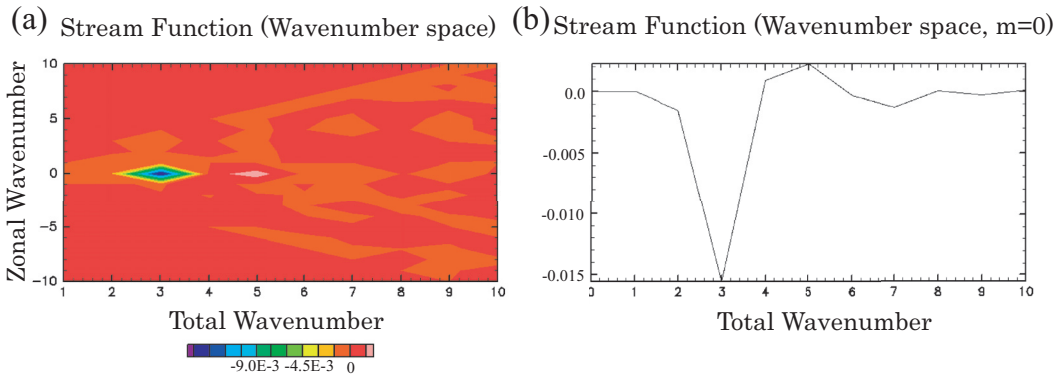

Figure 2.9: (a) The spectral distribution of the stream function ψ_n^m at $t = 4.5 \times 10^5$ in run 17 in the wavenumber space (For only $1 \leq n \leq 10, -10 \leq m \leq 10$ is shown). The horizontal and the vertical axes are total wavenumber n and zonal wavenumber m in linear scale, respectively. (b) The spectral distribution of zonal component of the stream function ψ_n^0 at $t = 4.5 \times 10^5$ in run 17 in the wavenumber space (For only $1 \leq n \leq 10$ is shown). The horizontal and the vertical axes are total wavenumber n and the stream function ψ_n^0 in linear scale, respectively.

As we have seen in §2.3.1, the structure with three zonal jets seen in runs 16, 17 and 18 is persistent and show little change for nearly 3×10^5 of non-dimensional time, whereas the asymptotic states consist of two broad zonal jets in the rest of the runs. It is not clear if the broad 3-jet state is the asymptotic state of the system. Here we examine the robustness of 3-jet state in run 17 by adding small perturbations with $(n, m) = (2, 0)$ to the stream function, since the main component of the stream function of the 2-jet state in the wavenumber space is the one with $n = 2$, and observe whether the three jets experience a merger and disappearance to make 2-jets state or not.

Fig.2.9 shows the stream function at $t = 4.5 \times 10^5$ in run 17. Now let us magnify the $(n, m) = (2, 0)$ component of this stream function two, three, five, and ten times, then make temporal development taking each new flow as the starting flow field at $t = 4.5 \times 10^5$. The temporal variations of the zonal-mean zonal angular momentum $\overline{[L_{lon}]}$ from $t = 4.5 \times 10^5$ to $t = 4.6 \times 10^5$ are shown in Fig.2.10. In all cases, the three jets do not experience merger

and disappearance and are persistently remain until the final time. Further more, $[\overline{L_{lon}}]$ appears to go back to the 3-jet state even when the starting flow field consists of two strong jets and a very weak jet, the third (weakest) jet is enhanced in the course of temporal development, and the 3-jet state is reproduced at $t = 4.6 \times 10^5$. In fact, as shown in Fig.2.11, the absolute value of the $(n, m) = (2, 0)$ component of the stream function decreases, and the $(n, m) = (4, 0)$ component increases instead. This suggests that the 3-jet state in runs $16, 17$ and 18 are robust, and the structure with three broad zonal jets may be the long-time asymptotic state in these cases (runs $16, 17$ and 18).

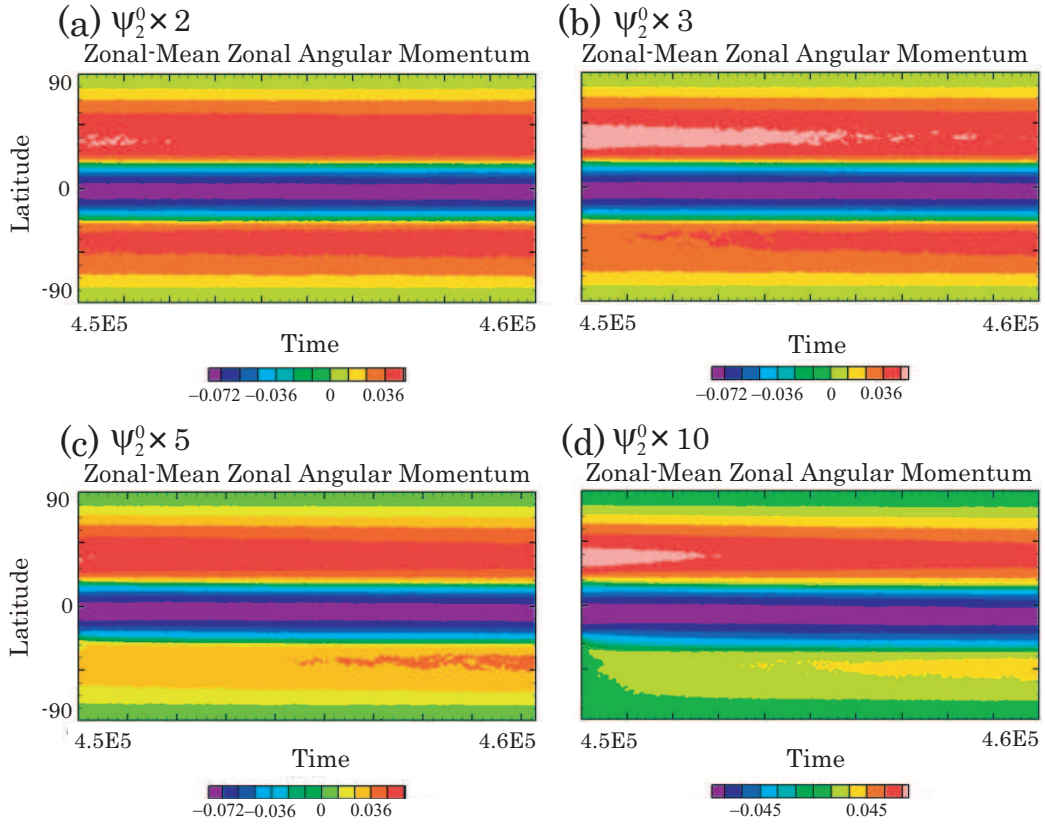

Figure 2.10: Temporal development of zonal-mean zonal angular momentum $\overline{[L_{lon}]}$, started from a perturbed 3-jet state. The horizontal and the vertical axes in each panel are time and latitude in linear scale, respectively. The flows are set to have ψ_2^0 two (a), three (b), five (c), and ten (d) times as large as that in run 17 at $t = 4.5 \times 10^5$.

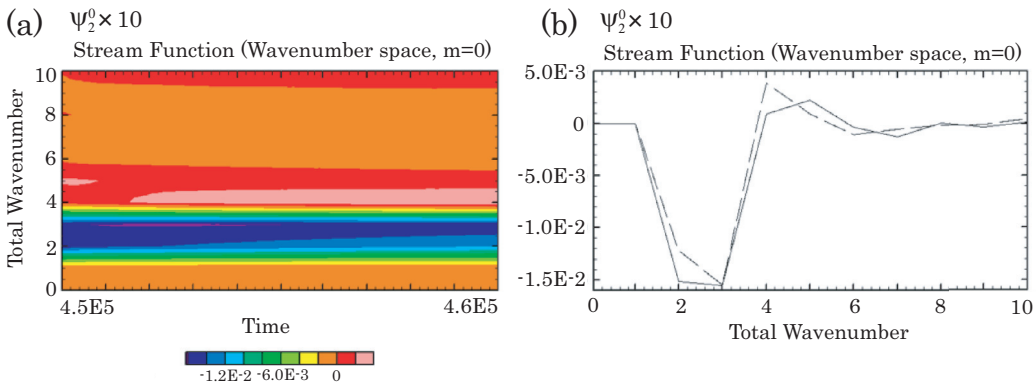

Figure 2.11: (a) Temporal variation of the spectral distribution of zonal component of the stream function ψ_n^0 (For only $1 \leq n \leq 10$ is shown). The horizontal and the vertical axes are time and total wavenumber n in linear scale, respectively. (b): The spectral distribution of zonal component of the stream function ψ_n^0 at $t = 4.5 \times 10^5$ (solid line) and $t = 4.6 \times 10^5$ (dashed line) (For only $1 \leq n \leq 10$ is shown). The horizontal and the vertical axes are total wavenumber n and ψ_n^0 in linear scale, respectively. The flow is set to have ψ_2^0 ten times as large as that in run 17 at $t = 4.5 \times 10^5$.

2.5 Discussions and Conclusions

In §2.2 and §2.3, we have performed 15 numerical simulations with the Markovian random forcing, with different combinations of the rotation rate of a sphere Ω, and the central total wavenumber of the forcing n_f. We have integrated the equation of motion numerically from $t = 0$ to $t = 1.0 \times 10^5$ (100 times of the integration time of Nozawa and Yoden [13]) or even more, with the zero initial condition. At an early stage of the integration, in line with the findings of Nozawa and Yoden [13], a multiple zonal-band structure or a structure with westward circumpolar jets emerges. However, in the course of further time development, multiple zonal-band structures appear in all runs, and then enter quasi-steady states showing little energy increase with nearly steady spectral distribution of the energy, followed by a sudden merger and disappearance of the jets, accompanying an energy increase. At the final stage of the time integration, a zonal-band structure with only a few (two or three) zonal jets were realised in each case. This affects the spectral distribution of the zonal energy, which shows the strong energy concentration to the total wavenumber $n = 2$ or 3 (this n coincides with the number of the jets) at the final integration time. At the final stage, the characteristic total wavenumber is lower than the Rhines wavenumber of the flow.

The numerical results show that the 2-jet state obtained here is one of the long-time asymptotic states of the two-dimensional barotropic incompressible flow with a small-scale, homogeneous, isotropic, and Markovian random forcing on a rotating sphere, as the energy inverse cascade cannot reach the wavenumber $n = 1$ due to the conservation law of total angular momentum. Contrary to this, it is not clear whether the 3-jet state at the final integration time is the asymptotic state or it is still changing to the 2-jet state. In §2.4, we considered the stability of the 3-jet state to the perturbation with wavenumber $(n, m) = (2, 0)$, and the result suggest that the 3-jet state may be possible to be one of the asymptotic states.

Huang *et al.* [14] has argued that the inverse energy cascade reaches below the Rhines wavenumber when the forcing is white noise, but not definitely when it is a Markovian random forcing. In our case of Markovian random forcing, the inverse energy cascade does not stop around the Rhines wavenumber but proceeds down to lower wavenumbers in the course of long-time evolution. This, together with the numerical result of Huang *et al.* [14], suggests that, in the forced two-dimensional barotropic incompressible flow on a rotating sphere, the inverse energy cascade cannot be arrested around

the Rhines wavenumber by the β effect irrespective of the kind of the forcing given to the system, and the asymptotic states consists of a very small number of zonal jets. This may also imply that a forced two-dimensional barotropic incompressible flow on a rotating sphere is not an appropriate model for the dynamics of the planetary atmospheres with multiple zonal-band structure such as the one seen on the Jupiter, as far as long-time asymptotic states are concerned.

Last but not least, although the real flow on a sphere becomes zonal to some degree even at an early stage of the time integration, the mergers and disappearances of the zonal jets seen in the simulations in this section is not explained by the barotropic instability, as a laminar zonal jet having a meridional scale larger than the Rhines scale, and is therefore linearly stable as discussed in §2.4. This strongly suggests that the turbulence behind the zonal jets is essential for the mergers and disappearances of the zonal jets, although the energy is almost concentrated on the zonal components. Hence in the next chapter, we consider zonal flows superposed upon simple non-zonal flow, which roughly models turbulence, and investigate the dynamics of zonal flows.

Chapter 3

Asymptotic analysis of long-time development of zonal flow

3.1 Introduction

In forced two-dimensional turbulence on a rotating sphere, a multiple zonal-band structure emerges from a small-scale random flow. Long numerical time integrations in §2 show that the multiple zonal jets experience merges and disappearances, passing over the Rhines scale as time progresses, and the structure with two or three large-scale alternating zonal jets remain at the final stage. Mergers and disappearances of zonal jets and the realisation of the zonal structure whose characteristic scale if larger than the Rhines scale are the common properties for the forced two-dimensional turbulence on a rotating sphere irrelevant to the settings of the forcing, whether the forcing is Markovian or white in time for example, or the settings for numerical simulation.

In the numerical simulation in §2, the representative flow scale becomes sufficiently larger then the Rhines scale even in the early stage of time integration. This suggests that the mergers and disappearances of the zonal jets and the realisation of the asymptotic state may be beyond the Rhines' theory that the robust and long-living flow structure is explained by the arrest of the inverse energy cascade around the Rhines number (Rhines [4]). Furthermore, although the zonal jets possesses most of the energy of the

flow at sufficiently large time where fully developed zonal-band structure is formed in the simulation, the mergers and disappearances of the jets described above cannot be explained only by the linear instability of laminar zonal jets, as a laminar zonal jet having a meridional scale larger than the Rhines scale becomes linearly stable. This strongly suggests that the effect of the background small-scale turbulence is essential for the theory of long-time behaviour of zonal jets in two-dimensional turbulence on a rotating sphere.

One of the possible interpretations of such a disappearance of zonal jets is that the state with multiple zonal jets may be dynamically unstable and the transition to a stable state with wider and fewer zonal jets may occur. It is accordingly tempted to examine the stability of zonal jets driven and maintained by a small-scale forcing and background small-scale turbulent motions.

Also, the interaction between neighbouring zonal jets through their tails and the background turbulence may be one of the conceivable physics which are working in a merging process of zonal jets described above. Then, the application of a reduction theory for the interaction between two isolated zonal jets under the influence of background small-scale turbulence is expected to work.

However, it is difficult to investigate the properties of zonal flows induced by a small-scale stochastic forcing, because it is hard to construct an analytically tractable and reasonable physical configuration. We therefore study zonal flows induced by a small-scale deterministic forcing instead of a stochastic forcing as a first step. Manfroi and Young [16] investigated the evolution of zonal flows on β plane when there is a homogeneous zonal flow and a small-scale sinusoidal transversal flow as a background base flow. They derived a time evolution equation of zonal flows with a small-scale background flow by using a multiple-scale expansion technique. This equation is a special case of Cahn-Hilliard equation [17], and we call it the Manfroi-Young equation for clarity. From numerical experiments of the Manfroi-Young equation in Manfroi and Young [16], it was found that, when the bottom drag is absent, a multiple zonal-band structure emerges, and then gradual disappearances of the zonal jet occur one by one, forming a thin eastward jet and a broad westward jet in the considered periodic domain. They also pointed out that the structure with one set of alternating zonal jets is the final state by using a Lyapunov functional analysis. Since the evolution of the zonal band structure seen in their numerical experiment is similar to long-time behaviour of zonal jets on a rotating sphere mentioned above, we may deduce some

physical insight about the dynamics of zonal flows induced by small-scale stochastic forcing by examining the system derived by Manfroi and Young more precisely.

Therefore in this chapter, based on the work of Manfroi and Young [16], we investigate the merging and the disappearing processes of zonal jets observed in two-dimensional turbulence on a rotating sphere and β plane. Showing that the merger and disappearance of zonal also observed as an outstanding property of forced two-dimensional turbulence on β plane §3.2, we briefly introduces the model and the equation used in Manfroi and Young [16], and then we analytically derive the steady isolated zonal jet solution of the Manfroi-Young equation in §3.3. In §3.4, to discuss the disappearing process, we examine the linear stability of the steady jet solutions both numerically and partially analytically, and also confirm their nonlinear time evolution. §3.5 considers the merging process of zonal jets by investigating the weak interaction between two identical steady zonal jets derived in §3.3. The time derivative (Ei [19]) of the distance between two identical zonal jets (two-jet state) is analytically estimated by using a perturbation method, and it is numerical calculated for a certain set of parameters. This is then compared with the result of numerical time integration of the Manfroi-Young equation. The strong nonlinear stage and the final state of the two-jet state are also examined numerically. Finally, We make modifications to the Manfroi and Young's model by taking account of the spatial variation of the disturbance in the zonal direction, and the surface variation of the fluid layer, in order to make the model a little more realistic, and investigate the linear stability of steady isolated zonal jets in these models in §3.6. Then discussions and conclusions are given in §3.7.

3.2 Long-time behaviour of forced two-dimensional turbulence on a β plane

β-plane approximation is often used in order to treat problems on a rotating sphere much simpler. The flow in this model is confined in a plane with no curvature, and the Coriolis parameter there is linearly approximated with respect to the meridional direction ($y-$coordinate). Although these treatments make the situation much simpler, same as the spherical-geometry case, long-time behaviour of forced two-dimensional turbulence on β plane is not yet fully known or understood.

Therefore in this section, we perform long-time integration of forced two-dimensional barotropic incompressible flows on a β to see its long-time behaviour.

3.2.1 Equation of motion and numerical method

A non-dimensionalised vorticity equation for a forced two-dimensional barotropic incompressible flow on a β plane at the position where (longitude, latitude) $= (\phi_0, \theta_0)$ on a rotating sphere is written by northward and eastward coordinates (x, y) as :[1]

$$\frac{\partial \zeta}{\partial t} + J(\psi, \zeta) + \beta \frac{\partial \psi}{\partial x} = F + \nu \nabla^2 \zeta. \tag{3.1}$$

Here, t is time, ψ is the stream function and $\zeta \equiv \nabla^2 \psi$ is the vorticity, where ∇^2 is the horizontal Laplacian. Ω is a dimensionless constant rotation rate of the sphere, $\beta \equiv 2\Omega \cos(\theta_0)$ is the β parameter, and $F = F(x, y, t)$ is the vorticity forcing function. ν is the dimensionless kinematic viscosity coefficient, and set to be $\nu = 3.46 \times 10^{-6}$ here. $J(A, B)$ is the Jacobian operator: $J(A, B) \equiv (\partial A/\partial x)(\partial B/\partial y) - (\partial A/\partial y)(\partial B/\partial x)$. The domain of the β plane is $[0, L_x] \times [0, L_y]$.

The vorticity forcing function F is taken to be the same type as that used for the case of spherical geometry in §2.2; small-scale, homogeneous, isotropic, Markovian random function, is given by

$$F(x, y, j\Delta t) = RF(x, y, (j-1)\Delta t) + \sqrt{(1 - R^2)}\hat{F}(x, y, j\Delta t) \tag{3.2}$$

[1]Same as the case of spherical geometry in §2.2, the non-dimensionalisation here is done by utilising the radius of the sphere as a length scale and inverse of the rotation rate of the sphere as a time scale.

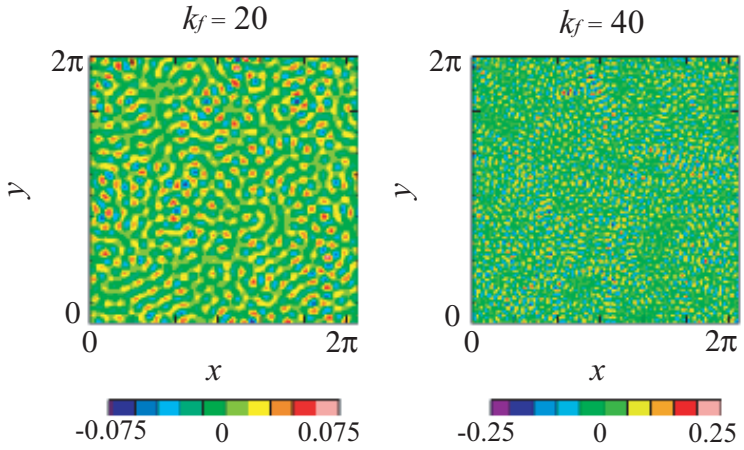

Figure 3.1: Vorticity forcing field at dimensionless time $t = 5000$. k_f of the left and right panels are 20and 40, respectively.

where Δt is the time step interval, j is the number of time steps, and $R = 0.982$ is the memory coefficient. $\hat{F}$ is a random vorticity source generated at each time step as

$$\hat{F}(x, y, j\Delta t) = \sum_{\substack{k_x, k_y \\ k_f - \Delta k \le k \le k_f + \Delta k}} \hat{F}_{k_x,\, k_y}(j)\ \exp(\frac{i\ 2\pi k_x x}{L_x})\ \exp(\frac{i\ 2\pi k_y y}{L_y}). \quad (3.3)$$

where $\hat{F}_{k_x,k_y}(j)$ is the double Fourier expansion coefficient of $\hat{F}$, $\frac{2\pi k_x}{L_x}$ and $\frac{2\pi k_y}{L_y}$ are wavenumbers of $x-$ and $y-$ directions. The phase of $\hat{F}_{k_x,k_y}$ are randomly and uniformly distributed on $[0,\ 2\pi]$. The amplitude of $\hat{F}_{k_x,k_y}$ are also random with $\parallel F \parallel = \sqrt{\langle \hat{F}^2 \rangle}$ being a prescribed value, where $\langle \cdots \rangle$ denotes the spatial mean on the β plane. Then $\hat{F}_{-k_x,-k_y}$ are the complex conjugate of $\hat{F}_{k_x,k_y}$, since $\hat{F}$ is real. This vorticity forcing is given in a small square region in the wavenumber space: $k_f - \Delta k \le k \le k_f + \Delta k$ with $\Delta k = 2$, where $k \equiv \sqrt{{k_x}^2 + {k_y}^2}$ and k_f is a central total wavenumber of the forcing. Fig.3.1 shows the examples of the vorticity forcing fields with $k_f = 20, 40$ and $\Delta t = 0.05$.

For the domain of the β plane $[0, L_x] \times [0, L_y]$, we consider $L_x = L_y = 2\pi$ and a double periodic boundary condition. A double Fourier spectral method is used for the calculation, by which the stream function ψ, for example, is

expanded as

$$\psi(x,y,t) = \sum_{k_x=-K_{xT}}^{K_{xT}} \sum_{k_y=-K_{yT}}^{K_{yT}} \psi_{k_x,k_y}(t)\ \exp(i\ 2\pi k_x\ x)\ \exp(i\ 2\pi k_y\ y).$$

Here, ψ_{k_x,k_y} is the expansion coefficient. We set the truncation mode numbers to be $K_{xT} = K_{yT} = 170$, then we take 512 spatial grid points for both in $x-$ and $y-$ directions, which are sufficiently large to eliminate the aliasing errors. Linear terms in the governing equation are analytically treated by using exponential function (See §A.3). The time integration is performed with the 4th order Runge-Kutta method with a time step width $\Delta t = 0.05$ from the initial condition $\zeta = 0$. With the conditions above, we have performed numerical simulations with different combinations of β, k_f and $\parallel F \parallel$. [2]

3.2.2 Results of numerical experiments

x-mean zonal x-direction velocity

Temporal development of $x-$mean $x-$direction velocity $\overline{[u_x]}$, where u_x is the x-component of the velocity is shown in Fig.3.2. Here, $\overline{[\ ]}$ denotes the x-mean, and $\overline{[u_x]}$ is given by

$$\overline{[u_x]} \equiv \frac{1}{2\pi}\int_0^{2\pi} u_x\ dx,$$

Same as in the numerical simulations on a rotating sphere in §2.3.1, a multiple zonal-band structure appears in the course of time development. This is followed by sudden mergers and disappearances of the zonal jets. The intermittent mergers and disappearances of the zonal jets may be a robust and common property of long-time behaviour of zonal flows on both a two-dimensional rotating sphere and β plane.

There is an outstanding tendency which is not so strongly seen in the spherical geometry case in §2.3.1; the mergers of the jets only occur for eastward jets and the disappearances of the jets only occur for westward jets, at least for the all cases we have considered [3].

[2] The convergence of the numerical simulations has been checked by performing calculations with different parameters; $\Delta t = 0.025$, which is half of the one used here; the truncation mode numbers $K_{xT} = K_{yT} = 340$ and the spatial grid points 1024×1024 which realise twice higher resolution than the one here. See §A.4.

[3] Although eastward jets tend to merge whilst a westward jets tend to disappear, we observe some mergers of westward jets in the spherical geometry case in §2.3.1.

In contrast to the spherical geometry case in §2.3.1, we observe cases with multiple zonal-band structure even at non-dimensional time $t = 5.0 \times 10^5$ for certain sets of parameters (See Fig.3.2 (b) for example.). The survival of multiple zonal-band structure at sufficiently large time on β plane may of course be attributed from conditions for the numerical simulations we have considered: strength and spatial scales of the forcing, for example. However, it is undeniable that the most critical reasons for this is caused by more fundamental differences between two systems: the absence of curvature on β plane; and the absence of North and South poles and usage of periodic boundary condition for North-South direction, *i.e.*,$y-$direction on β plane. Although the result here does not give a simple suggestion for asymptotic stats on β plane, it still suggests that the intermittent mergers and disappearances of the zonal jets is an important and fundamental property of the long-time behaviour of the zonal flows on β plane as well as on a two-dimensional rotating sphere.

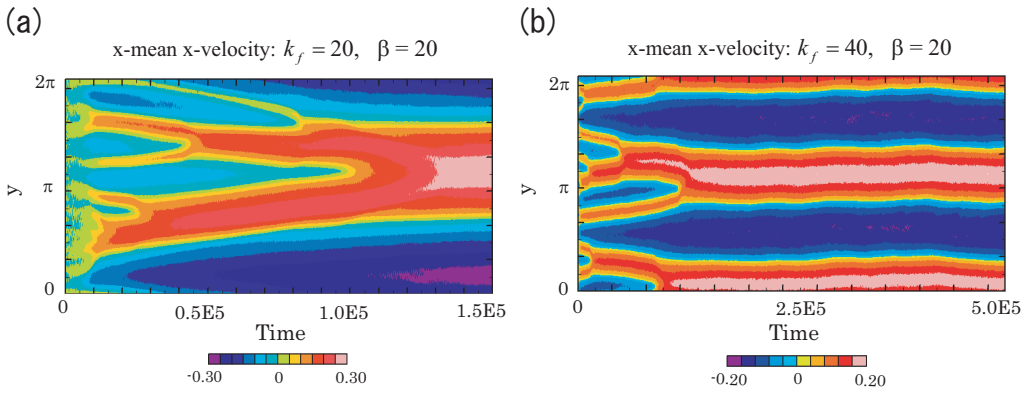

Figure 3.2: Long-time development of the $x-$mean $x-$velocity $\overline{[u_x]}$ for (a): $k_f = 20, \beta = 20.0$, and $\| F \| = 1.412 \times 10^{-2}$ (b): $k_f = 40, \beta = 10.0$, and $\| F \| = 3.929 \times 10^{-2}$. The horizontal and the vertical axes in each panel are time and y in linear scale, respectively. The temporal integrations have been performed (a): $t = 0 - 1.5 \times 10^5$ and (b): $t = 0 - 5.0 \times 10^5$.

The Rhines wavenumber

In the spherical-geometry case in §2.3.3, the inverse energy cascades proceed further even after the characteristic total wavenumber of the flow became

lower than the Rhines wavenumber, reflecting the realisation of the asymptotic states with a few large jets. This implies that the long-time behaviour of the zonal flow on the rotating sphere is beyond Rhines' theory that the robust and long-living flow structure is explained by the arrest of the inverse energy cascade around the Rhines number [4]. Here we compare the characteristic total wavenumber of the flow and the Rhines wavenumber to see whether the inverse energy cascade is stopped by the rotation effect around the the Rhines wavenumber, and whether Rhines' theory is valid in the long-time behaviour of the zonal jets on β plane.

Rhines wavenumber k_β on a β plane is defined by

$$k_\beta(t) \equiv \sqrt{\frac{\beta}{2U_{rms}(t)}}. \tag{3.4}$$

Here, $U_{rms}(t)$ is the rms velocity of the fluid:

$$U_{rms}(t) \equiv \sqrt{2\mathcal{E}(t)},$$

where $\mathcal{E}$ is the kinematic energy of the flow.

Now we define the energy-weighted mean total wavenumber k_{mean} as the characteristic total wavenumber of the flow;

$$k_{mean}(k,t) \equiv \frac{\sum_{k_x=-K_{xT}}^{K_{xT}} \sum_{k_y=-K_{yT}}^{K_{yT}} k\langle \mathcal{E}_{tot}(k,t)\rangle}{\sum_{k_x=-K_{xT}}^{K_{xT}} \sum_{k_y=-K_{yT}}^{K_{yT}} \langle \mathcal{E}_{tot}(k,t)\rangle},$$

where $k = \sqrt{{k_x}^2 + {k_y}^2}$ is the total wavenumber. $\langle \mathcal{E}_{tot}\rangle$ is given by

$$\langle \mathcal{E}_{tot}(k,t)\rangle \equiv \sum_{\substack{k_x,k_y \\ \sqrt{{k_x}^2+{k_y}^2}=k}} ({k_x}^2 + {k_y}^2)\ |\psi_{k_x,k_y}(t)|^2,$$

and this is the energy at the total wavenumber k.

The temporal variation of the Rhines wavenumber k_β and the characteristic wavenumber k_{mean} is shown in Fig.3.3. Note that both of them are infinity at $t = 0$, because $\mathcal{E}(0) = \langle \mathcal{E}_{tot}\rangle = 0$. The characteristic wavenumber k_{mean} becomes lower than the Rhines wavenumber k_β in a very early stage of the time integration, and decreases to reach a fairly low wavenumber at the final stage. The result suggests that the inverse energy cascade or the

energy transfer to lower wavenumbers continues even when $k_{mean} < k_\beta$, and that the Rhines wavenumber does not give an estimation of the characteristic wavenumber of the asymptotic flow field. Note that k_{mean} does not reach 1 precisely, even when the fully developed two broad jets are dominating over the β plane.

Now, We consider the necessary condition for the instability of a laminar zonal jet whose $x-$velocity is u_x on β plane: $\beta - \partial^2 u_x/\partial y^2$ changes its sign at least once in the considered domain. Then the scale analysis

$$\beta - \frac{\partial^2 u_x}{\partial y^2} \sim \beta - \frac{U_{rms}}{L_\beta^2} \sim \beta - \beta = 0, \tag{3.5}$$

where L_β is the Rhines scale defined by $L_\beta \equiv 1/k_\beta$, implies that the jets' mergers and disappearances seen in Fig.3.2 cannot be explained in a framework of laminar zonal flows, since a laminar jet having a meridional ($y-$direction) scale larger than the Rhines scale L_β becomes linearly stable, and that the effect of the background turbulence, though it is far weaker than the zonal jets, is an essential element for the long-time behaviour of zonal jets.

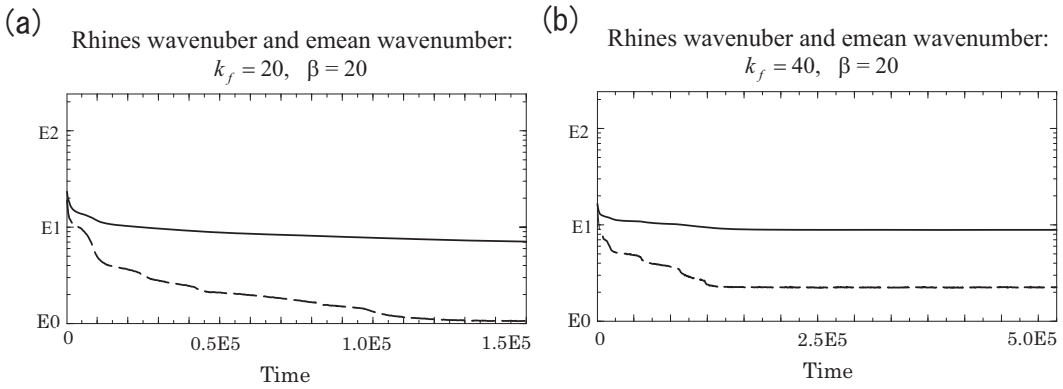

Figure 3.3: Temporal variation of the Rhines wavenumber k_β (solid line) and the characteristic wavenumber k_{mean} (dashed line) for (a): $k_f = 20, \beta = 20.0$, and $\parallel F \parallel = 1.412 \times 10^{-2}$ (b): $k_f = 40, \beta = 10.0$, and $\parallel F \parallel = 3.929 \times 10^{-2}$. Note that both k_β and k_{mean} are infinity at $t = 0$ because $\mathcal{E}(0) = \langle \mathcal{E}_{tot} \rangle = 0$. The horizontal and the vertical axes in each panel are time in linear scale and the Rhines wavenumber and the mean wavenumber in log scale, respectively. The temporal integrations have been performed (a): $t = 0 - 1.5 \times 10^5$ and (b): $t = 0 - 5.0 \times 10^5$.

3.3 Weakly nonlinear model and its steady isolated jet solution

From Sections §2 and §3.2, it has been confirmed that the intermittent mergers and disappearances of the zonal jets is one of the most fundamental and outstanding properties of the long-time behaviour of the zonal flow on both a two-dimensional rotating sphere and β plane. In addition to this, we have to keep it in our mind that, in these cases, it is not enough to discuss zonal jets in the framework of laminar flows, and the influence of the background turbulence should always be taken into account when we discuss mergers and disappearances of the zonal jets. This suggest that, in order to understand the long-time behaviour of the zonal structure appearers in forced two-dimensional Navier-Stokes turbulence on a rotating sphere and β plane, it is necessary to investigate the mechanism of merger and disappearance of the zonal jets having turbulent flows in their background. For this purpose, we now make the most of one of the features of β plane approximation, *i.e.*, we consider zonal flows and simply-modelled turbulence on an infinite β plane, and perform asymptotic analysis by utilising the spatial variables.

In this section, we briefly introduce weakly-nonlinear model of zonal flows induced by a small-scale deterministic forcing instead of a stochastic forcing and the amplitude equation of zonal flow, originally derived by Manfroi and Young [16]. Then we analytically derive one of its steady isolated jet solutions.

3.3.1 Model and the Manfroi-Young equation

To investigate zonal flows induced by a small-scale deterministic forcing instead of a stochastic forcing, Manfroi and Young [16] derived the governing equation of a zonal flow having a small-scale sinusoidal transversal flow behind it on a β plane, and studied their temporal evolution. Here, we briefly explain their derivation of the governing equation.

Let us consider an incompressible forced two-dimensional flow on a β plane where the governing equation for such flow is written as

$$\frac{\partial Z}{\partial t} + J(\Psi, Z) + \beta \frac{\partial \Psi}{\partial x} = F + \nu \nabla^2 Z. \tag{3.6}$$

Here t, Ψ, and $Z = \nabla^2 \Psi$ are the time, the stream function, and the vorticity. F and ν are the vorticity forcing function and the kinematic viscosity

coefficient. $J(A,B)$ is the Jacobian operator: $J(A,B) \equiv (\partial A/\partial x)(\partial B/\partial y) - (\partial A/\partial y)(\partial B/\partial x)$, and $\nabla = (\partial/\partial x, \partial/\partial y)$.

Suppose a steady base flow with the velocity

$$(u_B, v_B) = \left(-\frac{\partial \Psi_B}{\partial y}, \frac{\partial \Psi_B}{\partial x}\right) = (U_B, m\Psi_{B0} \sin mx) \tag{3.7}$$

is driven by a suitable forcing function on this β plane, where Ψ_B, u_B and v_B are the stream function, x and y components of the base flow, respectively, U_B and Ψ_{B0} are constants, and m is an integer. Now assume that the base flow is slightly unstable, that is, the Reynolds number of the base flow $R \equiv \Psi_{B0}/\nu$ is slightly larger than the critical Reynolds number R_c,

$$R = R_c(1 + \epsilon^2), \tag{3.8}$$

where ϵ is a small parameter. Then we write the total stream function of the flow as $\Psi = \Psi_B(x) + \psi(x,y,t)$, where $\psi(x,y,t)$ is the stream function of the disturbance flow and, from Eq.(3.6), satisfies

$$\frac{\partial \zeta}{\partial t} + U_B \frac{\partial \zeta}{\partial x} + m\Psi_{B0}\left(\frac{\partial \zeta}{\partial y} + m^2 \frac{\partial \psi}{\partial y}\right) \sin(mx) + J(\psi, \zeta) + \beta \frac{\partial \psi}{\partial x} = \nu \nabla^2 \zeta, \tag{3.9}$$

in which $\zeta \equiv \nabla^2 \psi$ is the vorticity of the disturbance flow. Introducing new variables,

$$(\hat{x}, \hat{y}) \equiv (mx, my), \quad \hat{t} \equiv tm^2\nu, \quad \hat{\psi} \equiv \frac{\psi}{\nu}, \tag{3.10}$$

we non-dimensionalise Eq.(3.9) as

$$\frac{\partial \hat{\zeta}}{\partial \hat{t}} + \hat{u}_B \frac{\partial \hat{\zeta}}{\partial \hat{x}} + R\left(\frac{\partial \hat{\zeta}}{\partial \hat{y}} + \frac{\partial \hat{\psi}}{\partial \hat{y}}\right) \sin \hat{x} + J(\hat{\psi}, \hat{\zeta}) + \hat{\beta} \frac{\partial \hat{\psi}}{\partial \hat{x}} = \hat{\nabla}^2 \hat{\zeta}, \tag{3.11}$$

where

$$\hat{u}_B \equiv \frac{u_B}{m\nu}, \quad \hat{\beta} \equiv \frac{\beta}{m^3\nu}. \tag{3.12}$$

We, hereafter, drop the notation $\hat{}$ for the dimensionless variables and operators for simplicity.

Using the small parameter ϵ defined in (3.8), we now perform perturbation expansions of the stream function of the disturbance flow ψ, U_B, and the β parameter:

$$\begin{aligned} \psi &= \psi_0 + \epsilon\psi_1 + \epsilon^2\psi_2 + \cdots, \\ U_B &= U_{B0} + \epsilon U_{B1} + \epsilon^2 U_{B2} + \cdots, \\ \beta &= \beta_0 + \epsilon\beta_1 + \epsilon^2\beta_2 + \cdots, \end{aligned} \tag{3.13}$$

and multiple-scale expansions:

$$\frac{\partial}{\partial x} \to \frac{\partial}{\partial x} + \epsilon^6 \frac{\partial}{\partial \xi}, \quad \frac{\partial}{\partial y} \to \epsilon \frac{\partial}{\partial \eta}, \quad \frac{\partial}{\partial t} \to \epsilon^4 \frac{\partial}{\partial \tau}, \tag{3.14}$$

where η, τ and ξ are defined as

$$\eta \equiv \epsilon y, \quad \tau \equiv \epsilon^4 t, \quad \xi \equiv \epsilon^6 x. \tag{3.15}$$

Substituting the expanded variables and operators (3.13), (3.14), and (3.15) into Eq.(3.11), then we obtain the equation for the $O(1)$ elements

$$\frac{\partial^4 \psi_0}{\partial x^4} - U_{B0} \frac{\partial^3 \psi_0}{\partial x^3} - \beta_0 \frac{\partial \psi_0}{\partial x} = 0, \tag{3.16}$$

which is satisfied if ψ_0 depends on ξ, η, τ as

$$\psi_0 = A(\xi, \eta, \tau). \tag{3.17}$$

Substituting the expanded variables and operators (3.13), (3.14), and (3.15) into Eq.(3.11) again, we next take the x-mean of it. By gathering the $O(\epsilon^6)$ elements, we obtain

$$\begin{aligned} \frac{\partial}{\partial \tau} \frac{\partial^2 A}{\partial \eta^2} + 2 \frac{\partial^4 A}{\partial \eta^4} + 3 \frac{\partial^6 A}{\partial \eta^6} - \frac{\partial^3}{\partial \eta^3} \left[\left(\beta_1 - U_{B1} + \frac{\partial A}{\partial \eta} \right)^2 \frac{\partial A}{\partial \eta} \right] \\ + \frac{1}{3} \frac{\partial^3}{\partial \eta^3} \left(\frac{\partial A}{\partial \eta} \right)^3 + \beta_0 \frac{\partial A}{\partial \xi} = 0. \end{aligned} \tag{3.18}$$

Considering the ξ-independent solution $A(\eta, \tau)$ of Eq. (3.18), Eq.(3.18) can be integrated over η twice. After all, the amplitude equation for the $O(1)$ elements of the x-independent disturbance flow $U(\eta, \tau)$

$$U(\eta, \tau) \equiv -\frac{\partial A(\eta, \tau)}{\partial \eta}, \tag{3.19}$$

is obtained as

$$\frac{\partial U}{\partial \tau} = -(2 - \gamma^2) \frac{\partial^2 U}{\partial \eta^2} - 3 \frac{\partial^4 U}{\partial \eta^4} - 2\gamma \frac{\partial^2 U^2}{\partial \eta^2} + \frac{2}{3} \frac{\partial^2 U^3}{\partial \eta^2}, \tag{3.20}$$

where γ is defined as

$$\gamma \equiv \beta_1 - U_{B1}. \tag{3.21}$$

Eq.(3.20) governs zonal flows having a small-scale sinusoidal transversal background flow. We call Eq.(3.20) the Manfroi-Young equation, and investigate the linear stability of its steady solutions. The full derivation of Eq.(3.20) is available in §4 in Manfroi and Young [16].

The Manfroi-Young equation is a special form of the one-dimensional Cahn-Hilliard equation [17] whose steady solutions and their stabilities have attracted much attention. Langer [20] studied the linear stability of the one-dimensional steady solution of the form of tanh, and also gave an intuitive explanation for the general stability criterion for a steady solution with a periodic boundary condition in an arbitrary dimensional case, which was extended to the cases of a natural boundary condition, or a null flux boundary condition, by Novick-Cohen and Segel [21]. Bettinson and Rowlands [22] performed linear stability analysis of a one-dimensional steady kink solution to a general Cahn-Hilliard equation in an infinite domain for both small- and large-wavenumber three-dimensional perturbations, and gave an approximate formula for eigenvalues by perturbation methods. The linear stability of a steady one-dimensional kink-antikink solution, which is called a bubble solution, and of a multibubble solution was studied by Argentina *et al.* [23]. The bifurcations originating from varying system size are discussed for both a periodic boundary condition and a natural boundary condition. Villain-Guillot [24] suggested that steady non-symmetric soliton-lattice solutions, which belong to the family of the soliton-lattice solutions discussed in Novick-Cohen and Segel [21] are linearly unstable. Although a great deal of research has been carried out for the stability of steady solutions of the Cahn-Hilliard equation, to the best of the authors' knowledge, the steady solution which consists of one bump in an infinite domain and their linear stabilities relevant to the present β plane problem have not been investigated yet. Thus in the following two sections, we derive steady solutions of the Manfroi-Young equation analytically and investigate their linear stability both numerically and analytically.

3.3.2 Steady isolated zonal jet solution U_0

[4]

Now, we consider a steady solution $U_0(\eta)$ of Eq.(3.20), having one bump

[4]Published in Obuse *et al.* [25]

and $U_0 \to U_W$ as $\eta \to \pm\infty$, where U_W is a constant[5]. The equation and boundary conditions for the U_0 are

$$-(2-\gamma^2)\frac{d^2U_0}{d\eta^2} - 3\frac{d^4U_0}{d\eta^4} - 2\gamma\frac{d^2U_0^2}{d\eta^2} + \frac{2}{3}\frac{d^2U_0^3}{d\eta^2} = 0, \tag{3.22a}$$

$$U_0 \to U_W, \quad \frac{dU_0}{d\eta} \to 0 \quad \text{as } \eta \to \pm\infty. \tag{3.22b}$$

To solve Eq.(3.22a), we first integrate it over η twice, and use conditions (3.22b)[6]. Multiplying $dU_0/d\eta$ to both hand sides of the obtained equation, and integrating it with η again, we have

$$\frac{dU_0}{d\eta} = \pm\frac{1}{3}\sqrt{-V(U_0)}. \tag{3.23}$$

Here, the potential $V(U_0)$ is defined as

$$V(U_0) \equiv -U_0^4 + 4\gamma U_0^3 + 3(2-\gamma^2)U_0^2 - 6C_1U_0 - 3C_2, \tag{3.24}$$

and the constants of integration C_1 and C_2 are

$$\begin{aligned} C_1 &= (2-\gamma^2)U_W + 2\gamma U_W^2 - \frac{2}{3}U_W^3, \\ C_2 &= U_W^4 - \frac{8}{3}\gamma U_W^3 - (2-\gamma^2)U_W^2. \end{aligned} \tag{3.25}$$

To realise the solution U_0 that takes the same value U_W at $\eta \to \pm\infty$, the potential $V(U_0)$ should have the shape shown in Fig.3.4, specifically; $V(U_0)$ must take a double root U_W and two other different real roots U_E and U_R $(U_E \neq U_R)$[7] $V(U_0)$, as a consequence, should be expressed as

$$\begin{aligned} V(U_0) &= (U_0 - U_W)^2(U_0 - U_E)(U_0 - U_R), \\ U_E &< U_R, \quad U_W \neq U_E, \quad U_W \neq U_R. \end{aligned} \tag{3.26}$$

[5]The steady solution having the eastward/westward bump is expressed as a steady solution with an/a eastward/westward jet hereafter.

[6]We adopt natural conditions $d^2U_0/d\eta^2, d^3U_0/d\eta^3 \to 0$ $(\eta \to \pm\infty)$

[7]U_W,U_E correspond to the U_W, U_E in Fig.3 in Manfroi and Young[16], and U_R is the rest root. For the case U_0 is an eastward jet, U_W and U_E give the westward and eastward maximum values of the U_0, respectively; for the case U_0 is a westward jet, U_R and U_W give the westward and eastward maximum values of the U_0, respectively.

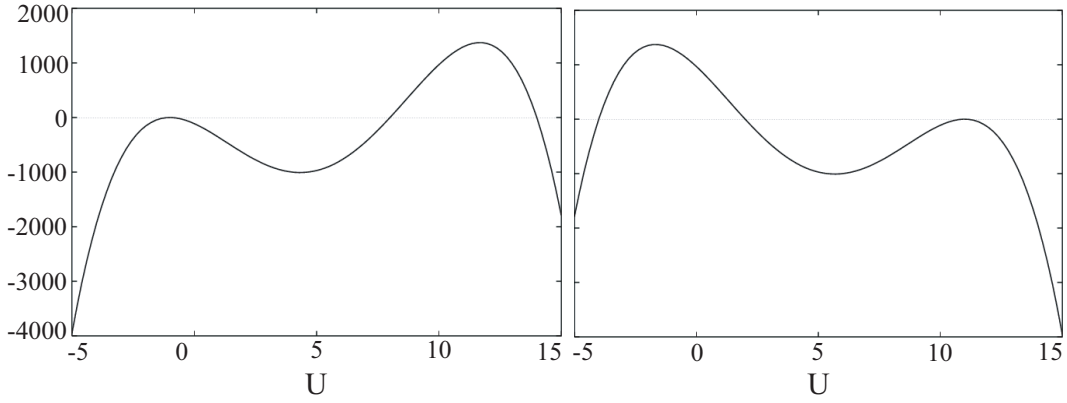

Figure 3.4: Examples of the shape of potential $V(U_0)$ which realises a solution $U_0(\eta)$ that satisfies $U_0 \to U_W$ as $\eta \to \pm\infty$. $U_W < U_E < U_R$ for $V(U_0)$ which realises U_0 with an eastward jet (Left: for the case $\gamma = -5, U_W = 1$), while $U_E < U_R < U_W$ for $V(U_0)$ which realises U_0 with a westward jet (Right: for the case $\gamma = 5, U_W = -1$).

From the definitions (3.24) and (3.25), on the other hand, $V(U_0)$ can be factorised as

$$V(U_0) = -(U_0 - U_W)^2\{{U_0}^2 - 2(2\gamma - U_W)U_0 - (6 - 3\gamma^2 + 8\gamma U_W - 3{U_W}^2)\}. \tag{3.27}$$

As $V(U_0)$ has to be factorised to the form of Eq.(3.26), there must exist two different real roots U_E and U_R in addition to U_W. For the discriminant of the last factor of Eq.(3.27) to be positive, we have

$$\gamma - \frac{1}{2}\sqrt{6(\gamma^2+2)} < U_W < \gamma + \frac{1}{2}\sqrt{6(\gamma^2+2)}. \tag{3.28}$$

Note that in the case where

$$U_W = \gamma - \frac{1}{2}\sqrt{6(\gamma^2+2)} \tag{3.29a}$$

or

$$U_W = \gamma + \frac{1}{2}\sqrt{6(\gamma^2+2)}, \tag{3.29b}$$

$V(U_0)$ has two real double roots U_W and $U_E = U_R$, the only solution of

(3.22a) and (3.22b) is $U_0 = U_W$[8]. The parameters U_W, U_E, and U_R should satisfy $U_W < U_E < U_R$ (for an eastward jet) or $U_E < U_R < U_W$ (for a westward jet) as shown in Fig.3.4. Therefore, the last factor of (3.27),

$$U_0^2 - 2(2\gamma - U_W)U_0 - (6 - 3\gamma^2 + 8\gamma U_W - 3U_W^2) = (U_0 - U_E)(U_0 - U_R),$$

has to be positive at $U_0 = U_W$, and thus

$$U_W < \gamma - \frac{1}{2}\sqrt{2(\gamma^2+2)} \quad \text{or} \quad \gamma + \frac{1}{2}\sqrt{2(\gamma^2+2)} < U_W, \tag{3.30}$$

should be satisfied. Again note that the case

$$U_W = \gamma - \frac{1}{2}\sqrt{2(\gamma^2+2)} \tag{3.31a}$$

or

$$U_W = \gamma + \frac{1}{2}\sqrt{2(\gamma^2+2)}. \tag{3.31b}$$

corresponds to the situation that either U_E or U_R is the same value as the double root U_W.

The conditions (3.28) and (3.30) are shown in Fig.3.5 where the hatched regions give (γ, U_W) corresponding to a steady solution U_0 which has one bump and takes the value U_W at $\eta \to \pm\infty$. The upper hatched region corresponds to U_0 with a westward jet, while lower hatched region to U_0 with an eastward jet.

Under the conditions of (3.28) and (3.30), U_0 has a double real root U_W and two other different real roots U_E and U_R;

$$U_E = 2\gamma - U_W - \sqrt{-2U_W^2 + 4\gamma U_W + \gamma^2 + 6}, \tag{3.32}$$

$$U_R = 2\gamma - U_W + \sqrt{-2U_W^2 + 4\gamma U_W + \gamma^2 + 6}. \tag{3.33}$$

[8]Apart from this uniform solution, if we do not assume that U_0 should converge to a same value, U_W, as η goes to $\pm\infty$, Eq.(3.22a) has a sigmoid solution

$$U_{0sig} = \pm\left(U_E + \frac{U_W - U_E}{\exp[(\eta - c)(U_W - U_E)/3] + 1}\right),$$

where c is a constant which determine the centre position of these solutions. These solution U_{0sig} are the asymptotic forms of the rising and decreasing curves of U_0, *i.e.* U_0 is made by superposing two U_{0sig} of different signs.

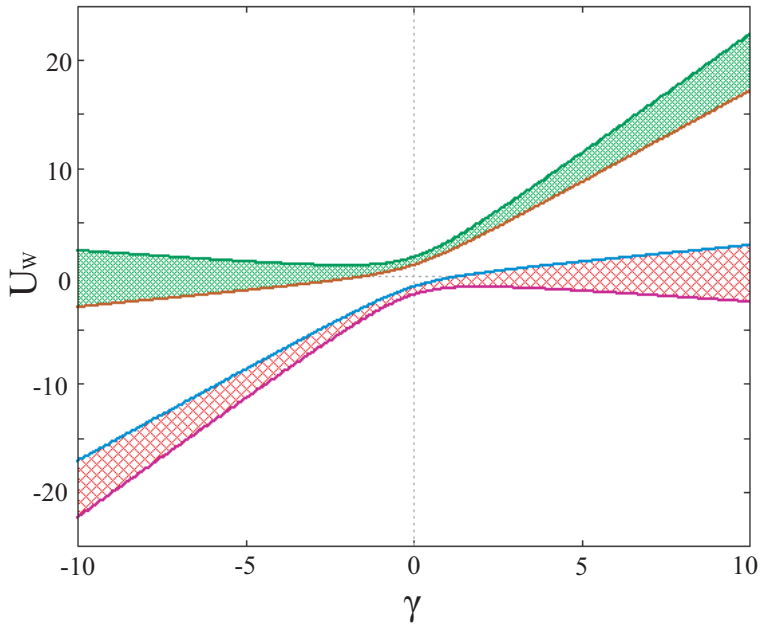

Figure 3.5: The regions of (γ, U_W) which realise one-bump steady solution U_0. The upper and lower hatched regions correspond to U_0 with an eastward jet and with a westward jet, respectively. The boundary curves are, from above, (3.29b)(dark green), (3.31b)(brown), (3.31a)(light blue), and (3.29a)(purple).

Eq.(3.23) is then written as

$$\frac{dU_0}{d\eta} = \pm\frac{1}{3}\sqrt{(U_0 - U_W)^2(U_0 - U_E)(U_0 - U_R)}. \tag{3.34}$$

A steady solution with an eastward jet $U_{0east}(\eta)$ $(U_W \leq U_{0east}(\eta) \leq U_E)$ is obtained by integrating Eq.(3.34) as

$$\int_{\eta_E}^{\eta} d\eta = \pm 3 \int_{U_E}^{U_{0east}(\eta)} \frac{dU_0}{(U_0 - U_W)\sqrt{(U_0 - U_E)(U_0 - U_R)}},$$

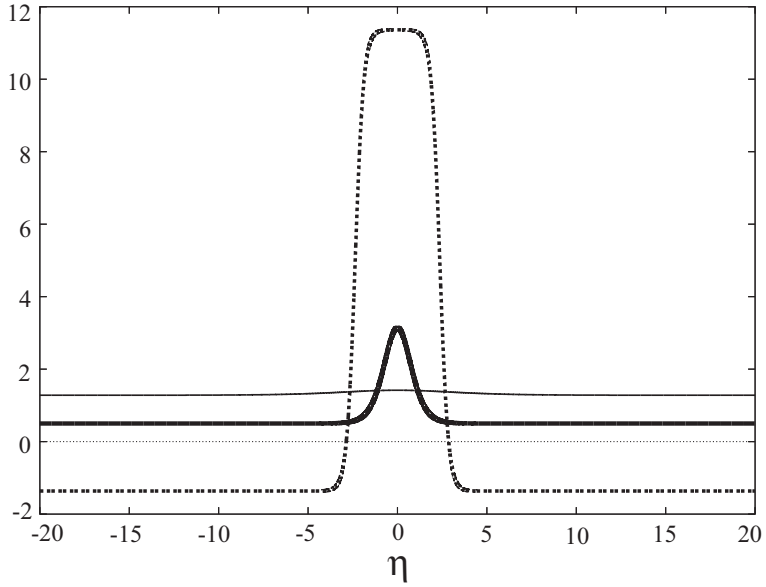

Figure 3.6: Examples of steady solutions with an eastward jet; $(\gamma, U_W) = (5.0, -1.363961)$:dashed line, $(5.0, 0.5)$:thicker solid line, $(5.0, 1.28)$:thinner solid line.

where η_E is defined to satisfy $U_{0east}(\eta_E) = U_E$, which leads to

$$U_{0east}(\eta) = \frac{a_{east}^2 U_R \tanh^2\left[\frac{(U_R-U_W)a_{east}}{6}\eta\right] - U_E}{a_{east}^2 \tanh^2\left[\frac{(U_R-U_W)a_{east}}{6}\eta\right] - 1}, \tag{3.35a}$$

$$a_{east} \equiv \sqrt{\frac{U_E - U_W}{U_R - U_W}}. \tag{3.35b}$$

Examples of $U_{0east}(\eta)$ are shown in Fig.3.6 for some combinations of γ and U_W. Jets near the boundary curve (3.29a) have trapezoid-like shape; jets near the boundary curve (3.31a) are almost flat; and jets apart from the boundaries have sharp shapes. A steady solution with a westward jet $U_{0west}(\eta)$

$(U_R \leq U_{0west}(\eta) \leq U_W)$ is similarly obtained as

$$U_{0west}(\eta) = \frac{a_{west}^2 U_E \tanh^2\left[\frac{(U_E-U_W)a_{west}}{6}\eta\right] - U_R}{a_{west}^2 \tanh^2\left[\frac{(U_E-U_W)a_{west}}{6}\eta\right] - 1}, \tag{3.36a}$$

$$a_{west} \equiv \sqrt{\frac{U_R - U_W}{U_E - U_W}}. \tag{3.36b}$$

Note that no steady solution exists on the boundary curves (3.29a), (3.29b), (3.31a), and (3.31b).

3.4 Disappearing processes of zonal jets – Linear stability of U_0

[9]

From numerical experiments of the Manfroi-Young equation (3.20), Manfroi and Young [16] found, when the bottom drag is absent, a multiple zonal-band structure, *i.e.* the structure with multiple zonal jets emerges, and then gradual disappearances of the zonal jet occurs one by one, forming a thin eastward jet and a broad westward jet in the considered periodic domain. We now pay attention to the disappearing process of zonal jets seen in their numerical simulation. This is discussed by examining the linear stability of steady isolated zonal jet solution U_0 introduced in §3.3.2, and their nonlinear time evolution.

3.4.1 Characteristic equation and eigenvalues

To investigate the linear stability of a steady solution $U_0(\eta)$, we first derive its characteristic equation. Consider the case in which a sufficiently small perturbation $v(\eta, \tau)$ is added to the steady solution $U_0(\eta)$. Substituting $U = U_0 + v$ for U in Eq.(3.20), we linearise it with respect to v. Further, we assume v to be in the following form,

$$v = \exp(\sigma\tau) f(\eta),$$

where $f(\eta)$ is a certain function, which satisfies,

$$f \to 0, \quad \frac{df}{d\eta} \to 0 \quad as\ \eta \to \pm\infty.$$

Then, we have

$$\sigma f = \frac{d^2}{d\eta^2}\left\{[-(2-\gamma^2) + (2U_0^2 - 4\gamma U_0)]f - 3\frac{d^2 f}{d\eta^2}\right\}. \tag{3.37}$$

Assume that $\sigma \neq 0$. By integrating Eq.(3.37) over η twice, we find

$$\int_{-\infty}^{\infty}\int_{-\infty}^{\eta} f(\eta')d\eta'\, d\eta = 0.$$[10]

[9] Published in Obuse *et al.* [25]

[10] We assume $d^2f/d\eta^2, d^3f/d\eta^3 \to 0$ $(\eta \to \pm\infty)$ as in Eq.(3.22a)

Now rewriting $f(\eta)$ as

$$f(\eta) = \frac{d^2 g(\eta)}{d\eta^2}, \quad g(\eta) \to 0, \quad \frac{dg(\eta)}{d\eta} \to 0, \quad \text{as } \eta \to -\infty.$$

We have

$$g(\eta) = g(\eta) - g(-\infty) = \int_{-\infty}^{\eta} \int_{-\infty}^{\eta'} \frac{d^2 g(\eta'')}{d\eta''^2}\, d\eta''\, d\eta' = \int_{-\infty}^{\eta} \int_{-\infty}^{\eta'} f(\eta'')\, d\eta''\, d\eta'.$$

This means that, $g, dg/d\eta \to 0$ as $\eta \to \pm\infty$. Putting $f = d^2 g/d\eta^2$ into Eq.(3.37), and integrating this equation over η twice, the characteristic equation is obtained as follows.

$$\sigma g = \left[-(2-\gamma^2) + (2U_0^2 - 4\gamma U_0)\right] \frac{d^2 g}{d\eta^2} - 3\frac{d^4 g}{d\eta^4}, \tag{3.38}$$

$$g \to 0, \quad \frac{dg}{d\eta} \to 0 \quad as\ \eta \to \pm\infty.$$

From the symmetry property of the characteristic equation, it easily follows that investigating the linear stability of U_{0east} with $\gamma \geq 0$ is enough to know the linear stability of all the U_0 (See §A.5). It is easily verified that the characteristic equation (3.38) also holds for $\sigma = 0$.

We solve the eigenvalue problem (3.38) numerically by the Fourier spectral method, where U_0, U_0^2, g are expressed as

$$\begin{aligned} U_0 &= \sum_{k=-K}^{K} u_k \exp\left(ik\frac{2\pi}{L_\eta}\eta\right), \\ U_0^2 &= \sum_{k=-K}^{K} d_k \exp\left(ik\frac{2\pi}{L_\eta}\eta\right), \\ g &= \sum_{k=-K}^{K} c_k \exp\left(ik\frac{2\pi}{L_\eta}\eta\right). \end{aligned} \tag{3.39}$$

We consider the domain $[0, L_\eta]$ and a periodic boundary condition for η. The width of the domain, L_η, was determined so that the numerical calculation converges sufficiently [11]. The width of the spatial grids was set to be around

[11] We have performed numerical calculations with both $L_\eta = 150$ and $L_\eta = 225$, and have confirmed that the relative errors are less than 0.1%.

10^{-3}, and the truncation mode number K was taken in the way that the maximum wavenumber $2\pi K/L_\eta$ becomes 10π for each case.

Fig.3.7 shows the real parts of the leading eigenvalues, $\sigma_{fr} \equiv \mathrm{Max}\{\mathrm{Re}(\sigma)|$ (γ, U_W) : fixed$\}$, for $\gamma = 0.0, 1.0,$ and 5.0 and U_W satisfying the conditions (3.28) and (3.30). It is apparent that every σ_{fr} is positive and that the maximum value of σ_{fr} becomes larger for the larger γ, while σ_{fr} converges to 0 as U_W approaches the two boundary curves (3.29a) and (3.31a) (the purple and the light blue curves in Figs.3.5 and 3.7). The square roots of σ_{fr} are plotted in Fig.3.8. It is clear that $\sqrt{\sigma_{fr}}$ are aligned in the vicinity of the point on the two boundaries (3.29a) and (3.31a), and the zeros on the line obtained by the least square fitting are quite precisely on the boundaries (3.29a) and (3.31a) with the relative errors less than 0.4% for $\gamma = 0, 1.0,$ and 5.0. The numerical results therefore show that the real part of every leading eigenvalue is positive, implying that the steady solutions $U_0(\eta; \gamma, U_W)$ are all linearly unstable.

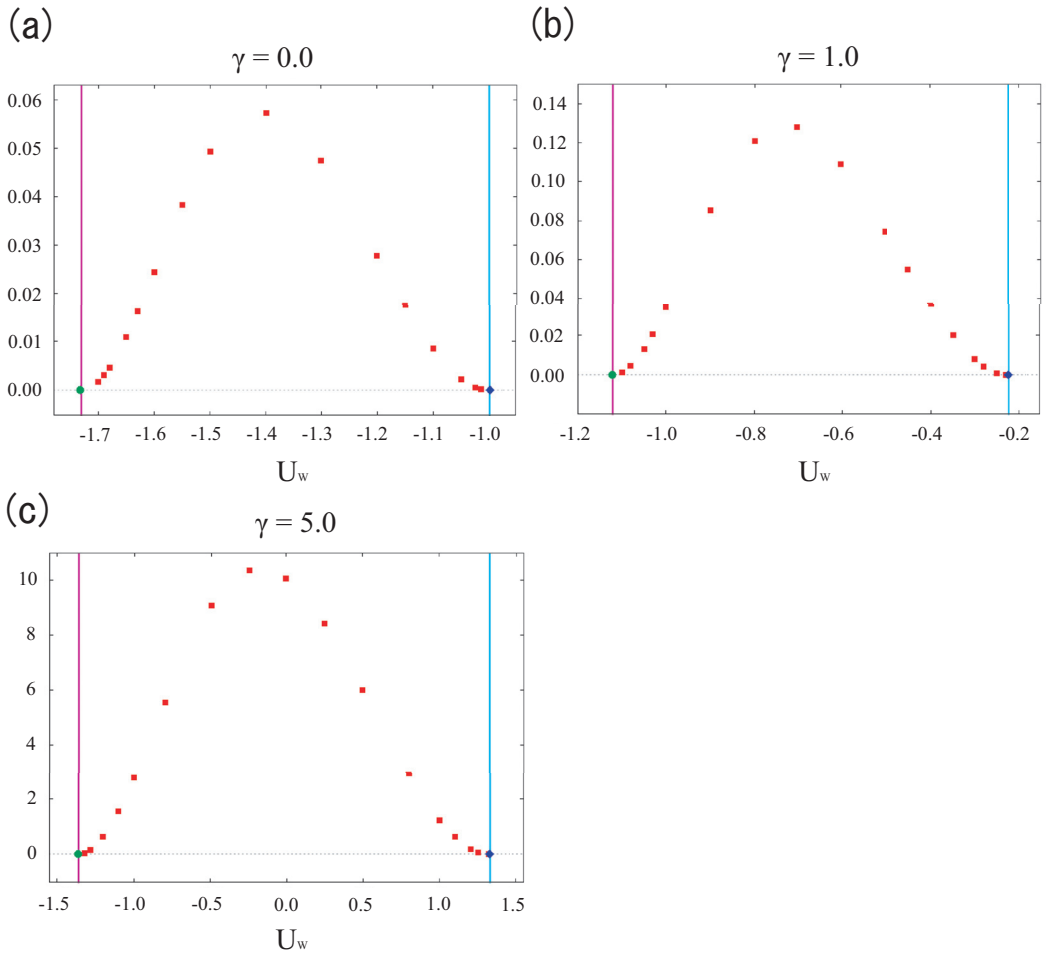

Figure 3.7: The real parts of the leading eigenvalues (red squares) for (a): $\gamma = 0.0$, (b): 1.0, and (c): 5.0. The purple and the light blue lines denote the two boundaries (3.29a) and (3.31a), which also correspond to the purple and the light blue curves in Fig.3.5. The green circle and the blue lozenge are the zeros obtained from the fitted lines shown in Fig.3.8.

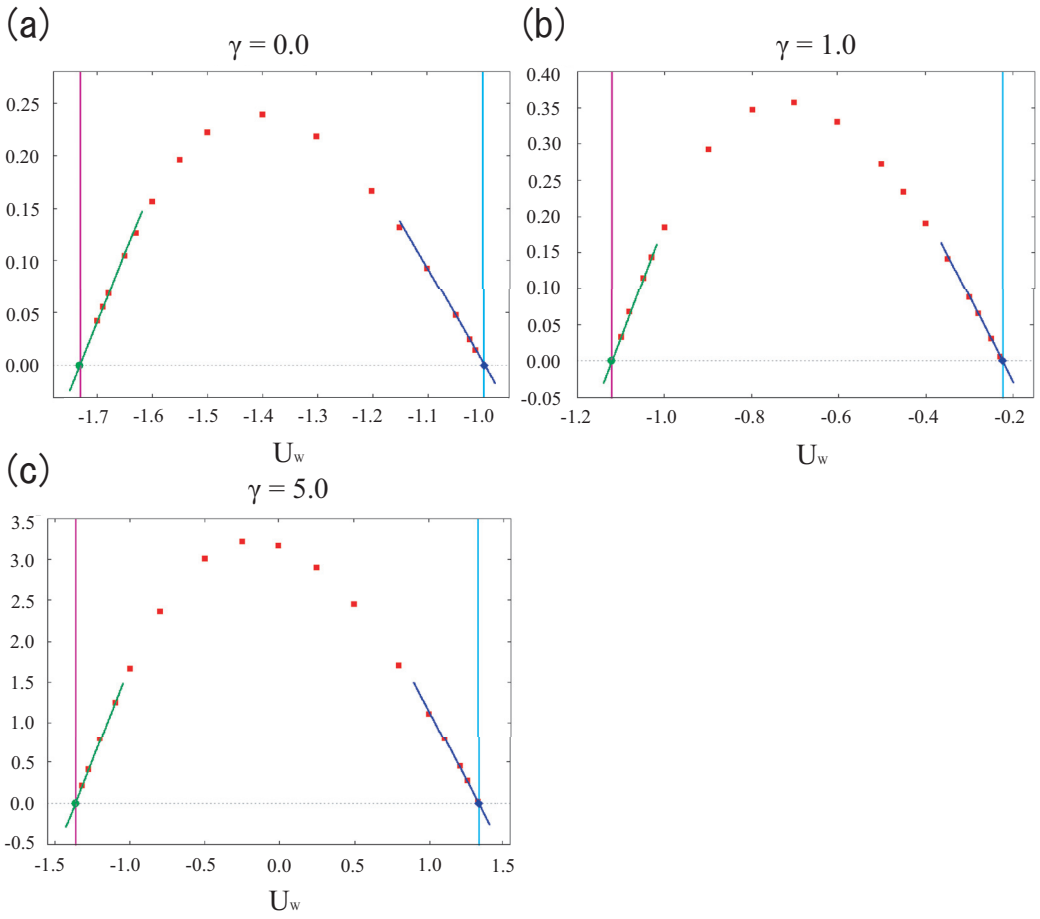

Figure 3.8: The square roots of the real parts of the leading eigenvalues (red squares) for (a): $\gamma = 0.0$, (b): 1.0, and (c): 5.0. The purple and the light blue lines denote the two boundaries (3.29a) and (3.31a), which also correspond to the purple and the light blue curves in Fig.3.5. The dark green and the dark blue lines are the fitted lines from the data, and the green circle and the blue lozenge are the zeros obtained from these fitted lines.

3.4.2 The analytical evaluation of the eigenvalues

It is numerically showed in §3.4.1 that, for a fixed γ, the real part of the leading eigenvalues $\sigma_{fr} = \mathrm{Max}\{\mathrm{Re}(\sigma)|(\gamma, U_W) : \mathrm{fixed}\}$ has zeros of the second order with respect to U_W on the curves (3.29a) and (3.31a). This feature is partly confirmed analytically below.

Around the upper boundary

On the boundary of the curve (3.31a), U_W is given by

$$U_W = \gamma - \frac{1}{2}\sqrt{2\,(\gamma^2+2)} \equiv U_{W_C},$$

which give $U_E \equiv U_{E_C} = U_{W_C}$ and

$$U_R = (2\gamma - U_{W_C}) + \sqrt{-2U_{W_C}^2 + 4\gamma U_{W_C} + \gamma^2 + 6} \equiv U_{R_C},$$

and then

$$U_{E_C} - U_{W_C} = 2(\gamma - U_{W_C}) - \sqrt{-2U_{W_C}^2 + 4\gamma U_{W_C} + \gamma^2 + 6} = 0. \tag{3.40}$$

Let us consider a point close to $C(\gamma, U_{W_C})$: $N(\gamma, U_W = U_{W_C} - \delta)$, where δ is positive and small. As $U_{W_C} = U_{E_C}$ on the curve (3.31a), U_E at the point N is expressed as $U_E = U_W + \epsilon$, where

$$\begin{aligned}
\epsilon &\equiv U_E - U_W \\
&= 2(\gamma - U_W) - \sqrt{-2U_W^2 + 4\gamma U_W + \gamma^2 + 6} && (3.41)\\
&= 2(\gamma - U_{W_C} + \delta) - \sqrt{-2(U_{W_C} - \delta)^2 + 4\gamma(U_{W_C} - \delta) + \gamma^2 + 6}. && (3.42)
\end{aligned}$$

Using the Eqs.(3.40) and (3.42), ϵ is given as

$$\epsilon = 3\delta + \mathrm{O}(\delta^2). \tag{3.43}$$

From (3.41) and (3.32), we have

$$2U_W^2 - 4\gamma U_W - (2-\gamma^2) = \frac{4}{3}(\gamma - U_W)\epsilon + \mathrm{O}(\epsilon^2). \tag{3.44}$$

Noting that $a^2 = \mathrm{O}(\sqrt{\epsilon})$, the steady solution U_0 on the point N can be written from (3.35a) as

$$U_0 \equiv U_W + \epsilon S(\sqrt{\epsilon}\eta) + O(\epsilon^2)$$

where

$$S(\sqrt{\epsilon}\eta) = \mathrm{sech}^2\left[\frac{\sqrt{U_R - U_W}}{6}\sqrt{\epsilon}\eta\right].$$

The characteristic equation (3.38) precise to O(ϵ) is, therefore,

$$\sigma g = \left[(\gamma - U_W)\left(\frac{4}{3} - 4S(\sqrt{\epsilon}\eta)\right)\epsilon\right]\frac{d^2g}{d\eta^2} - 3\frac{d^4g}{d\eta^4}. \tag{3.45}$$

Here, Eq.(3.44) has been used. Defining $s \equiv \sqrt{\epsilon}\eta$, Eq.(3.45) becomes

$$\sigma_1 g = \left[(\gamma - U_W)\left(\frac{4}{3} - 4S(s)\right)\right]\frac{d^2g}{ds^2} - 3\frac{d^4g}{ds^4}. \tag{3.46}$$

where $\sigma_1 = \sigma/\epsilon^2$. Hence, an eigenvalue σ given by Eq.(3.45) can be expressed with an eigenvalue σ_1 given by Eq.(3.46) as

$$\sigma = \epsilon^2\sigma_1 = 9\sigma_1\delta^2 = 9\sigma_1(U_{W_C} - U_W)^2. \tag{3.47}$$

where (3.43) has been used. Eq.(3.47) demonstrates that the eigenvalues in the vicinity of the point $C(\gamma, U_{W_C})$ behave as $9\sigma_1(U_{W_C} - U_W)^2$.

Fig.3.9 shows the real parts of the eigenvalues σ_{fr}, the two zeros obtained from the fitted line in §3.4.1, and the analytical curve (3.47), for $\gamma = 0.0, 1.0,$ and 5.0 and U_W which satisfy the conditions (3.28) and (3.30). σ_1 is obtained as $\sigma_1 = 0.111111, 0.166668,$ and 1.500000, respectively, by solving (3.46) numerically. The analytical curve fits fairly well with the leading eigenvalues in the vicinity of the point $C(\gamma, U_{W_C})$.

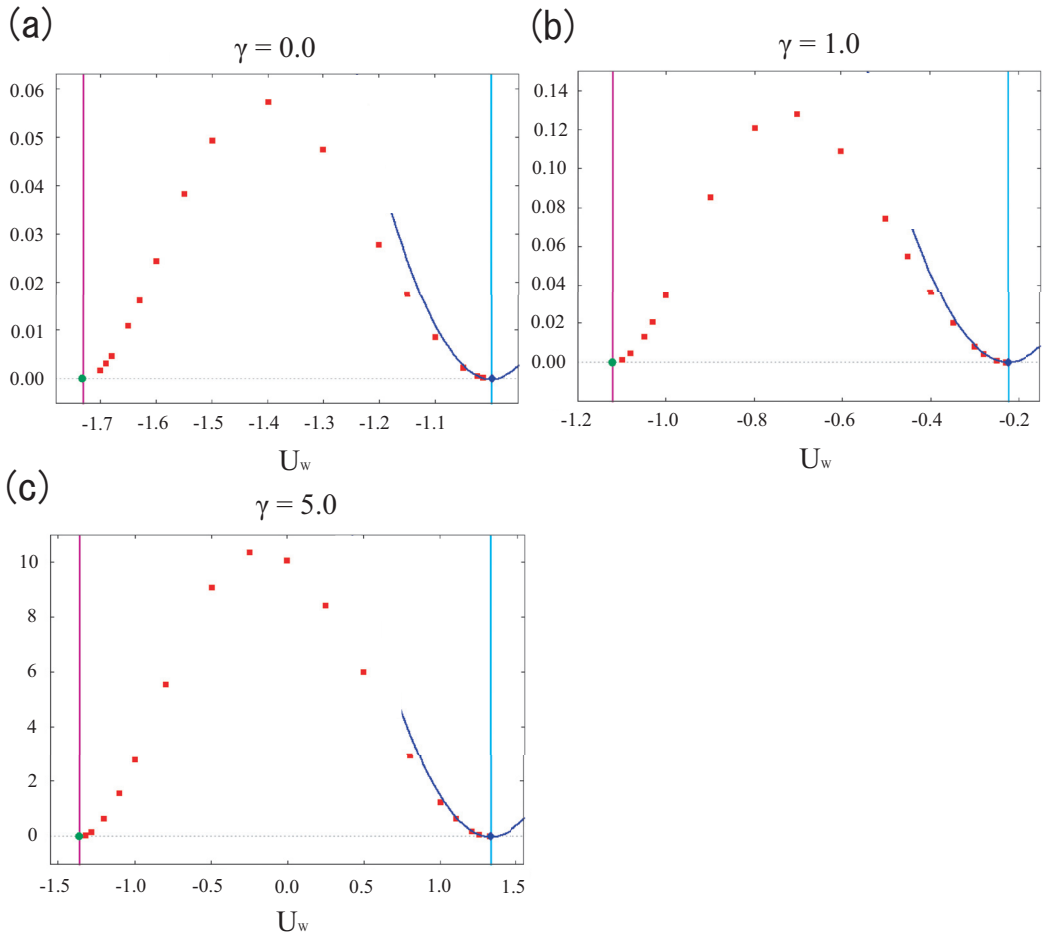

Figure 3.9: The real parts of the leading eigenvalues numerically calculated in §3.4.1 (red squares) and the analytical curve (3.47) (dark blue curves) for (a): $\gamma = 0.0$, (b): 1.0, and (c): 5.0. The purple and the light blue lines correspond to the two boundaries (3.29a) and (3.31a). The green circle and the blue lozenge are the zeros obtained from the fitted lines shown in §3.4.1.

Around the lower boundary

For the eigenvalues at (γ, U_W) close to the other boundary curve (3.29a), we analytically show below that the eigenvalues converge to zero as (γ, U_W) approaches an arbitrary point D on the boundary curve (3.29a).

Let us denote U_W at D as U_{W_D},

$$U_{W_D} = \gamma - \frac{1}{2}\sqrt{6(\gamma^2+2)},$$

and consider a point M close to the point $D(\gamma, U_{W_D})$: $M(\gamma, U_W = U_{W_D} + \delta)$, where δ is positive and small. Then a defined in Eq.(3.35b) at M satisfies

$$a^2 = 1 - \epsilon + \mathrm{O}(\delta),$$

where ϵ is defined as

$$\epsilon \equiv \frac{2\sqrt{2\sqrt{6(\gamma^2+2)}\delta - 2\delta^2}}{\sqrt{6(\gamma^2+2)}}.$$

Introducing α by

$$\begin{aligned}\alpha \equiv& \frac{a}{6}(U_R - U_W) \\ =& \frac{\sqrt{6(\gamma^2+2)}}{6}\left(1 - \frac{\epsilon}{2} + \mathrm{O}(\delta)\right),\end{aligned}$$

we can write $U_0(\eta)$ as

$$U_0(\eta) = \gamma - \delta + \frac{1}{2}\sqrt{6(\gamma^2+2)}(1+\epsilon) - \frac{\sqrt{6(\gamma^2+2)}}{\mathrm{sech}^2(\alpha\eta)/\epsilon + \tanh^2(\alpha\eta) + \mathrm{O}(\delta)}$$

for small δ. Now write η as $\eta = \eta_0 + \eta'$, where η_0 is defined such that

$$\mathrm{sech}(\alpha\eta_0) = \sqrt{\epsilon},$$

then, when $\delta \to 0$,

$$\frac{dU_0(\eta_0+\eta')}{d\eta'} = -\frac{1}{6}(-2U_0^2 + 4\gamma U_0 + \gamma^2 + 6),$$

and after all, the characteristic equation (3.38) becomes

$$\sigma g = \left[6\frac{dU_0}{d\eta'} + 2(2+\gamma^2)\right]\frac{d^2g}{d\eta'^2} - 3\frac{d^4g}{d\eta'^4}. \tag{3.48}$$

Multiplying $d^2g^\dagger/d\eta'^2$, where $g^\dagger$ is an adjoint solution of g, to both sides of Eq.(3.48) and integrating this over η, we obtain

$$-\sigma\int\left|\frac{dg}{d\eta'}\right|^2 d\eta' = \int\left[6\frac{dU_0}{d\eta'} + 2(2+\gamma^2)\right]\left|\frac{d^2g}{d\eta'^2}\right|^2 d\eta' + 3\int\left|\frac{d^3g}{d\eta'^3}\right|^2 d\eta'. \tag{3.49}$$

We next introduce $\phi \equiv d^2g/d\eta'^2$, and define a function

$$\begin{aligned} I[\phi] &\equiv \int\left[6\frac{dU_0}{d\eta'}|\phi|^2 + 3\left|\frac{d\phi}{d\eta'}\right|^2\right]d\eta' \\ &= \int\left[-3(\gamma^2+2)\mathrm{sech}^2(\alpha\eta')|\phi|^2 + 3\left|\frac{d\phi}{d\eta'}\right|^2\right]d\eta'. \end{aligned} \tag{3.50}$$

Now, we know that the Schrödinger equation

$$\left(-\frac{\hbar^2}{2m}\frac{d^2}{dx^2} - A_0\mathrm{sech}^2\beta x\right)\psi = E\psi, \quad A_0 > 0, \tag{3.51}$$

has its minimum eigenvalue (Landau-Lifshitz [26]),

$$E_0 = -\frac{\hbar^2\beta^2}{8m}\left[-1 + \sqrt{1 + \frac{8mA_0}{\hbar^2\beta^2}}\right]^2,$$

and therefore, we have

$$\int\left(\frac{\hbar^2}{2m}\left|\frac{d\psi}{dx}\right|^2 - A_0\mathrm{sech}^2\beta x|\psi|^2\right)dx \geq E_0\int|\psi|^2dx.$$

Applying this to Eq.(3.50) yields

$$I[\phi] \geq -2(\gamma^2+2)\int|\phi|^2d\eta',$$

hence, from Eq.(3.49),

$$-\sigma\int\left|\frac{dg}{d\eta'}\right|^2 d\eta' = I[\phi] + 2(\gamma^2+2)\int|\phi|^2d\eta' \geq 0;$$

this certifies the limit of the eigenvalue σ as $\delta \to 0$ is real and non-positive, which, together with Fig.3.7 and Fig.3.8, indicates $\lim_{\delta\to 0}\sigma = 0$ at the point D.

3.4.3 The growth of an unstable eigenfunction and the final flow field

As discussed above, every non-trivial steady solution $U_0(\eta)$ of Eq.(3.20) is linearly unstable. The next question is the final state (at $\tau = \infty$) of this unstable jet when it is slightly perturbed.

Fig.3.10 shows the leading eigenfunction and the time development of U_0 added its leading eigenfunction as the perturbation for the case $(\gamma, U_W) = (1.0, -1.05)$. The amplitude of the perturbation function is set to be 3% of that of U_0. The solution of Eq.(3.20) is numerically calculated with the Fourier spectral method. The time integration is performed with the 4th order Runge-Kutta method with a time step width $\Delta\tau = 1.0 \times 10^{-5}$. The boundary condition, the width of the domain, the truncation mode number K for the Fourier expansion, and the number of the grid point are all set to be the same with those used for the calculation for the eigenvalues in §3.4.1. In Fig.3.10, the jet become flat gradually, and the uniform flow is realised at the end. Note that it is easily verified that this uniform flow $U = U_W$ is linearly stable in the parameter regions shown in Fig.3.5 (See §A.6)[12].

[12]Precisely, the uniform flow obtained in the numerical simulation is not $U = U_W$, since the numerical simulation is performed in a periodic domain and conserves the momentum of the flow. However, if we use a domain sufficiently wide for the numerical calculation, it is almost equivalent to considering the development of the flow in an ideal infinite domain, then the resulting uniform flow is $U = U_W$. Actually, in Fig.3.10, we do not see visible shift of the baseline of the flow.

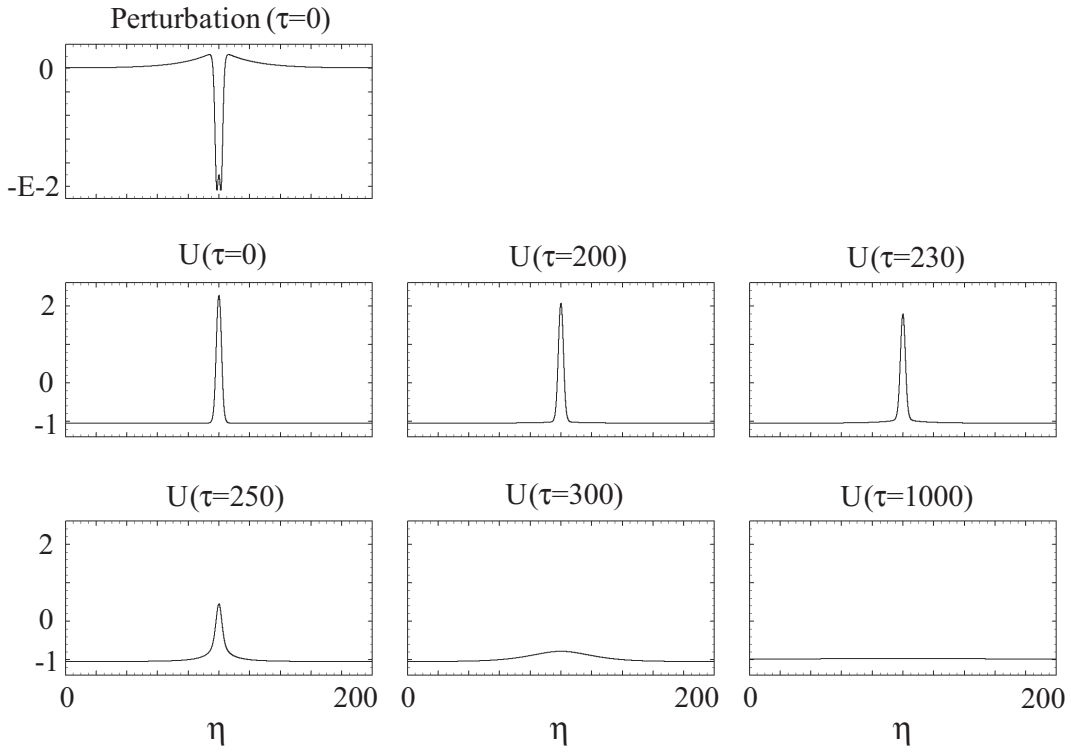

Figure 3.10: The eigenfunction of the leading eigenfunction (top row) and the temporal variation of the U_0 added the eigenfunction as a perturbation (middle and bottom rows) for the case $(\gamma, U_W) = (1.0, -1.05)$. Each panel is at time $\tau = 0, 200, 230,$(middle row, from the left to right) $\tau = 250, 300,$ and 1000 (the bottom row, from the left to the right).

3.5 Merging processes of zonal jets – Weak interaction between two zonal jets

The results of linear stability analysis of steady isolated zonal jet solutions U_0 and its long-time behaviour discussed in §3.4 seem to be in a good agreement with the evolution of zonal flows in the numerical experiment in Manfroi and Young [16], and also seem to imply the importance of the instability of zonal jets caused by the effect of the turbulence. In the long-time numerical simulations of two-dimensional turbulence on a rotating sphere and on β plane in §2 and §3.2, however, the disappearance of a zonal jet does not happen on its own, but it is almost always accompanied by a merger of the neighbouring two zonal jets. To closely study this situation, we investigate the weak interaction between two zonal jets by utilising a steady isolated zonal jet solution U_0.

3.5.1 Estimation of a weak interaction between two zonal jets

Here we estimate a weak interaction (Ei [19]) between two identical zonal jets using steady isolated zonal jet solutions (3.35a) of Manfroi-Young equation (3.20). This idea originate from the fact that the attraction of two neighbouring zonal jets each other precesses the merger in the numerical simulations of forced two-dimensional barotropic incompressible flows on a rotating sphere and on β plane.

Suppose two isolated zonal jets placed sufficiently far from each other are interacting through their tails (two-jet state). If the distance between them is large enough so that the interaction is very weak, we can estimate the effect of the interaction by utilising a perturbation method. Here, we have to be careful with the stability of zonal jets we use; the theory will not work well if the zonal jets are linearly unstable. Now all $U_0(\eta)$ are linearly unstable as stated in §3.4. Nevertheless, if we recall that U_0 is almost marginally stable when the combination of the parameters (γ, U_W) is near one of the boundary curves (3.29a), (3.29b), (3.31a), and (3.31b) (§3.4), and if we only consider such (U_W, γ), it may be allowed to assume that U_0 is linearly stable.

First of all, we decompose the steady solution $U_0(\eta)$ as

$$U_0(\eta) = \widetilde{U}_0(\eta) + U_W. \tag{3.52}$$

Then $\widetilde{U}_0 \to 0$ when $\eta \to \pm\infty$, so the tail of $\widetilde{U}_0$ is $O(\delta)$, where δ is small and positive. According to this decomposition, Manfroi-Young equation (3.20) is also rewritten as

$$\begin{aligned}\frac{\partial \widetilde{U}}{\partial \tau} &= -(2-\gamma^2)\frac{\partial^2 \widetilde{U}}{\partial \eta^2} - 3\frac{\partial^4 \widetilde{U}}{\partial \eta^4} - 2\gamma\left(\frac{\partial^2 \widetilde{U}^2}{\partial \eta^2} + 2U_W\frac{\partial^2 \widetilde{U}}{\partial \eta^2}\right) \\ &\quad + \frac{2}{3}\left(\frac{\partial^2 \widetilde{U}^3}{\partial \eta^2} + 3U_W\frac{\partial^2 \widetilde{U}^2}{\partial \eta^2} + 3U_W^2\frac{\partial^2 \widetilde{U}}{\partial \eta^2}\right).\end{aligned} \tag{3.53}$$

Now we place two identical jets $\widetilde{U}_{01}$ and $\widetilde{U}_{02}$ with sufficiently large distance h from each other and let them interact through their tails. Strictly, this two-jet state is not an exact solution of Eq.(3.20). If h is large enough, however, it may be possible to assume that it is an approximate solution of (3.53), and can be expressed as

$$\widetilde{U}(\eta,\tau) = \widetilde{U}_{01}\left(\eta - \ell_1(\tau)\right)) + \widetilde{U}_{02}\left(\eta - \ell_2(\tau)\right) + \widetilde{V}(\eta,\tau), \tag{3.54}$$

where $\widetilde{V}$ is the function to describe the deformation of the two jets. When $h = |\ell_1 - \ell_2|$ is large enough as stated above, the height of the tail of one jet is sufficiently small at the centre of the other jet, *i.e.* $U_{0i}(\eta = \ell_j) = O(\delta)$, $(i, j = 1 \text{ or } 2,\ i \neq j)$. Using this δ, we make further assumptions as follows.

$$\ell_1,\ \ell_2 :\ \mathrm{O}(1), \quad \widetilde{V}(\eta,\tau) :\ \mathrm{O}(\delta^3), \quad \frac{\partial}{\partial \tau} :\ \mathrm{O}(\delta^2), \quad \frac{\partial}{\partial \eta} :\ \mathrm{O}(1).$$

Now let us consider the influence that $\widetilde{U}_{02}$ gives to $\widetilde{U}_{01}$. To do this, we pay attention only to $\eta \sim \ell_1$, where $\widetilde{U}_{01}(\eta)$ is $O(1)$ and $\widetilde{U}_{02}(\eta)$ is $O(\delta)$. Substituting the approximate solution (3.54) into Eq.(3.53), we obtain

$$-\dot{\ell_1}\frac{\partial \widetilde{U}_{01}}{\partial \eta} - \dot{\ell_2}\frac{\partial \widetilde{U}_{02}}{\partial \eta} = \mathcal{L}(\widetilde{U}_{01} + \widetilde{U}_{02}) + L\widetilde{V} + \mathrm{O}(\epsilon^4). \tag{3.55}$$

Here, $\dot{*}$ denotes $\partial * / \partial \tau$. $\mathcal{L}$ and L are operators which satisfy

$$\begin{aligned}\mathcal{L}(\widetilde{U}_0) \ &\equiv -(2-\gamma^2)\frac{\partial^2 \widetilde{U_0}}{\partial \eta^2} - 3\frac{\partial^4 \widetilde{U}_0}{\partial \eta^4} - 2\gamma\left(\frac{\partial^2 \widetilde{U}_0^2}{\partial \eta^2} + 2U_W\frac{\partial^2 \widetilde{U}_0}{\partial \eta^2}\right) \\ &\quad + \frac{2}{3}\left(\frac{\partial^2 \widetilde{U}_0^3}{\partial \eta^2} + 3U_W\frac{\partial^2 \widetilde{U}_0^2}{\partial \eta^2} + 3U_W^2\frac{\partial^2 \widetilde{U}_0}{\partial \eta^2}\right),\end{aligned}$$

$$L\widetilde{V} \equiv -(2-\gamma^2)\frac{\partial^2\widetilde{V}}{\partial\eta^2} - 3\frac{\partial^4\widetilde{V}}{\partial\eta^4} - 4\gamma\frac{\partial^2}{\partial\eta^2}(\widetilde{U}_{01}+U_W)\widetilde{V} + 2\frac{\partial^2}{\partial\eta^2}(\widetilde{U}_{01}+U_W)^2\widetilde{V}.$$

If we write $\xi \equiv \eta - \ell_1(\tau)$, then $\widetilde{U}_{01}, \widetilde{U}_{02}$, and $\widetilde{V}$ are rewritten as

$$\begin{cases} \widetilde{U}_{01}\left(\eta-\ell_1(\tau)\right) = \widetilde{U}_{01}(\xi), \\ \widetilde{U}_{02}\left(\eta-\ell_2(\tau)\right) = \widetilde{U}_{02}\left(\xi-(\ell_2-\ell_1)\right) = \widetilde{U}_{02}(\xi-h), \\ \widetilde{V}(\eta,\tau) = \widetilde{V}(\xi,\tau), \end{cases} \tag{3.56}$$

We hereafter use $\widetilde{U}_0(\xi)$ and $\widetilde{U}_0(\xi-h(\tau))$ instead of $\widetilde{U}_{01}\left(\eta-\ell_1(\tau)\right)$ and $\widetilde{U}_{02}\left(\eta-\ell_2(\tau)\right)$. With these new notations, Eq.(3.55), $\mathcal{L}$, and L are

$$0 = \dot{\ell_1}\frac{\partial\widetilde{U}_0(\xi)}{\partial\xi} + \dot{\ell_2}\frac{\partial\widetilde{U}_0(\xi-h)}{\partial\xi} + \mathcal{L}\left(\widetilde{U}_0(\xi)+\widetilde{U_0}(\xi-h)\right) + L\widetilde{V}(\xi,\tau) \tag{3.57}$$

$$\begin{aligned}\mathcal{L}(\widetilde{U}_0(\xi)) \equiv & -(2-\gamma^2)\frac{\partial^2\widetilde{U}_0(\xi)}{\partial\xi^2} - 3\frac{\partial^4\widetilde{U}_0(\xi)}{\partial\xi^4} - 2\gamma\left(\frac{\partial^2\widetilde{U}_0(\xi)^2}{\partial\xi^2} + 2U_W\frac{\partial^2\widetilde{U}_0(\xi)}{\partial\xi^2}\right) \\ & + \frac{2}{3}\left(\frac{\partial^2\widetilde{U}_0(\xi)^3}{\partial\xi^2} + 3U_W\frac{\partial^2\widetilde{U}_0(\xi)^2}{\partial\xi^2} + 3U_W^2\frac{\partial^2\widetilde{U}_0(\xi)}{\partial\xi^2}\right),\end{aligned} \tag{3.58}$$

$$LV \equiv -(2-\gamma^2)\frac{\partial^2\widetilde{V}}{\partial\xi^2} - 3\frac{\partial^4\widetilde{V}}{\partial\xi^4} - 4\gamma\frac{\partial^2}{\partial\xi^2}(\widetilde{U}_0(\xi)+U_W)\widetilde{V} + 2\frac{\partial^2}{\partial\xi^2}(\widetilde{U}_0(\xi)+U_W)^2\widetilde{V}. \tag{3.59}$$

Now we introduce a new function

$$g(\xi,\tau) \equiv \dot{\ell_1}\frac{\partial\widetilde{U}_0(\xi)}{\partial\xi} + \mathcal{L}\left(\widetilde{U}_0(\xi)+\widetilde{U}_0(\xi-h)\right) \tag{3.60}$$

so that Eq.(3.57) is written as

$$-\dot{\ell_2}\frac{\partial\widetilde{U}_0(\xi-h)}{\partial\xi} = L\widetilde{V} + g. \tag{3.61}$$

Incidentally, since $\widetilde{U}_0(\eta)$ is a steady solution of Eq.(3.53), *i.e.*

$$\mathcal{L}\widetilde{U}_0(\xi) = 0$$

differentiating the above equation with respect to ξ yields

$$0 = \frac{\partial^2}{\partial\xi^2}\left[\left\{-(2-\gamma^2) - 3\frac{\partial^2}{\partial\xi^2} - 4\gamma\left(\widetilde{U}_0(\xi)+U_W\right) + 2\left(\widetilde{U}_0(\xi)+U_W\right)^2\right\}\frac{\partial\widetilde{U}_0(\xi)}{\partial\xi}\right] \tag{3.62}$$

$$= L\,\frac{\partial\widetilde{U}_0(\xi)}{\partial\xi}. \tag{3.63}$$

From Eq.(3.63), L possesses a zero eigenvalue whose eigenfunction is $\partial\widetilde{U}_0/\partial\xi$. The adjoint operator of L

$$L^\dagger \equiv \left\{-(2-\gamma^2) - 3\frac{\partial^2}{\partial\xi^2} - 4\gamma\left(\widetilde{U}_0(\xi)+U_W\right) + 2\left(\widetilde{U}_0(\xi)+U_W\right)^2\right\}\frac{\partial^2}{\partial\xi^2} \tag{3.64}$$

also possesses a zero eigenvalue whose eigenfunction ϕ is a certain real function which satisfies

$$L^\dagger\phi = 0. \tag{3.65}$$

We assume ϕ converges to a certain constant as $\xi \to \pm\infty$.

The inside of [ ] in Eq.(3.62) can be written as $A\xi + B$ by utilising $^\exists A, B \in \mathbb{R}$:

$$\left\{-(2-\gamma^2) - 3\frac{\partial^2}{\partial\xi^2} - 4\gamma\left(\widetilde{U}_0(\xi)+U_W\right) + 2\left(\widetilde{U}_0(\xi)+U_W\right)^2\right\}\frac{\partial\widetilde{U}_0(\xi)}{\partial\xi} = A\xi+B$$

Remembering $\widetilde{U}_0 \to 0$ and $\partial\widetilde{U}_0/\partial\xi \to 0$ as $\xi \to \pm\infty$, it is apparent that $A = B = 0$. This means, if we write the inside of [ ] in (3.62) as $M(\widetilde{U}_0(\xi) + U_W)\partial\widetilde{U}_0(\xi)/\partial\xi$,

$$M(\widetilde{U}_0(\xi)+U_W)\frac{\partial\widetilde{U}_0(\xi)}{\partial\xi} = 0 \tag{3.66}$$

holds. Then, from definition (3.64) and Eqs.(3.65) and (3.66),

$$\frac{\partial^2\phi}{\partial\xi^2} = \frac{\partial\widetilde{U}_0(\xi)}{\partial\xi}. \tag{3.67}$$

Integrating (3.67) with respect to ξ gives

$$\frac{\partial\phi}{\partial\xi} = \widetilde{U}_0(\xi) + C,$$

where C is constant. Since ϕ converges to a constant as $\xi \to \pm\infty$, C should be zero, *i.e.*

$$\frac{\partial \phi}{\partial \xi} = \widetilde{U}_0(\xi). \tag{3.68}$$

ϕ can be multiplied by an arbitrary constant by its definition, here we normalise it as

$$\left\langle \frac{\partial \widetilde{U}_0(\xi)}{\partial \xi},\ \phi \right\rangle_{L^2} = 1, \tag{3.69}$$

where $< *, * >_{L^2}$ is a L^2-inner product: $< f, g >_{L^2} = \int_\Omega fg\ d\mu$, where Ω is a domain and μ is a measure. In addition to this, as ϕ only appears in the inner product with other functions, its constant term has no importance. We therefore set $\phi(\xi = 0) = 0$.

Now we return to Eq.(3.61), and take an inner product between Eq.(3.61) and ϕ. This yields

$$-\left\langle \phi, \dot{\ell_2} \frac{\partial \widetilde{U}_0(\xi - h)}{\partial \xi} \right\rangle_{L^2} = \langle \phi,\ g \rangle_{L^2}\,. \tag{3.70}$$

Here we have used Eq.(3.65). As the orders, *i.e.* $\mathrm{O}(\delta^{\mathrm{n}}), \mathrm{n} = 0, 1, 2, ...$, of both sides of Eq.(3.70) are different, we can deduce that

$$\langle \phi,\ g \rangle_{L^2} = 0,$$

and together with the normalisation (3.69), it follows

$$\dot{\ell_1} = -\left\langle \mathcal{L}\left(\widetilde{U}_0(\xi) + \widetilde{U}_0(\xi - h) \right),\ \phi \right\rangle_{L^2}. \tag{3.71}$$

This is the shift of the centre of the jet $\widetilde{U_{01}}$ attributed to the existence of $\widetilde{U}_{02}$.

The influence from $\widetilde{U}_{01}$ to $\widetilde{U}_{02}$ is obtained in the same manner at $\eta \sim \ell_2$, and the resulting shift of the centre of $\widetilde{U_{02}}$ is

$$\dot{\ell_2} = -\left\langle \mathcal{L}\left(\widetilde{U}_0(\xi + h) + \widetilde{U_0}(\xi) \right),\ \phi \right\rangle_{L^2}. \tag{3.72}$$

From Eqs.(3.71) and (3.72), we finally obtain the estimation of the time derivative of the distance between two identical zonal jets

$$\begin{aligned} \dot{h} &= \dot{\ell_2} - \dot{\ell_1} \\ &= \left\langle \mathcal{L}\left(\widetilde{U}_0(\xi) + \widetilde{U}_0(\xi - h) \right),\ \phi \right\rangle_{L^2} - \left\langle \mathcal{L}\left(\widetilde{U}_0(\xi + h) + \widetilde{U}_0(\xi) \right),\ \phi \right\rangle_{L^2}. \end{aligned} \tag{3.73}$$

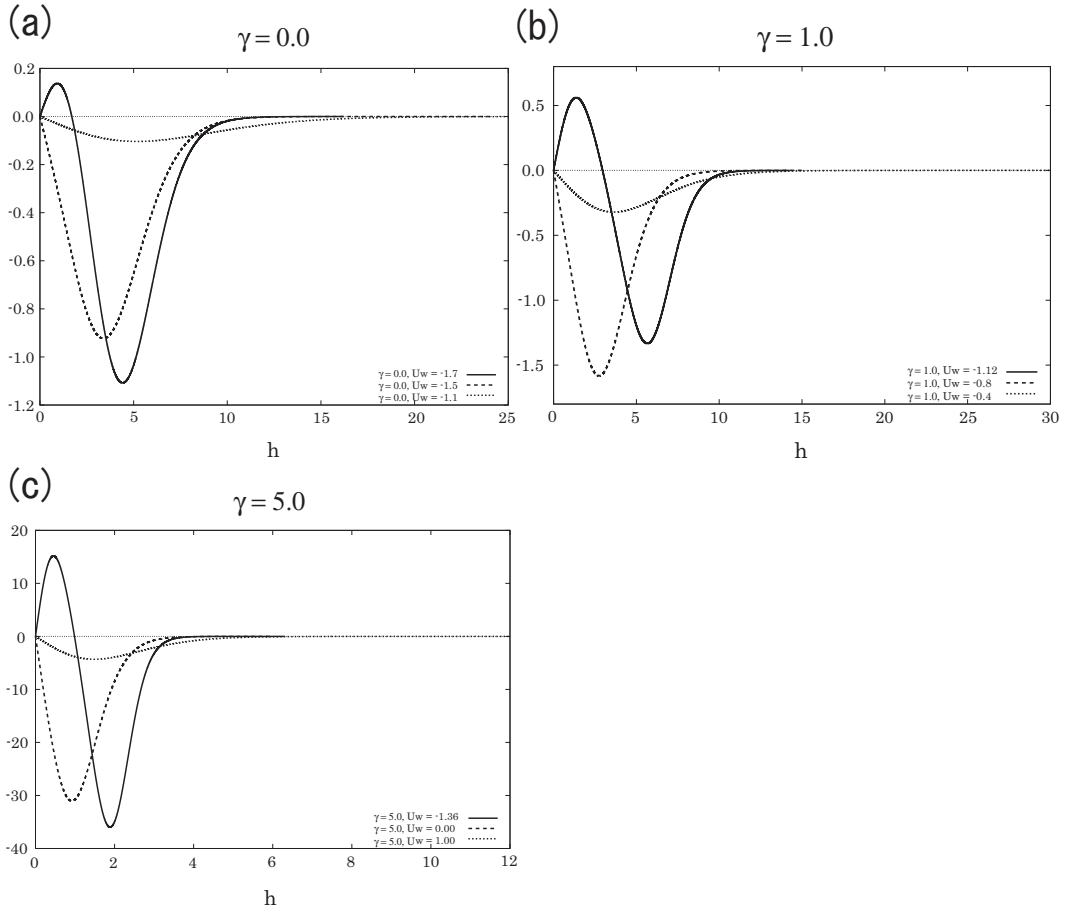

Figure 3.11: Examples of $\dot{h}_P$. (a): $\gamma = 0$, $U_W = -1.7$ (solid line), -1.5 (dashed line), and -1.1 (dotted line), (b): $\gamma = 1$, $U_W = -1.12$ (solid line), -0.8 (dashed line), and -0.4 (dotted line), (c): $\gamma = 5$, $U_W = -1.36$ (solid line), 0.0 (dashed line), and 1.0 (dotted line).

3.5.2 Numerical evaluation of the time derivative of the distance between two zonal jets

Time derivative of the distance between two identical zonal jets $\dot{h}$ has been obtained as (3.73) by perturbation analysis in §3.5.1. Now we numerically evaluate it, which will be addressed as $\dot{h}_P$ hereafter. This then will be compared with $\dot{h}_N$, the numerically obtained time derivative of the distance between two identical zonal jets by a full nonlinear calculation of Eq.(3.53).

For the numerical calculation of $\dot{h}_P$, we use the 4th order Runge-Kutta method to obtain unnormalised ϕ, and use the trapezoidal rule to normalise ϕ and calculate $\dot{h}_P$ from Eqs.(3.73) and (3.58). We consider the domain $[0, L_\eta]$ and a periodic boundary condition for ξ [13]. L_η is chosen to be $L_\eta = 50$, the width of the grids for space ξ and h are set to be $\Delta\xi = 1.0 \times 10^{-3}$ and $\Delta h = 1.0 \times 10^{-3}$, respectively. The numerical calculation sufficiently converges with these L_η, $\Delta\xi$, and Δh.

Fig.3.11 shows examples of $\dot{h}_P$. Parameters γ and U_W are chosen so that the examples locate near (3.29a), near (3.31a), and near neither (3.29a) nor (3.31a), respectively, for different values of γ in the parameter space. $\dot{h}_P$ is suggested to be all negative when two jets are sufficiently far from each other in any case. It is also confirmed, by checking several cases, that $\dot{h}_P \to 0$ monotonically as $h \to 0$. Note that although $\dot{h}_P$ take positive values for certain sets of parameters when two jets are close, it is the region where the assumption given in §3.5.1 that two jets should be placed with sufficiently large distance from each other does not hold. The results show that two identical zonal jets placed sufficiently apart may attract each other, and the attraction becomes stronger as the distance h between them gets smaller.

Now we choose the set of the parameters $\gamma = 5.0, U_W = -1.36$, where the instability of the steady solution $\widetilde{U_0}$ is fairly weak, and compare $\dot{h}_P$ with $\dot{h}_N$.

$\dot{h}_N$ is calculated from a full nonlinear numerical time integration of Eq.(3.53). The initial state for this is the one that two jets $\widetilde{U_0}$ are placed with $h(\tau = 0) = 4.3$, as shown in Fig.3.12 (solid line), in the domain $[0, L_\eta]$, $L_\eta = 50$ with a periodic boundary condition with respect to η. We use Fourier spectral method with a truncation $K = 150$, and the time integration is performed by the 4th order Runge-Kutta method. The width of the spatial and time grids are $\Delta\eta \sim 0.7 \times 10^{-3}$ and $\Delta\tau = 5.0 \times 10^{-5}$, respectively. $\dot{h}_N$ is calculated every $30 \times \Delta\tau$ from obtained h. The states at $\tau = 20.0$ is shown in Fig.3.12 (dashed line).

Fig.3.13 shows $\dot{h}_P$ and $\dot{h}_N$. In agreement with $\dot{h}_P$, $\dot{h}_N$ takes negative value and $|\dot{h}_N|$ becomes larger monotonically as h gets smaller, reflecting the fact that the two identical zonal jets placed apart attract each other and the attraction becomes stronger as the distance h gets smaller in the full nonlinear numerical time integration of Eq.(3.53).

[13] Although ϕ is not continuous at the boundary, this brings no critical problems since ϕ is always taken inner products with some functions, all of which converge to zero around the boundary.

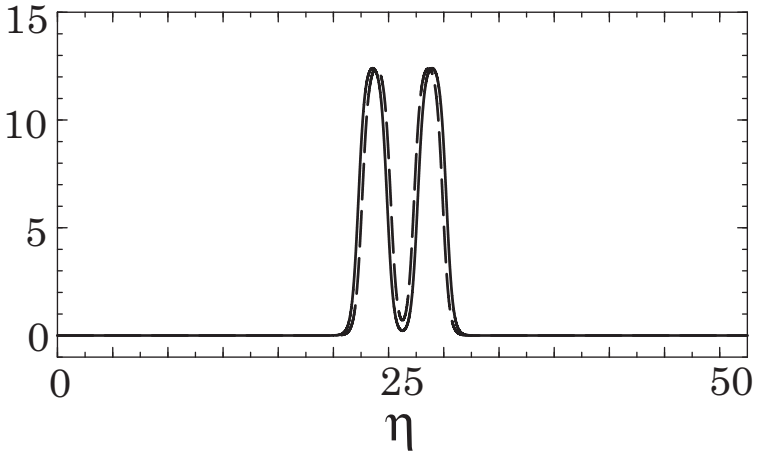

Figure 3.12: Solid line: initial two-jet state for the numerical time integration of Eq.(3.53). Dashed line: the state at $\tau = 20.0$ obtained by numerical time integration of Eq.(3.53). Parameters are $\gamma = 5.0, U_W = -1.36$.

The results obtained in this section strongly suggest that the attraction and the merger of the neighbouring zonal jets is due to the weak interaction between them through their tails.

3.5.3 Strongly nonlinear stage and the final state

Here, we numerically check the behaviour of two-jet states considered in §3.5.1 and §3.5.2 at strongly nonlinear stages and the final states. This is basically investigated by performing a longer numerical time integrations of Eq.(3.53) we have considered in §3.5.2.

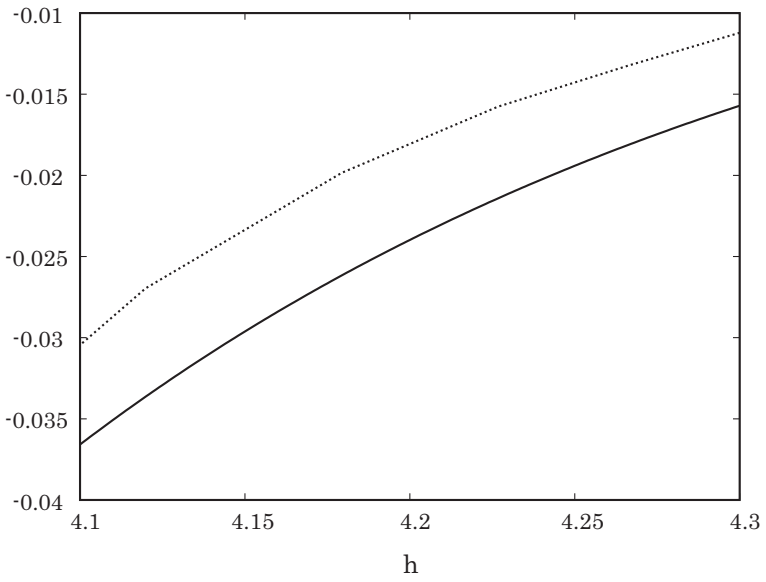

Figure 3.13: Upper dotted line: $\dot{h}_N$, Lower solid line: $\dot{h}_P$. Parameters are $\gamma = 5.0, U_W = -1.36$.

Weakly-unstable type

We choose the case $\gamma = 5.0, U_W = -1.36$, the same parameter set considered in §3.5.2, as an example of weakly-unstable type. Fig.3.14 shows the time development of the velocity U. During the first stage of time integration, two jets are attracted by each other and gradually shorten the distance h between them (not shown). Then, once h becomes small enough *i.e.* the effect of the interaction between two jets becomes strong enough, they speed up moving towards each other, keeping their general shapes, and merge to one jet at the centre of the first position of the two jets.

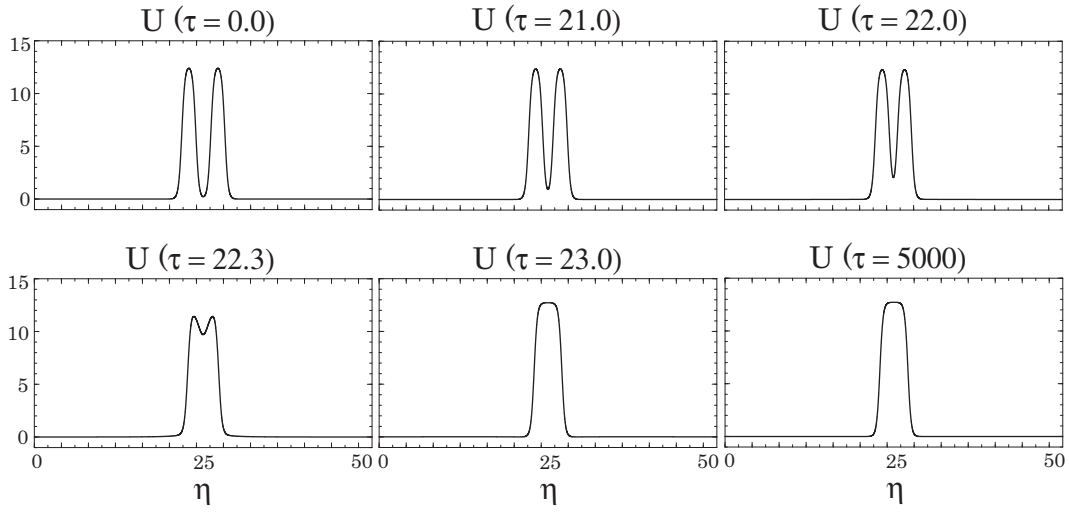

Figure 3.14: $\widetilde{U}$ of $\gamma = 5.0, U_W = -1.36$ at $\tau = 0.0,\ 21.0,\ 22.0$ (upper row, from the left to right), $\tau = 22.3,\ 23.0\ 5000.0$ (lower row, from the left to right).

The one jet resulted from the merger of two original jets survives very long time in the numerical simulation we have performed (Fig.3.14). This is probably because the obtained new jet is an another steady solution $\widetilde{U_0}$ of the same γ but a different U_W, whose instability is much weaker than the original steady jet $\widetilde{U_0}$ of $\gamma = 5.0, U_W = -1.36$. If we admit this assumption, as the numerical calculation here is performed in the periodic domain, which means the total momentum should be conserved, we can estimate U_{Wnew} of the new steady jet solution realised after the merger. U_{Wnew} obtained by Newton's method is $U_{Wnew} \sim -1.363960$. The numerically obtained new

jet after the merger and the steady solution U_{0new} of $\gamma = 5.0, U_{Wnew} = -1.363960$ are plotted in the same panel in Fig.3.15(a). $\widetilde{U_{0new}}$ falls in with the numerically realised new jet very well, showing that the assumption given above may be correct. Note that the small difference in U_W causes a big difference to the shape of $\widetilde{U_0}$ in this parameter range, and that the agreement of the shape can be a crucial support of the assumption that the numerically obtained new jet after the merger is a new steady jet of a different U_W. For an example of steady jet solution of another slightly different U_W, see Fig.3.15(b). The instability of the new steady isolated jet $\widetilde{U_{0new}}$ is much weaker than the original steady isolated jet $\widetilde{U_0}$ (§3.4) so that this allows $\widetilde{U_{0new}}$ to survive for a very long time as we see in Fig.3.14. Actually, by utilising fitted data of the leading eigenvalues of various U_W for $\gamma = 5.0$, it is suggested that Re[leading eigenvalue] of $\gamma = 5.0, U_W = -1.36$ is $O(10^{-4})$ and that of $\gamma = 5.0, U_W = -1.363960$ is $O(10^{-5})$, which indicate that time integration should be performed very long if we wish to see the deformation of $\widetilde{U_{0new}}$. Nevertheless, as all $\widetilde{U_0}$ is linearly unstable (§3.4), U_{0new} may, therefore, become a stable uniform flow (§3.4) in the end, and this will be the final state of two-jet states considered in §3.5.1 and §3.5.2.

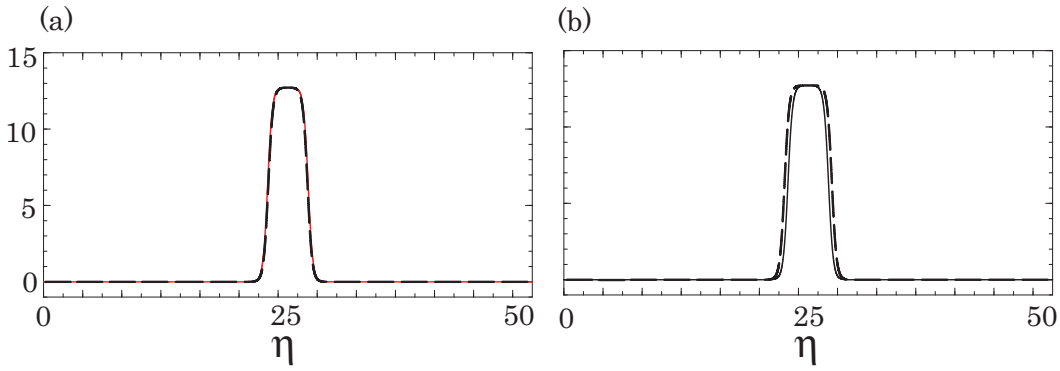

Figure 3.15: (a) Numerically obtained new jet $\widetilde{U}$ after the merger at $\tau = 5000$ (red solid line, $\gamma = 5.0, U_W = -1.36$) and $\widetilde{U_{0new}}$ (black dashed line, $\gamma = 5.0, U_W = -1.363960$). (b) $\widetilde{U_{0new}}$ ($\gamma = 5.0, U_W = -1.363960$, solid line) and $\widetilde{U_0}$ of $\gamma = 5.0, U_W = -1.363961$ (dashed line).

Strongly-unstable type

Here we consider the parameter set $\gamma = 5.0, U_W = -1.28$. The real part of the leading eigenvalue of the steady isolated zonal jet $\widetilde{U_0}$ is $O(10^{-1})$, then the jet is much more unstable than that of $\gamma = 5.0$ $U_W = -1.36$ whose real part of leading eigenvalue is $O(10^{-4})$[14].

Again in this parameter range, in agreement with the theoretical expectation and same as the numerically investigated weakly-unstable case, two identical zonal jets attract each other in the very first stage of the time integration. In contrast to the weakly-unstable type, however, then the strong deformation of the jets occurs, and as a result, one of the two jets disappears by being 'absorbed' into the other one (Fig.3.16). Here, the centre of the resulted one jet is shifted to the centre position of 'survived' jet. Under the the same assumption we made in §3.5.3 that the new jet is an another steady jet solution of the same γ but a different U_W, by utilising the conservation of the total momentum, U_{Wnew} of new steady jet solution expected to be realised after the merger is expected to be $U_{Wnew} \sim -1.363860$. The shape of isolated steady jet solution of $\gamma = 5.0, U_W = U_{Wnew}$ falls in with that of numerically realised jet after the merger well (not shown). Consequently, from the instability of the isolated zonal jet $\widetilde{U_{0new}}$, the final state of the two-jet state may be a uniform flow, same as the weakly-unstable type.

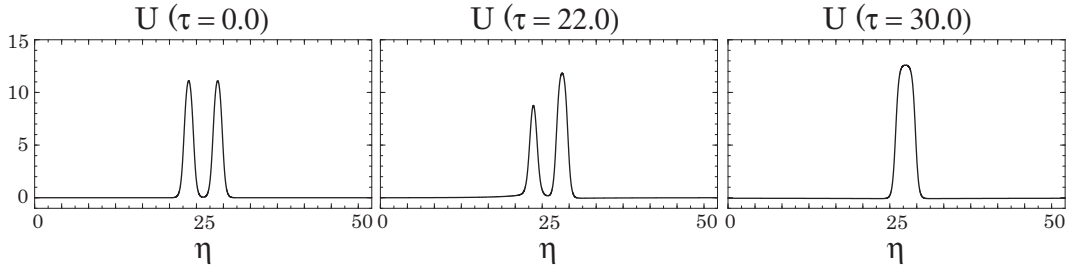

Figure 3.16: $\widetilde{U}$ of $\gamma = 5.0, U_W = -1.28$ at $\tau = 0.0,\ 22.0,\ 30.0$ (from the left to right).

[14]While the eigenvalue of $\widetilde{U_0}$ of $\gamma = 5.0, U_W = -1.28$ has been obtained by numerical calculation of its characteristic equation, that of $\widetilde{U_0}$ of $\gamma = 5.0, U_W = -1.28$ has been obtained by fitting other data because of a poor convergence of the eigenvalue calculation.

3.6 Modifications to the Manfroi-Young model

In §3.3 – §3.5, we have investigated the merging and disappearing processes of zonal jets through Manfroi-Young model. Although it is a highly simplified zonal flow – turbulence model, it seems to capture many fundamental dynamics zonal in two-dimensional turbulence on a rotating sphere and β plane. Here we modify the Manfroi-Young model to enquire into slightly more realistic situations. First, in §3.6.1, we add $\xi-$dependence to the Manfroi-Young equation and examine the linear stability of steady isolated zonal jets there. Then we consider zonal flows superposed upon a small-scale sinusoidal transversal flow in a quasi-geostrophic model, and perform the same asymptotic analysis which was employed in Manfroi and Young [16]. Both cases that the large-scale disturbance flow is $\xi-$independent and $\xi-$dependent are discussed in §3.6.2 and §3.6.3, respectively.

3.6.1 Two-dimensional barotropic model; x-dependent case

In the derivation of the amplitude equation of zonal flows, namely the Manfroi-Young equation (3.20), we have considered the ξ-independent solution $A(\eta, \tau)$ of Eq.(3.18), where ξ is $\xi \equiv \epsilon^6 x$ as introduced in (3.15). Although this specially idealised case is adequate for the first step to see the usefulness of the model and to study the zonal flows under the influence of non-zonal flow, real zonal jets observed in the long-time numerical simulations of two-dimensional Navier-Stokes turbulence on a rotating sphere in §2 and on a β plane in §3.2 are always governed by two-dimensional equations. In order to take this into account, here we consider the case that the solution A of Eq.(3.18) has ξ-dependence; $A(\xi, \eta, \tau)$.

Amplitude equation and its steady solution U_0

If we allow the solution A of Eq.(3.18) to be ξ-dependent, *i.e.* $A(\xi, \eta, \tau)$, the amplitude equation for the $O(1)$ elements of the x-independent but $\xi-$ and $\eta-$ dependent disturbance flow $U(\xi, \eta, \tau)$

$$U(\xi, \eta, \tau) \equiv -\frac{\partial A(\xi, \eta, \tau)}{\partial \eta},$$

is obtained as

$$\frac{\partial^3 U}{\partial\tau\partial\eta^2} = -(2-\gamma^2)\frac{\partial^4 U}{\partial\eta^4} - 3\frac{\partial^6 U}{\partial\eta^6} - 2\gamma\frac{\partial^4 U^2}{\partial\eta^4} + \frac{2}{3}\frac{\partial^4 U^3}{\partial\eta^4} - \beta_0\frac{\partial U}{\partial\xi}, \qquad (3.74)$$

by taking the derivative of Eq.(3.18) with respect to η, where γ is defined by (3.21). Eq.(3.74) governs $\xi-$ and $\eta-$ dependent flows having a small-scale sinusoidal transversal base flow in their background.

$U_{0east}(\eta)$ given by (3.35a) and $U_{0west}(\eta)$ given by (3.36a) in §3.3.2 again become steady isolated zonal jet solutions of Eq.(3.74). Now this $U_0(\eta)$ represents a zonal flow superposed upon a small-scale sinusoidal transversal background flow, governed by an amplitude equation having $\xi-$ and $\eta-$ dependence.

Linear stability of U_0

Let us investigate the linear stability of $U_0(\eta)$ in the $xi-$ dependent case. Same as in §3.4.1, we consider the situation in which a sufficiently small perturbation v is added to the steady solution $U_0(\eta)$, but this time $v = v(\xi,\eta,\tau)$. First, we assume v to be in the following form,

$$v = \exp(\sigma\tau)h(\xi)f(\eta),$$

where $h(\xi)$ and $f(\eta)$ are certain functions, which satisfy

$$h \to 0, \quad \frac{dh}{d\xi} \to 0 \quad as\ \xi \to \pm\infty, \qquad f \to 0, \quad \frac{df}{d\eta} \to 0 \quad as\ \eta \to \pm\infty.$$

Substituting $U = U_0 + v$ for U in Eq.(3.74), we linearise it with respect to v, then we have

$$\sigma h(\xi)\frac{\partial^2 f(\eta)}{\partial^2\eta} = h(\xi)\frac{d^4}{d\eta^4}\left\{[-(2-\gamma^2) + (2U_0^2 - 4\gamma U_0)]f - 3\frac{d^2 f}{d\eta^2}\right\} - \beta_0 f(\eta)\frac{dh(\xi)}{d\xi}. \qquad (3.75)$$

Assume that $\sigma \neq 0$. By integrating Eq.(3.75) over η twice, we find

$$\int_{-\infty}^{\infty}\int_{-\infty}^{\eta} f(\eta')d\eta'\ d\eta = 0^{15}$$

[15]We assume $d^2f/d\eta^2, d^3f/d\eta^3 \to 0$ $(\eta \to \pm\infty)$ as in Eq.(3.22a)

or

$$\frac{dh(\xi)}{d\xi} = 0.$$

As we are considering ξ-dependent case in this section, $dh(\xi)/d\xi \neq 0$, then

$$\int_{-\infty}^{\infty} f(\eta')d\eta' = 0.$$

Now rewriting $f(\eta)$ as

$$f(\eta) = \frac{d^2g(\eta)}{d\eta^2}, \quad g(\eta) \to 0, \quad \frac{dg(\eta)}{d\eta} \to 0, \quad \text{as } \eta \to -\infty.$$

We have

$$g(\eta) = g(\eta) - g(-\infty) = \int_{-\infty}^{\eta}\int_{-\infty}^{\eta'} \frac{d^2g(\eta'')}{d\eta''^2}\, d\eta''\, d\eta' = \int_{-\infty}^{\eta}\int_{-\infty}^{\eta'} f(\eta'')\, d\eta''\, d\eta'.$$

This means that, $g, dg/d\eta \to 0$ as $\eta \to \pm\infty$. Putting $f = d^2g/d\eta^2$ into Eq.(3.75), and integrating this equation over η twice, the characteristic equation is obtained as follows.

$$\sigma\frac{d^2g}{\partial d^2} = -(2-\gamma^2)\frac{d^4g}{d\eta^4} - 3\frac{d^6g}{d\eta^6} + \frac{d^2}{d\eta^2}\left[(2U_0^2 - 4\gamma U_0)\frac{d^2g}{d\eta^2}\right] - \beta_0 g(\eta)\frac{dh(\xi)}{d\xi}, \tag{3.76}$$

$$g \to 0, \quad \frac{dg}{d\eta} \to 0 \quad as\ \eta \to \pm\infty.$$

Incidentally, since the $\xi-$dependence in (3.76) only appear in a form $dh(\xi)/d\xi$, by considering a Fourier expansion of h

$$h(\xi) = \sum_{n_\xi=-\infty}^{\infty} h_{n_\xi} \exp\left(i\frac{2\pi n_\xi}{L_\xi}\xi\right),$$

it is sufficient to solve

$$\sigma\frac{d^2g}{\partial d^2} = -(2-\gamma^2)\frac{d^4g}{d\eta^4} - 3\frac{d^6g}{d\eta^6} + \frac{d^2}{d\eta^2}\left[(2U_0^2 - 4\gamma U_0)\frac{d^2g}{d\eta^2}\right] - i\frac{2\pi n_\xi}{L_\xi}\beta_0 g(\eta) \tag{3.77}$$

for various $2\pi\beta_0 n_\xi/L_\xi$, where L_ξ is a width of the domain in ξ direction.

Same as in §3.4, from the symmetry property of the characteristic equation, it easily follows that investigating the linear stability of U_{0east} with

$\gamma \geq 0$ is enough to know the linear stability of all the U_0 (See §A.5). Also, it is easily verified that the characteristic equation (3.77) holds also for $\sigma = 0$.

We solve the eigenvalue problem (3.77) numerically by the Fourier spectral method, where U_0, U_0^2, and g are expressed as

$$\begin{aligned} U_0 &= \sum_{k=-K}^{K} u_k \exp\left(ik\frac{2\pi}{L_\eta}\eta\right), \\ U_0^2 &= \sum_{k=-K}^{K} d_k \exp\left(ik\frac{2\pi}{L_\eta}\eta\right), \\ g &= \sum_{k=-K}^{K} c_k \exp\left(ik\frac{2\pi}{L_\eta}\eta\right). \end{aligned} \tag{3.78}$$

We consider the domain $[0, L_\eta]$ and a periodic boundary condition for η. The width of the domain, L_η, was determined so that the numerical calculation sufficiently converges [16]. The width of the spatial grids was set to be $1/(2^10)$, and the truncation mode number K was taken in the way that K/L_η becomes $125/16$ for each case.

Fig.3.17 shows the real parts of the leading eigenvalues for various $2\pi\beta_0 n_\xi/L_\xi$, for the cases $(\gamma, U_W) = (1.0, -1.0)$ and $(5.0, -1.0)$. The real parts of the leading eigenvalues are positive when $|2\pi\beta_0 n_\xi/L_\xi = 0|$ is smaller than certain value, which is depending upon (γ, U_W). So these mode grows in time. $2\pi\beta_0 n_\xi/L_\xi = 0$ which corresponds to $\xi-$independent case takes positive and the maximum value of the real parts of the leading eigenvalues for a fixed (γ, U_W), which means $\xi-$independent mode is most unstable and grows fastest. Meanwhile, non-growing mode appears in $\xi-$depending case (See the nested panels in Fig.3.17). Although it was not possible to solve the characteristic equation (3.77) for large $2\pi\beta_0 n_\xi/L_\xi$ since the continuous mode appears and the calculation does not converge there, from the shapes of the graphs, it may be reasonable to assume that the real part of leading eigenvalue for sufficiently large $2\pi\beta_0 n_\xi/L_\xi$ are all negative. This suggest that, U_0 only in small parameter regions are linearly unstable for a perturbation of limited $\xi-$ wavenumber. Still, there certainly is an sector in a parameter region of n_ξ around $n_\xi = 0$, where the perturbation grows in time, and this means that the steady isolated zonal jet solution U_0 is also unstable even

[16] We mainly took $L_\eta = 216$ and 512 for each case and confirmed the convergence of the calculations.

when it is governed by a $\xi-$depending equation so that allowed to have non-zonal variation. The instability is expected to bring about the deformation of U_0, and causes its disappearance. This is consistent with the disappearance of westward jet in full nonlinear two-dimensional simulations on β plane in §3.2.

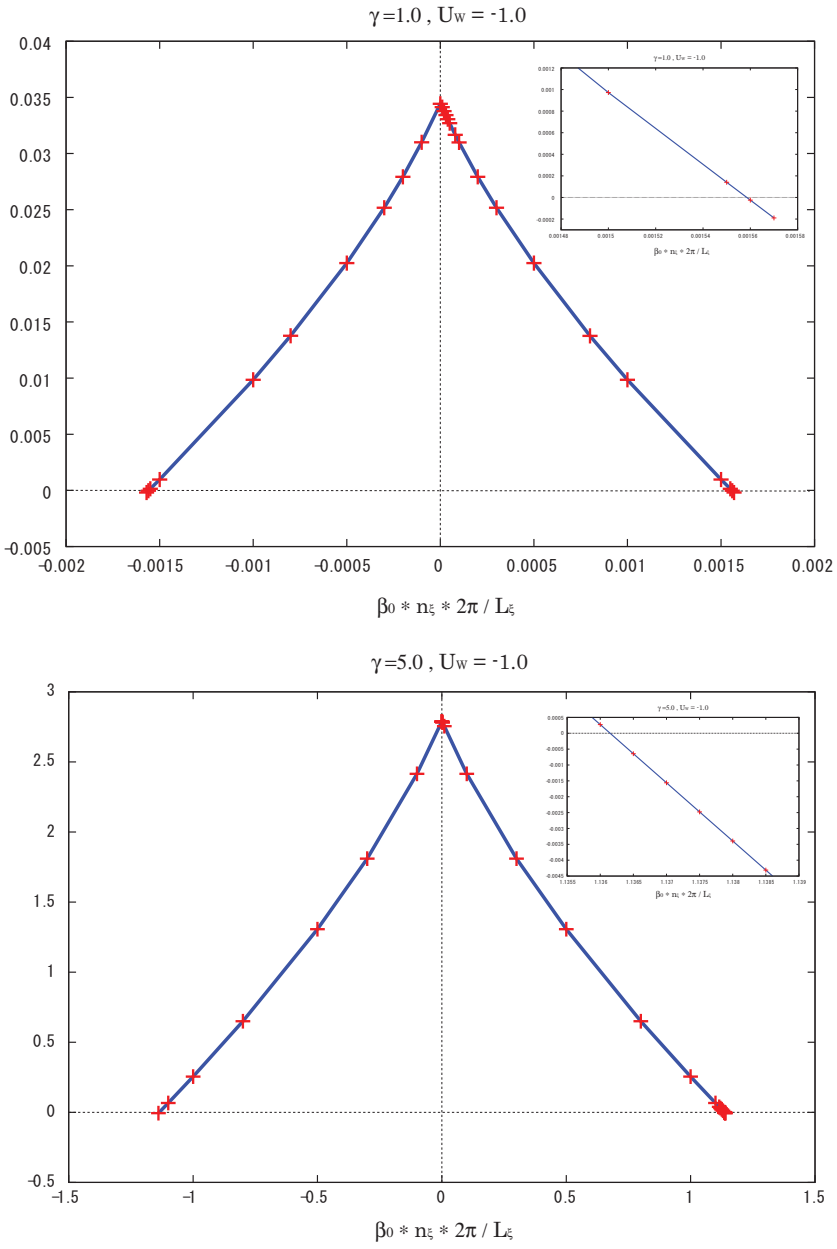

Figure 3.17: The real parts of the leading eigenvalues (red crosses) for $(\gamma, U_W) = (1.0, -1.0)$ (top) and $(5.0, -1.0)$ (bottom). The nested panel in each larger panel shows the region around one of two points where the real part of the leading eigenvalue becomes zero.

3.6.2 Quasi-Geostrophic model; x-independent case

Two-dimensional barotropic model describes the dynamics of a fluid with a constant density in a thin layer whose depth is constant both in time and in space, and sufficiently thinner than its horizontal scale. This is one of the most simple models used for large-scale flows on rotating systems. Very simple as the model is, it shows rich phenomena, including the formation of a zonal-band structure. The the zonal-band structure in the model, however, may be realised by a different mechanism from the one working in real planets such as Jupiter, for the multiple zonal-band structure in two-dimensional barotropic model does not survive and a structure with a few zonal jets is realised asymptotically §2. When we turn our eyes to more complicated models for planetary atmospheres, we notice that we nearly always observe zonal-band structures in the systems, but again, the mechanisms of their formation and the long-time behaviour are not yet well known. For this reason, now we modify the Manfroi-Young model to a system which contains a little bit more complexity than two-dimensional barotropic system. Consider a fluid with a constant density in one of the thin layers of a stratification on a rotating sphere, but this time, in contrast to the barotropic case, allows the layer to vary its depth both in time and space, then its dynamics is written in a shallow-water equations. The model still treats a two-dimensional dynamics but allows for divergence to take place. Further, we assume the situation that the rotation of the sphere is very strong *i. e.* the Rossby number

$$R_o \equiv \frac{\text{inertia}}{\text{rotation effect}} = \frac{U}{fL_x}$$

is sufficiently small, where U, f, and L_x are representative speed of the flow, Coriolis parameter, and the representative horizontal length scale of the flow. Expanding the shallow-water equations by R_o and collect terms $O(1)$ and $O(R_o)$, then the equations are called shallow-water quasi-geostrophic equations. For the small modification of the Manfroi-Young model, we next use this shallow-water quasi-geostrophic system.

Amplitude equation and its steady solution U_0

The analysis to derive an amplitude equation of $O(1)$ elements of the x-independent zonal flows having a small-scale sinusoidal transversal background flow is basically same as the one in the two-dimensional barotropic case in §3.3.

We consider an incompressible forced shallow-water quasi-geostrophic flow on a β plane where the governing equation for such flow is written as

$$\frac{\partial Z}{\partial t} + J(\Psi, Z) + \beta \frac{\partial \Psi}{\partial x} - \frac{1}{L_d^2}\frac{\partial \Psi}{\partial t} = F + \nu \nabla^2 Z. \tag{3.79}$$

Here t, Ψ, and $Z = \nabla^2 \Psi$ are the time, the stream function, and the vorticity. F and ν are the vorticity forcing function and the kinematic viscosity coefficient. $L_d \equiv gH/f_0^2$ is a Rossby radius of deformation, where g, H, and f_0 are gravitational acceleration, vertical width of a fluid layer, and Coriolis parameter at the reference latitude, respectively. $J(A, B)$ is the Jacobian operator: $J(A, B) \equiv (\partial A/\partial x)(\partial B/\partial y) - (\partial A/\partial y)(\partial B/\partial x)$, and $\nabla = (\partial/\partial x, \partial/\partial y)$.

We suppose a steady base flow with the velocity (3.7) is driven by a suitable forcing function on this β plane, and assume that the base flow is slightly unstable, that is, the Reynolds number of the base flow $R \equiv \Psi_{B0}/\nu$ is slightly larger than the critical Reynolds number R_c, as (3.8). Then we write the total stream function of the flow as $\Psi = \Psi_B(x) + \psi(x, y, t)$, where $\psi(x, y, t)$ is the stream function of the disturbance flow and, from the Eq.(3.79), satisfies a non-dimensionalised equation

$$\frac{\partial \hat{\zeta}}{\partial \hat{t}} + \hat{u}_B \frac{\partial \hat{\zeta}}{\partial \hat{x}} + R\left(\frac{\partial \hat{\zeta}}{\partial \hat{y}} + \frac{\partial \hat{\psi}}{\partial \hat{y}}\right)\sin \hat{x} + J(\hat{\psi}, \hat{\zeta}) + \hat{\beta}\frac{\partial \hat{\psi}}{\partial \hat{x}} - \frac{1}{L_d^2}\frac{\partial \hat{\psi}}{\partial \hat{t}} = \hat{\nabla}^2 \hat{\zeta}. \tag{3.80}$$

Here, $\zeta \equiv \nabla^2 \psi$ is the vorticity of the disturbance flow, $\hat{x}, \hat{y}, \hat{t}$, and $\hat{\psi}$ are non-dimensionalised variables given in (3.10). $\hat{u}_B$ and $\hat{\beta}$ are defined in (3.12), and $\hat{L_d} \equiv mL_d$. We, hereafter, drop the notation $\hat{}$ for the dimensionless variables and operators for simplicity.

Using the small parameter ϵ defined in (3.8), we now perform perturbation expansions of the stream function of the disturbance flow ψ, U_B, the β parameter, and $1/L_d$ by (3.13) and

$$\frac{1}{L_d} = \frac{1}{L_0} + \epsilon \frac{1}{L_1} + \cdots, \tag{3.81}$$

and multiple-scale expansion (3.14), and (3.15).

Substituting the expanded variables and operators (3.13), (3.14), 3.81, and (3.15) into Eq.(3.80), then we obtain Eq.(3.16) for the $O(1)$ elements. This is satisfied if ψ_0 depends on ξ, η, τ as $\psi_0 = A(\xi, \eta, \tau)$ as in (3.17). Substituting the expanded variables and operators (3.13), (3.14), 3.81, and

(3.15) into Eq.(3.80) again, we next take the x-mean of it. By gathering the $O(\epsilon^6)$ elements, we obtain

$$\begin{aligned}&\frac{\partial}{\partial\tau}\frac{\partial^2 A}{\partial\eta^2}-\frac{1}{L_1^2}\frac{\partial A}{\partial\tau}+2\frac{\partial^4 A}{\partial\eta^4}+3\frac{\partial^6 A}{\partial\eta^6}\\&-\frac{\partial^3}{\partial\eta^3}\left[\left(\beta_1-U_{B1}+\frac{\partial A}{\partial\eta}\right)^2\frac{\partial A}{\partial\eta}\right]+\frac{1}{3}\frac{\partial^3}{\partial\eta^3}\left(\frac{\partial A}{\partial\eta}\right)^3+\beta_0\frac{\partial A}{\partial\xi}=0.\end{aligned}\tag{3.82}$$

Taking the derivative of Eq.(3.82) with respect to η and considering the ξ-independent solution $A(\eta,\tau)$ of Eq.(3.82), we obtain the amplitude equation for the $O(1)$ elements of the x-independent disturbance flow $U(\eta,\tau)$ defined in (3.19) as

$$\frac{\partial^3 U}{\partial\tau\partial\eta^2}-\frac{1}{\mathrm{L}_1^2}\frac{\partial U}{\partial\tau}=-(2-\gamma^2)\frac{\partial^4 U}{\partial\eta^4}-3\frac{\partial^6 U}{\partial\eta^6}-2\gamma\frac{\partial^4 U^2}{\partial\eta^4}+\frac{2}{3}\frac{\partial^4 U^3}{\partial\eta^4},\tag{3.83}$$

where γ is again defined as (3.21). Eq.(3.83) governs zonal flows having a small-scale sinusoidal transversal background flow in the shallow-water quasi-geostrophic model. We call Eq.(3.83) the QG-Manfroi-Young equation.

$U_{0east}(\eta)$ given by (3.35a) and $U_{0west}(\eta)$ given by (3.36a) in §3.3.2 again become steady isolated zonal jet solutions of Eq.(3.83).

Linear stability of U_0

The characteristic equation for the situation when sufficiently small perturbation $v(\eta,\tau)$ of the form $v=\exp(\sigma\tau)f(\eta)$ is added to the steady solution $U_0(\eta)$ is derived completely in the same manner in §3.4.1:

$$\sigma\left[\frac{d^2}{d\eta^2}-\frac{1}{L_1^2}\right]g=-(2-\gamma^2)\frac{d^4 g}{d\eta^4}-3\frac{d^6 g}{d\eta^6}+\frac{d^2}{d\eta^2}\left[(2U_0^2-4\gamma U_0)\frac{d^2 g}{d\eta^2}\right].\tag{3.84}$$

Here g is the function which satisfies

$$v=\exp(\sigma\tau)f(\eta)=\exp(\sigma\tau)\frac{d^2 g(\eta)}{d\eta^2},$$

$$g\to 0,\quad \frac{dg}{d\eta}\to 0\quad as\ \eta\to\pm\infty.$$

Same as the two-dimensional case in §3.4.1, we solve the eigenvalue problem (3.84) numerically, by the Fourier spectral method, where U_0, U_0^2, g and

h are expressed by (3.39). We consider the domain $[0, L_\eta]$ and a periodic boundary condition for η. The width of the domain, L_η, was determined so that the numerical calculation converges sufficiently [17] The width of the spatial grids was set to be $1/2^10$, and the truncation mode number K was taken in the way that K/L_η becomes 125/16 for each case. The $O(\epsilon)$ element of Rossby radius of deformation, L_1, was express by taking the ratio of L_1 to L_J, the width of the steady zonal jet U_0 [18].

The real parts of the leading eigenvalues are shown in Fig.3.18. When L_1/L_J is large, the real part of the leading eigenvalue falls almost in line with that of U_0 in a barotropic system obtained in §3.4.1 (The pink line in Fig.3.18). This is because the vorticity equation of a shallow-water quasi-geostrophic model (3.79) reduces to that of a barotropic model (3.6) when $L_d \to \infty$. The real parts of the leading eigenvalue decreases as L_1/L_J decreases, and looks as if it covered to zero. Nevertheless, varying L_1/L_J only corresponds to looking at the same instability in a different time scale, and the real part of the leading eigenvalue is taking positive value, not zero, even when $L_1/L_J = 1.0 \times 10^{-6}$. To see this, let us define $\sigma_b \equiv \sigma\left[-(d^2/d\eta^2) + (1/L_1^2)\right]$. The characteristic equation (3.84) is written as

$$\sigma_b g = +(2-\gamma^2)\frac{d^4 g}{d\eta^4} + 3\frac{d^6 g}{d\eta^6} - \frac{d^2}{d\eta^2}\left[(2U_0^2 - 4\gamma U_0)\frac{d^2 g}{d\eta^2}\right]. \tag{3.85}$$

The Eq.3.85 gives a certain value of σ_b for a fixed (γ, U_w). Then $\sigma = \sigma_b/\left[-(d^2/d\eta^2) + (1/L_1^2)\right]$ takes various values when L_1/L_J is varied, but never takes minus value or precisely zero since σ' takes positive value as discussed in §3.4.1 – §3.4.2. In the limit of $L_1 \to 0$, σ becomes infinitesimal because $\sigma \sim \sigma_b/(1/L_1^2) \to 0$, but again, it has a positive value. This is certified by plotting the real parts of the leading eigenvalues divided by L_1^2, shown in Fig.3.19. We can see that the real parts of the leading eigenvalues divided by L_1^2 agrees with σ_b. Therefore, all the steady isolated jet solution U_0 are linearly unstable, same as the barotropic case in §3.4, though the instability is weaker compared to the barotropic case. Then again, the instability is expected to bring about the deformation of U_0, and causes its disappearance.

[17] We mainly took $L_\eta = 216$, and 512 for each case and confirmed the convergence of the calculations.

[18] We defined L_J, the width of U_0 to be $L_J \equiv 2\ell_{U_0}$, where ℓ_{U_0} satisfies $\left|\left[U_0(0) - U_0(\ell_{U_0})\right] / \left[U_0(0) - U_W\right]\right| = 1/\mathrm{e}$

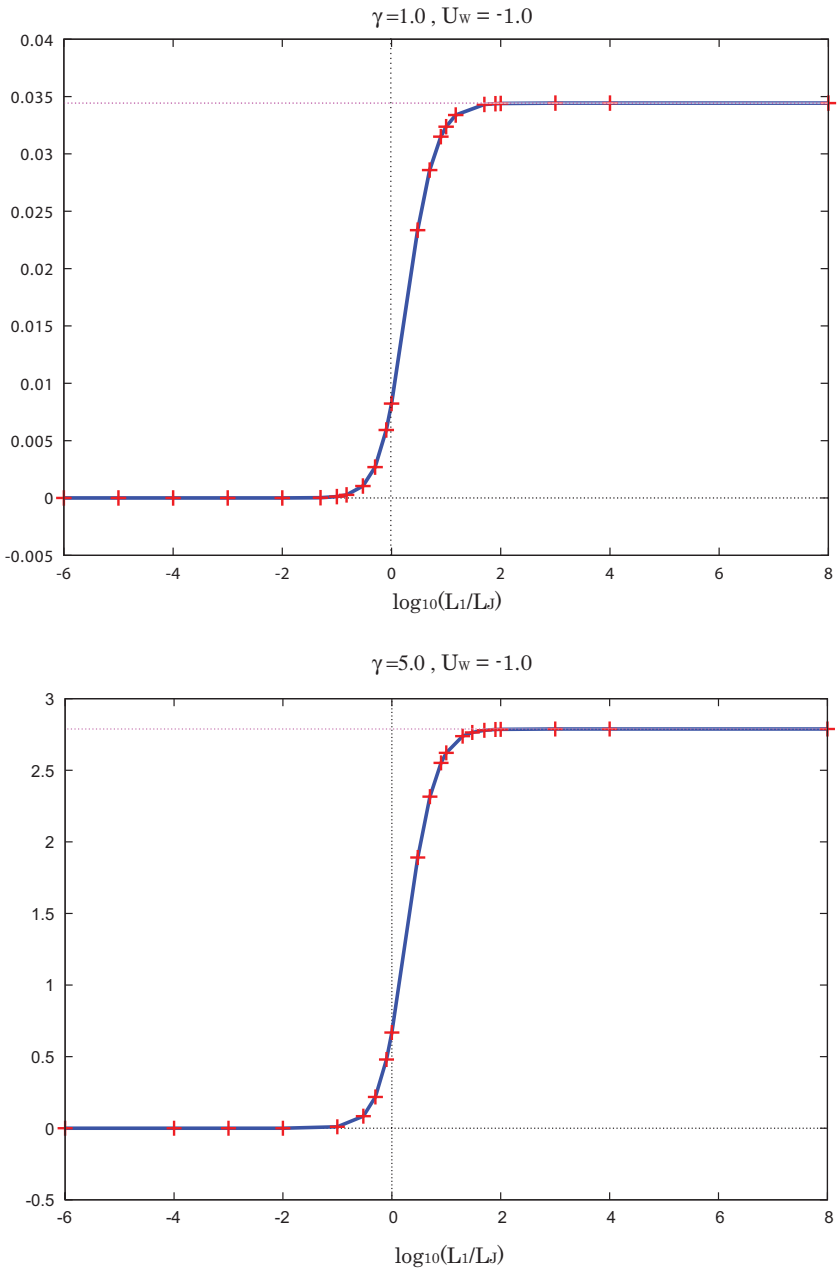

Figure 3.18: The real parts of the leading eigenvalues (red crosses) for $(\gamma, U_W) = (1.0, -1.0)$ (top) and $(5.0, -1.0)$ (bottom). The pink dotted line corresponds to the value of the eigenvalue of U_0 in a barotropic model.

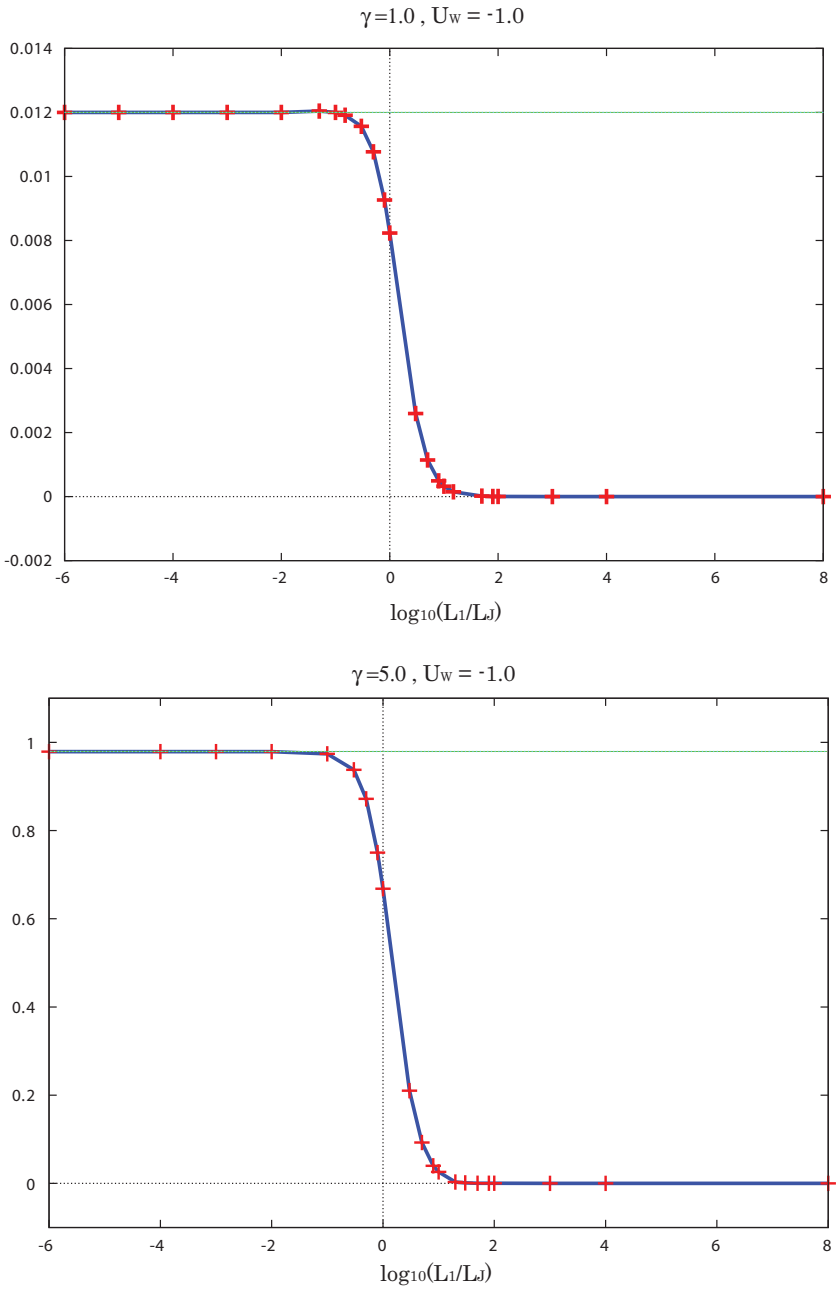

Figure 3.19: The real parts of the leading eigenvalues divided by L_1^2(red crosses) for $(\gamma, U_W) = (1.0, -1.0)$ (top) and $(5.0, -1.0)$ (bottom). The light blue dotted line corresponds to the value of σ_b

3.6.3 Quasi-Geostrophic model; x-dependent case

Same as the barotropic case, here, we consider the case that the solution A of Eq.(3.82) has ξ-dependence; $A(\xi, \eta, \tau)$.

Amplitude equation and its steady solution U_0

The amplitude equation for the $O(1)$ elements of the x-independent but $\xi-$dependent disturbance flow $U(\xi, \eta, \tau)$

$$U(\xi, \eta, \tau) \equiv -\frac{\partial A(\xi, \eta, \tau)}{\partial \eta},$$

is obtained as

$$\frac{\partial^3 U}{\partial \tau \partial \eta^2} - \frac{1}{L_1^2}\frac{\partial U}{\partial \tau} = -(2-\gamma^2)\frac{\partial^4 U}{\partial \eta^4} - 3\frac{\partial^6 U}{\partial \eta^6} - 2\gamma\frac{\partial^4 U^2}{\partial \eta^4} + \frac{2}{3}\frac{\partial^4 U^3}{\partial \eta^4} - \beta_0\frac{\partial U}{\partial \xi}, \quad (3.86)$$

This $U_0(\eta)$ represents a zonal flow superposed upon a small-scale sinusoidal transversal background flow governed by an amplitude equation having $\xi-$ and $\eta-$ dependence in shallow-water quasi-geostrophic system.

$U_{0east}(\eta)$ given by (3.35a) and $U_{0west}(\eta)$ given by (3.36a) in §3.3.2 again become steady isolated zonal jet solutions of Eq.(3.86). Now this $U_0(\eta)$ represents a zonal flow superposed upon a small-scale sinusoidal transversal background flow, governed by an amplitude equation having $\xi-$ and $\eta-$ dependence.

Linear stability of U_0

The characteristic equation for the situation when sufficiently small perturbation $v(\xi, \eta, \tau)$ of the form $v = \exp(\sigma\tau)h(\xi)f(\eta)$ is added to the steady solution $U_0(\eta)$ is derived completely in the same manner in §3.6.1, then written as

$$\sigma\left[\frac{d^2}{\partial d^2} - \frac{1}{L_1^2}\right]g = -(2-\gamma^2)\frac{d^4 g}{d\eta^4} - 3\frac{d^6 g}{d\eta^6} + \frac{d^2}{d\eta^2}\left[(2U_0^2 - 4\gamma U_0)\frac{d^2 g}{d\eta^2}\right] - i\frac{2\pi n_\xi}{L_\xi}\beta_0 g(\eta). \quad (3.87)$$

Here g is the function which satisfies

$$v = \exp(\sigma\tau)f(\eta) = \exp(\sigma\tau)\frac{d^2 g(\eta)}{d\eta^2},$$

$$g \to 0, \quad \frac{dg}{d\eta} \to 0 \quad as\ \eta \to \pm\infty,$$

L_ξ is a width of the domain in ξ direction, and $2\pi n_\xi / L_\xi$ is a wavenumber of mode $n_\xi \in \mathbb{N}$ of Fourier expansion of $h(\xi)$.

Same as the two-dimensional case in §3.6.1, we solve the eigenvalue problem (3.87) numerically by the Fourier spectral method, where U_0, U_0^2, and g are expressed by (3.78). We consider the domain $[0, L_\eta]$ and a periodic boundary condition for η. The width of the domain, L_η, was determined so that the numerical calculation converges sufficiently [19]. The width of the spatial grids was set to be $1/2^10$, and the truncation mode number K was taken in the way that K/L_η becomes 125/16 for each case. The $O(\epsilon)$ element of Rossby radius of deformation L_1 taken to be the width of the steady zonal jet U_0 [20].

Fig.3.20 shows the real parts of the leading eigenvalues for fixed γ, U_w, and $2\pi n_\xi \beta_0 / L_\xi$. For small enough $|2\pi n_\xi \beta_0 / L_\xi|$, the real parts of the leading eigenvalues monotonically decreases as L_1/L_j decreases, and the shape is similar to that of $\xi-$independent case in Fig.3.18. This is natural, because $2\pi n_\xi \beta_0 / L_\xi = 0$ corresponds to $\xi-$independent case. On the other hand, for larger $|2\pi n_\xi \beta_0 / L_\xi|$, the parts of the leading eigenvalues take the maximum values at $L_1/L_J \sim 10^{1/2}$. The bump becomes higher as $|2\pi n_\xi \beta_0 / L_\xi|$ becomes larger, but the real part of the leading eigenvalue of larger $|2\pi n_\xi \beta_0 / L_\xi|$ does not become larger than that of smaller $|2\pi n_\xi \beta_0 / L_\xi|$ even at $L_1/L_J \sim 10^{1/2}$, so the real parts of the leading eigenvalues for a fixed $L1/L_J$ monotonically decreases as $|2\pi n_\xi \beta_0 / L_\xi|$ increases. We will check this again in Fig.3.21 later. The mechanism of the appearance of the bump is not clear, and the structure of the eigenfunctions shows no apparent change from those of large or small $|2\pi n_\xi \beta_0 / L_\xi|$. Now, paying attention only to the region where $L1/L_J$ is small, all the real parts of the leading eigenvalues look as if they converge to zero. From the same reason stated in the $\xi-$independent case in §3.6.3, they do not become zero but take positive values for the values of $|2\pi n_\xi \beta_0 / L_\xi|$ shown in Fig.3.20. This analysis cannot be used for the case with much larger $|2\pi n_\xi \beta_0 / L_\xi|$, though. This will be discussed by using Fig.3.21 later.

Now, the plot of the the real parts of the leading eigenvalues for fixed γ, U_w, and L_1/L_J is shown in Fig.3.21. For both L_1/L_J where real parts

[19] We mainly took $L_\eta = 216$, and 512 for each case and confirmed the convergence of the calculations.

[20] We defined the width of U_0 to be $2\ell_{U_0}$, where ℓ_{U_0} satisfies $|\,[U_0(0) - U_0(\ell_{U_0})]\,/\,[U_0(0) - U_W]\,| = 1/\mathrm{e}$

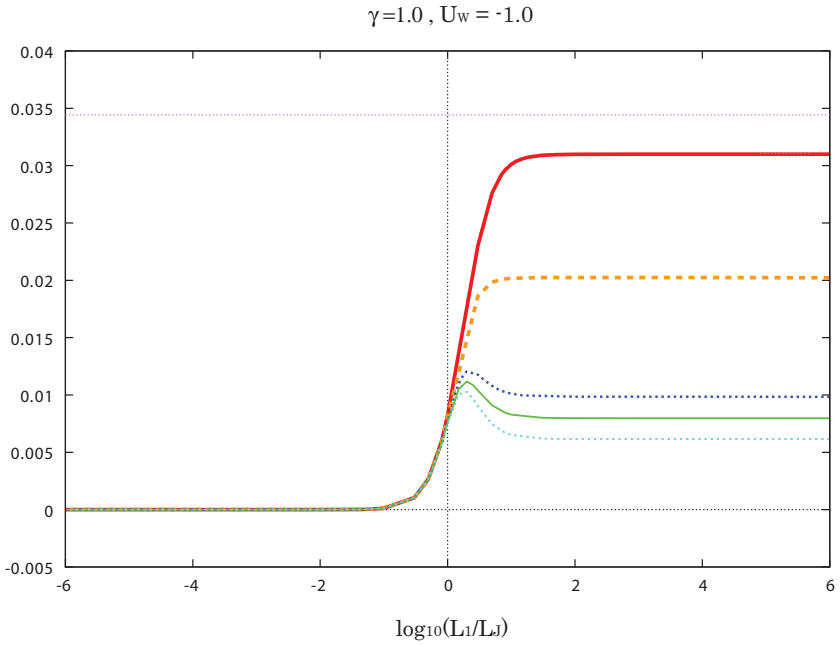

Figure 3.20: The real parts of the leading eigenvalues for $\gamma = 1.0, U_W = -1.0$), $2\pi n_\xi \beta_0 / L_\xi = 1.0 \times 10^{-4}$ (red thick solid line), 5.0×10^{-4} (orange thick dashed line), 1.0^{-3} (Blue thick dotted line), 1.1×10^{-3} (green thin solid line), and 1.2×10^{-3} (light blue thin dotted line). The pink dotted line corresponds to the eigenvalue of the $\xi-$independent barotropic case.

of the leading eigenvalues may or may not take a maximum value for fixed $|2\pi n_\xi \beta_0 / L_\xi|$ in Fig.3.20, the real parts of the leading eigenvalue monotonically decreases as $|2\pi n_\xi \beta_0 / L_\xi|$ increases, and takes the maximum value at $2\pi n_\xi \beta_0 = 0$. This certifies that the real part of the leading eigenvalue at the higher bump of larger $|2\pi n_\xi \beta_0 / L_\xi|$ does not become larger than that of smaller $|2\pi n_\xi \beta_0 / L_\xi|$ in Fig.3.20. We could not obtain the eigenvalue for large $|2\pi n_\xi \beta_0 / L_\xi|$ because continuous modes appear and the numerical calculation does not converge there. However, from the shape of the graph, it may be reasonable to expect the real parts of the leading eigenvalue to be negative at sufficiently large $|2\pi n_\xi \beta_0 / L_\xi|$. There are some differences between ξ-depending case in the shallow-water quasi-geostrophic system discussing here and $\xi-$depending case in the barotropic system in §3.6.1, for example, the real parts of the leading eigenvalues does not have a cusp at $2\pi n_\xi \beta_0 / L_\xi = 0$ now whilst it does in the barotropic case in §3.6.1, and the instability for

the same γ, U_w, and L_1/L_J is weaker than that of the barotropic case. However, the essential facts are the same as the $\xi-$depending barotropic case; U_0 certainly is linearly unstable. The instability is expected to bring about the deformation of the steady isolated zonal jet U_0 and causes its disappearance.

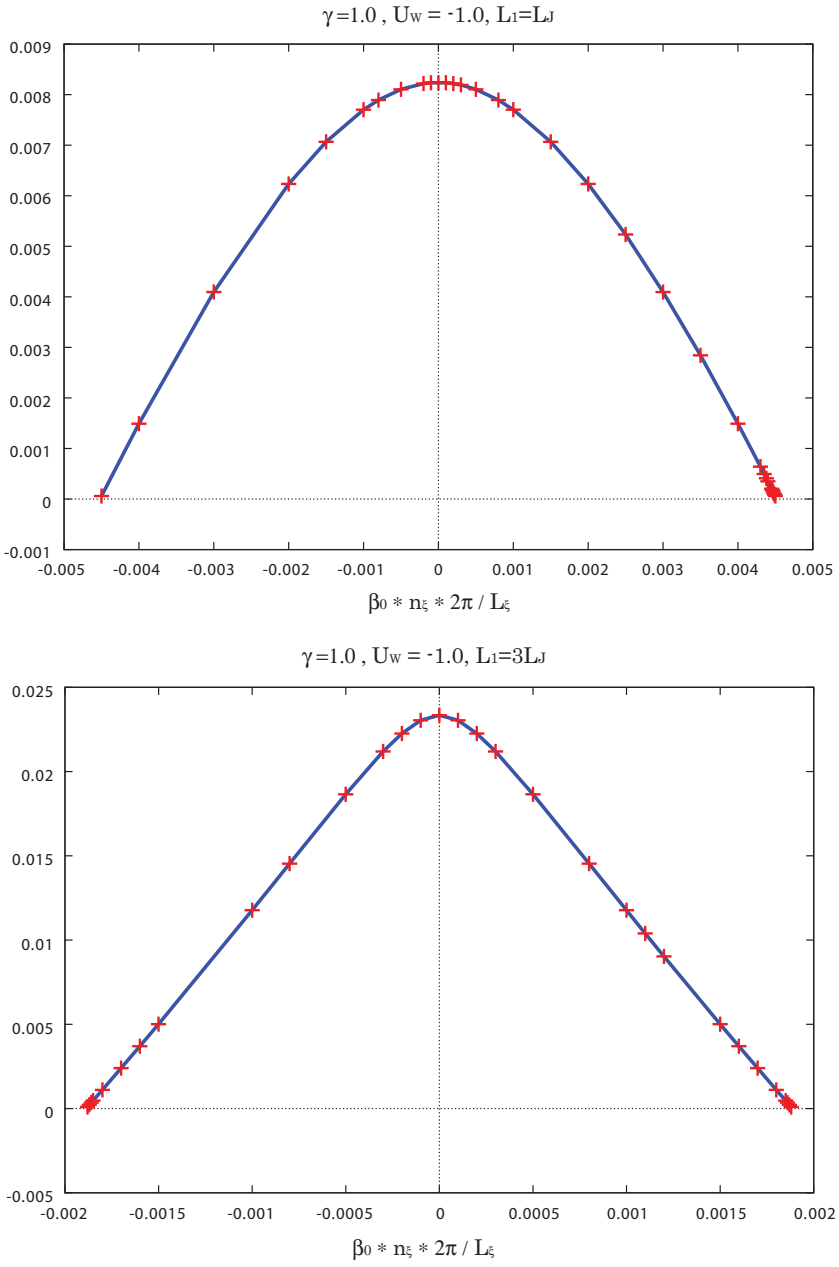

Figure 3.21: The real parts of the leading eigenvalues (red crosses) for $\gamma = 1.0,\ U_W = -1.0,\ L_1/L_J = 1.0$(a) and 3.0(b).

3.7 Discussions and Conclusions

In this chapter, we have examined the merging and the disappearing processes observed in a long-time development of zonal jets on a rotating sphere and β plane, by considering a simpler model of zonal jets with a non-zonal background flow on a β plane.

Firstly in §3.2, it was confirmed that the intermittent mergers and disappearances of zonal jets is also seen in two-dimensional turbulence on a β plane, and such dynamics of fully developed zonal jets cannot be explained in the framework of the laminar zonal flow because of the instability of laminar zonal jet whose representative scale is larger than the Rhines scale. For this reason, the effect of the background turbulence is inevitable for the theory of mergers and disappearances of such zonal jets in two dimensional turbulence in rotating systems.

To investigate zonal jets under the influence of turbulence, we have considered zonal jet flows on a β plane subject to the effect of a background small-scale sinusoidal transversal flow in §3.3 – §3.5. This model is originally introduced by Manfroi and Young[16], and the evolution equation of such zonal flow is given in Manfroi-Young equation (Manfroi and Young[16]).

Analytical solutions of steady isolated zonal jet of Manfroi-Young equation were obtained in §3.3.2. The solution U_0 exists in certain regions of a parameter space, and is uniquely determined by fixing two parameters.

In order to investigate the disappearing mechanism of zonal jets, the linear stability of U_0 was investigated both numerically and partially analytically, and it was found that the steady isolated zonal jet solutions U_0 are all linearly unstable. Numerical time integrations of the evolution equation also showed that the perturbed unstable steady jet solution gradually decreases its amplitude, and becomes a uniform flow in the long run (§3.4).

Comparing the results shown in §3.4 to the numerical experiment performed by Manfroi and Young [16], there seems to be a disagreement at first sight. Every steady jet solution is linearly unstable, whilst the jets appear in the numerical simulation in Manfroi and Young [16] disappear one by one quite deliberatively, ending up with one jet in the considering domain at the final stage.

This disagreement may be caused by the fact that the leading eigenvalues have zeros of second order on the curves (3.29a), (3.29b), (3.31a), and (3.31b). In Manfroi and Young [16], they only fixed γ in advance in their numerical simulation, where U_W was "selected" spontaneously by the system

itself and the resultant parameters (γ, U_W) was very close to the boundary curve (3.29a), which suggests that the zonal jets in the simulation are almost marginally stable. This implies that although the jets seen in the numerical simulation in Manfroi and Young [16] really were linearly unstable, their instability was very weak and the jets have behaved as if they had been linearly stable.

Concerning the difference between the analyses in Manfroi and Young [16] and our study, we also have to mention the differences of the boundary condition. The solution in Manfroi and Young [16] is affected by the periodic boundary condition, and alternative eastward westward jets rather than an isolated jet are observed. We, on the other hand, perform the analyses in the infinitely extended domain. For the calculations of the eigenvalue problems and numerical time integrations, we take a sufficiently large computational domain in order that the amplitude of disturbances may vanish when it is far from the isolated jets. Note that the eigenfunction decays spatially slower than the jet. The periodic boundary condition allows the baseline shift of the jet profile, which does not occur when the equation is considered in an infinite domain. Therefore, strictly speaking, the result of our analyses cannot be applied to the final state of their solution.

Nevertheless, we may find a point of our result consistent with the numerical experiment by Manfroi and Young [16]. Disappearance of the thin jet seen in Fig.3 in Manfroi and Young [16] at $\tau = 500$–600 may be caused by the intrinsic instability of the jet obtained in the present study, firstly because the baseline of the jet does not vary during the disappearance of the jet, consistently with the presumption of our analysis, and secondary because the stability of the thin jet is considered not to be affected by the adjacent jets, as the eigenfunction of the unstable disturbance is concentrated around the basic jet (Fig.3.10).

For the merging process of zonal jets, again, we have considered the steady isolated zonal jet solutions of Manfroi-Young equation, and have estimated a weak interaction (Ei [19]) between two identical zonal jets U_0 by a perturbation method, and calculated time derivative of the distance between two zonal jets $\dot{h}_P$ in §3.5. It has been found that the two identical zonal jets placed apart (two-jet state) attract each other, and the attraction becomes stronger as the distance between them gets shorter. The result is consistent with the behaviour of two jets and and the time derivative of the distance between them $\dot{h}_N$, obtained by a numerical time integration of the Manfroi-Young equation. There is a slight disagreement between $\dot{h}_P$ and $\dot{h}_N$ in terms

of numerical values, though. This had not been improved by changing any parameter used to obtain $\dot{h}_P$ and $\dot{h}_N$. The biggest reason for this may arises from the linear instability of a steady isolated jet U_0. Although U_0 we have used are nearly marginally stable, the deformation of them, especially around the centres of their bumps, may have not been small enough to neglect. This can bring some errors when the distance between two jets is measured from the full nonlinear numerical simulation. Even though, the result obtained here still strongly suggests that the weak interaction between two neighbouring jets through their tails is essential for their attraction of each other.

We have also investigated the strong nonlinear stage and the final state of two-jet state seen after a fairly long weak nonlinear stage. For the case that the linear instability of the steady isolated zonal jet solution U_0 is weak, when the distance between two jets becomes small enough, the jets promptly merge to one larger jet. This larger jet then survives for a very long time, keeping its shape. However, as this new jet is a steady isolated zonal jet solution U_0 of the same γ but different U_W, it may gradually decreases its amplitude and finally becomes a uniform flow, because of its linear instability discussed in §3.4. Meanwhile, in the case that the linear instability of the steady isolated jet is strong, when the distance between two jets becomes small enough, one of the jets disappears by being 'absorbed' into the other one. This may be what has happened in the numerical simulation performed by Manfroi and Young [16].

The total result found in §3.5 is consistent with gradual mergers and disappearances of zonal jets seen in the forced two-dimensional barotropic incompressible flows on a rotating sphere and on β plane; the mergers and disappearances takes longer time when the distance between the adjacent jets is larger; the mergers and disappearances take place quickly after the distance between the adjacent jets becomes short enough; and the zonal jets survives much longer time when they become a larger jet after having experienced several mergers and disappearances. This may suggests that the weak interaction between neighbouring jets can be essential to the jets mergers and disappearances as well as their intrinsic instability discussed in §3.4.

Then finally, we have made small modifications to Manfroi-Young model by taking account of the spatial variation of the disturbance in the zonal direction, and the surface variation of the fluid layer in §3.6. The Manfroi-Young model considers a special case that the zonal flow superposed upon a small-scale sinusoidal flow is governed by an amplitude equation that does not

have $x-$direction dependence. The real zonal jets in two-dimensional turbulence, on the contrary, is governed by two-dimensional governing equations. Hence in §3.6.1, we have considered the linear stability of steady isolated zonal jet solution U_0 when it is allowed to have a non-zonal variation. For another way to modify the Manfroi-Young equation, we have allowed the fluid to have divergence *i. e.* allow the fluid layer depth to have a slight variation both in time and space. We have performed an asymptotic analysis following the Manfroi and Young [16] in a shallow-water quasi-geostrophic system, and studied the linear stability of steady isolated zonal jet solution U_0 in §3.6.2 when it is governed by an amplitude equation independent of $x-$direction, and §3.6.3 when its amplitude equation has $x-$direction dependence.

It was found that U_0 is linearly unstable for three cases stated above. Long-time behaviour and the final state of the steady isolated zonal jet U_0 in these systems, especially when the U_0 is allowed non-zonal variation, is the problem desired to be clarified, and this is now under investigation.

Chapter 4

Conclusion

In this thesis, long-time behaviour of zonal jets in two-dimensional turbulence on both a rotating sphere and β plane was considered, and the mechanisms of mergers and disappearances of zonal jets was investigated by an asymptotic analysis on a β plane.

In two-dimensional turbulence on a rotating sphere, a structure with alternating eastward and westward jets, namely a multiple zonal-band structure, emerges from a randomly perturbed small-scale flow filed, in the course time development. The multiple zonal-band structure then experiences intermittent mergers and disappearances of zonal jets, and at the final stage of the time integration, a zonal-band structure with only a few (two or three) large-scale zonal jets is realised. The merger and disappearance of zonal jets is also seen in a simpler model, *i.e.*, two-dimensional turbulence on β plane, and it is one of the most outstanding properties of long-time behaviour of two-dimensional turbulence in rotating systems. The mechanism of the process, however, is not yet well understood, and one essential point we have to notice is that this is not explained in the framework of laminar flows because of the linear stability of large-scale laminar zonal jets. As a consequence, it is inevitable to take the effect of turbulence into the theory for zonal jets in an analytically treatable way when we hope to understand the long-time behaviour of zonal jets on a rotating sphere and β plane.

The simple model for a zonal flows superposed upon a homogeneous flow and a small-scale sinusoidal transversal background base flow, originally introduced by Manfroi and Young [16], is one of the most successful models in order to inspect the dynamics of zonal flows under the influence of turbulence. By utilising a deterministic forcing instead of turbulence whose

properties are stochastic, the model enables us to investigate the dynamics of zonal flows analytically to some extent.

Manfroi and Young has derived the time evolution amplitude equation of a zonal flow with a small-scale background flow (the Manfroi-Young equation), by utilising a multiple-scale expansion technique. From their numerical experiments, when the bottom drag is absent, it is known that a multiple zonal-band structure emerges from a random initial flow, and the gradual disappearances of the zonal jet occur one by one, forming a structure with one thin eastward jet and one broad westward jet in the considered periodic domain. Since the evolution of the zonal-band structure seen in their numerical experiment is similar to long-time behaviour of zonal jets on a rotating sphere or β plane, we may deduce some physical insight about the merging and the disappearing process of zonal flows induced by small-scale stochastic forcing by examining this system.

Therefore in the main part of this thesis, we first have derived an analytical steady solution of the Manfroi-Young equation in the form of isolated zonal jet with one bump and having a constant value at sufficiently far field. The solution, U_0, was found to exist in certain regions of a parameter space, and to be uniquely determined by fixing two parameters.

Then, by examining a linear stability of U_0, we have discussed the disappearing process of zonal jets. It was numerically confirmed that U_0 is linearly unstable for all the parameter regions where it can exist. The distribution of leading eigenvalues are partially proved analytically, too. It was also shown by a numerical long-time integration of the evolution equation, the perturbed unstable steady jet solution U_0 gradually decreases its amplitude, and becomes a uniform flow in the long run. The disappearing process of U_0 in this numerical simulation agrees well with the disappearing process of zonal flows in the Manfroi and Young's numerical experiment, and this is also consistent with disappearance of zonal jets in two-dimensional turbulence on a rotating sphere and β plane. The result suggests the possibility of the zonal jets' disappearance because of their intrinsic instability in two-dimensional turbulence in rotating systems.

The merging process of the neighbouring zonal jets was investigated by considering the weak interaction between two identical steady zonal jet solutions U_0 placed apart (two-jet state) through their tails. Applying a reduction theory to the interaction between two U_0, we have analytically estimated the time derivative of the distance between two zonal jets: $\dot{h}_P$. Using the analytical notation of $\dot{h}_P$, it has been numerically certified that the two iden-

tical zonal jets placed apart attract each other, and the attraction becomes stronger as the distance between them gets shorter. The result is consistent with the behaviour of two jets and the time derivative of the distance between tow jets $\dot{h}_N$, obtained by a numerical time integration of the two-jet state governed by the Manfroi-Young equation. The strong nonlinear stage and the final state of the two-jet state was also investigated numerically, and it was found that two zonal jets attract each other, and merge at the centre of their original position when the instability of U_0 is weak enough, whilst one of the two zonal jets is absorbed into the other one when the instability of U_0 is strong.

The result is consistent with gradual mergers and disappearances of zonal jets seen in forced two-dimensional turbulence on a rotating sphere and β plane; the mergers and disappearances takes longer time when the distance between the adjacent jets is larger; the mergers and disappearances take place quickly after the distance between the adjacent zonal jets becomes short enough; and the zonal jets survives much longer when they become a larger jet after having experienced several mergers and disappearances. This may suggests that the weak interaction between neighbouring jets can be essential to the jets mergers and disappearances as well as their instability caused by the effect of turbulence.

Futhermore, we have made small modifications to Manfroi-Young model by taking account of the spatial variation of the disturbance in the zonal direction, and the surface variation of the fluid layer. Note that in real two-dimensional turbulence, zonal flows are always governed by a two-dimensional equations, whilst the Manfroi-Young equation only possesses $y-$direction dependence. It was found that U_0 is linearly unstable even when it is allowed a non-zonal variation or when the depth of total flow layer is not constant as two-dimensional barotropic case but allowed to slightly vary both in time and space. This implies that the instability of zonal flow is a common property of wide range of systems on a β plane. The long-time behaviour and the final state of the steady isolated zonal jet U_0 in these systems, especially when the U_0 is allowed non-zonal growth variation, is the problem desired to be clarified, and this is now under investigation.

Although the results described in this thesis are consistent with the long-time behaviour of zonal jets in two-dimensional turbulence in rotating systems, and seem to be suggesting partially reasonable explanation to them, the applicability of the results of the study here to the mergers and disappearances of the zonal jets in the problems of stochastically forced two-

dimensional turbulence on a rotating sphere (§2) or β plane (Chekhlov *et al.* [8], §3.2) is not clear, because the background turbulence in these case consists of a lot of wavy modes varying in time, and the background single sinusoidal flow adopted in this study may be too simple to incorporate the effect of turbulence. However, the notion of the instability of zonal jets caused by the background small-scale non-zonal flow and the attraction between neighbouring zonal jets by the weak interaction through their tails appear to work in the complex flow at least phenomenologically, and deserves further investigation.

Appendices

A.1 Treatment of liner terms in the governing equation (2.1) in numerical calculations in §2

In the numerical time integration of Eq.(2.1) in §2, linear terms are analytically treated in advance. Here we introduce the method used in §2.

When using a spectral method with the spherical harmonics Y_n^m whose total wavenumber n and zonal wavenumber m, the stream function ψ, the vorticity ζ, and the forcing function F are expanded as

$$\begin{aligned}
\psi(\phi,\mu,t) &= \sum_{n=0}^{N_T} \sum_{m=-n}^{n} \psi_n^m(t) Y_n^m(\phi,\mu), \\
\zeta(\phi,\mu,t) &= \sum_{n=0}^{N_T} \sum_{m=-n}^{n} \zeta_n^m(t) Y_n^m(\phi,\mu), \\
F(\phi,\mu,t) &= \sum_{n=0}^{N_T} \sum_{m=-n}^{n} F_n^m(t) Y_n^m(\phi,\mu).
\end{aligned} \tag{A.1}$$

Here, N_T is the truncation wavenumber, and ψ_n^m, ζ_n^m, F_n^m are the expansion coefficients. Substituting the expansion (A.1) into Eq.(2.1), multiplying ${Y_{n'}^{m'}}^\dagger$ to both hand sides of the equation, and integrating it in a whole domain, we obtain

$$\frac{\partial \zeta_n^m}{\partial t} + \frac{1}{a^2}[J(\psi,\zeta)]_n^m + \frac{2\Omega}{a^2}\left[\frac{\partial \psi}{\partial \phi}\right]_n^m = F_n^m + \nu\,\frac{-n(n+1)+2}{a^2}\,\zeta_n^m. \tag{A.2}$$

Here, $[J(\psi,\zeta)]_n^m$ and $[\partial\psi/\partial\phi]_n^m$ are the spherical harmonics expansions coefficients of $J(\psi,\zeta)$ and $\partial\psi/\partial\phi$, respectively.

Noticing $\zeta = \nabla^2\psi$ so that

$$\left[\frac{\partial\psi}{\partial\phi}\right]_n^m = -\frac{a^2 m}{n(n+1)}\ \zeta_n^m$$

holds, and introducing the phase velocity of the Rossby wave

$$v_R(n,m) \equiv -\frac{2\Omega m}{n(n+1)},$$

and

$$-\nu^* \equiv \nu\frac{-n(n+1)+2}{a^2},$$

Eq.(A.2) is rewritten as

$$\frac{\partial\zeta_n^m}{\partial t} = -\frac{1}{a^2}[J(\psi,\zeta)]_n^m + v_R(n,m)\ \zeta_n^m + F_n^m - \nu^*\zeta_n^m. \tag{A.3}$$

Now we introduce

$$\hat{\zeta}_n^m(t) \equiv \zeta_n^m(t)\ \exp[(-v_R(n,m)+\nu^*)\ t\ ], \tag{A.4}$$

then the left and right hand sides of Eq.(A.3) become

$$(v_R-\nu^*)\hat{\zeta}_n^m\ \exp[-(-v_R(n,m)+\nu^*)t] + \frac{\partial\hat{\zeta}_n^m}{\partial t}\exp[-(-v_R(n,m)+\nu^*)t],$$

and

$$-\frac{1}{a^2}[J(\psi,\zeta)]_n^m + F_n^m + (v_R(n,m)-\nu^*)\ \hat{\zeta}_n^m\ \exp[-(-v_R(n,m)+\nu^*)t],$$

respectively. Consequently, from Eq.(A.3), we obtain

$$\frac{\partial\hat{\zeta}_n^m}{\partial t} = \left(-\frac{1}{a^2}[J(\psi,\zeta)]_n^m + F_n^m\right)\exp[(-v_R(n,m)+\nu^*)\ t\ ]. \tag{A.5}$$

After all, what we have to do for the time integration of Eq.(2.1) is calculating $\hat{\zeta}_n^m(t)$ by performing the time integration of Eq.(A.5), and obtain $\zeta_n^m(t)$ through Eq.(A.4) in every time step.

A.2 Convergence of the numerical calculations in §2

The convergence of the numerical simulations in §2 has been checked by performing calculations with different parameters; $\Delta t = 0.025$, which is half of the one used here; the truncation wavenumber $N_T = 341$ and the spatial grid points 1024×512 which realises almost twice higher resolution than the original one.

Temporal developments of zonal-mean zonal angular momentum $\overline{[L_{lon}]}$ of run 4 with different conditions for numerical simulation are shown in Fig.A.1. Although the details of the temporal development of zonal jets are different, the general tendency, the appearance of zonal-band structure in the first stage of time integration and the realisation of an asymptotic state with two zonal jets through mergers and disappearances of zonal jets, are common for three simulations. This suggest that these common properties are independent of conditions of numerical simulation. Note that which hemisphere is covered by an eastward jet in the asymptotic state strongly depends on the random force given to the system so that it is natural that different hemisphere is covered by an eastward jet for the different numerical simulations.

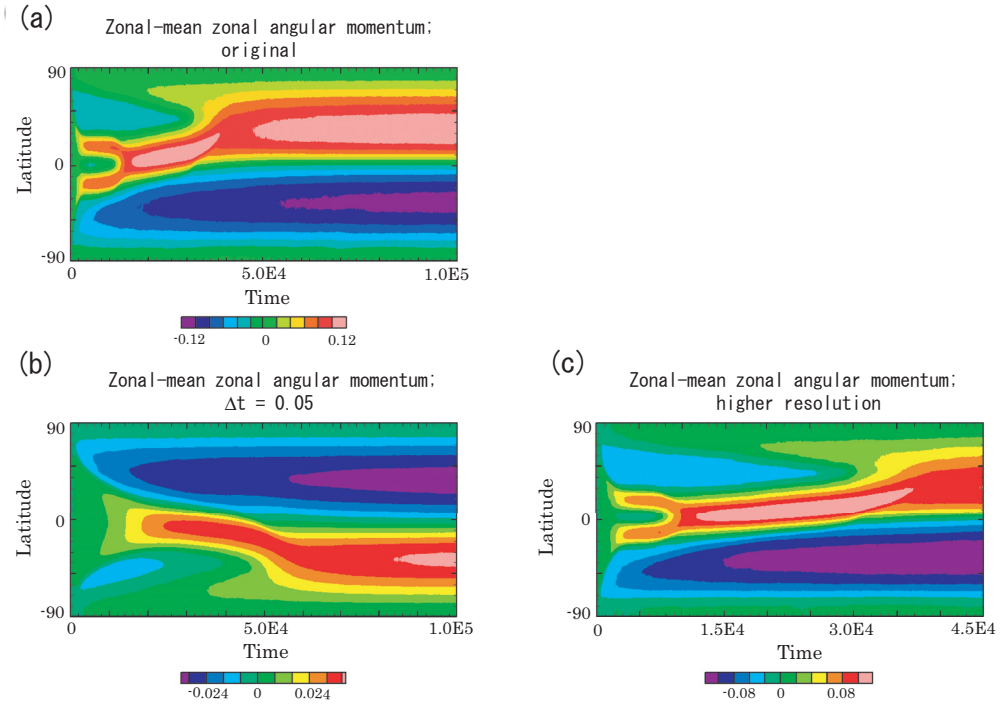

Figure A.1: The temporal development of zonal-mean zonal angular momentum $[\overline{L_{lon}}]$ by calculations with different time step width Δt, truncation wavenumber N_T, and the number of spatial grid points. Rest of the parameters are all set to be the same as those of run 4. (a): The original calculation (run 4). (b): $\Delta t = 0.025$, which is half of the one used in the original calculation. (c): $N_T = 341$ and the spatial grid points 1024×512 which realise almost twice higher resolution than the original calculation(This calculation is performed only to $t = 4.5 \times 10^4$).

A.3 Treatment of liner terms in the governing equation (3.1) in numerical calculations in §3.2

Here we introduce the method to treat the linear terms of Eq.(3.1) analytically in advance, used when we perform the numerical time integration of Eq.(3.1) in §3.2. The manner is almost same as that described in §A.1.

First, we perform double Fourier expansions to the stream function ψ, the vorticity ζ, and the forcing function F:

$$\begin{aligned}
\psi(x,y,t) &= \sum_{k_x=-K_{xT}}^{K_{xT}} \sum_{k_y=-K_{yT}}^{K_{yT}} \psi_{k_x,k_y}(t)\ \exp(ik_x\ x)\ \exp(ik_y\ y), \\
\zeta(x,y,t) &= \sum_{k_x=-K_{xT}}^{K_{xT}} \sum_{k_y=-K_{yT}}^{K_{yT}} \zeta_{k_x,k_y}(t)\ \exp(ik_x\ x)\ \exp(ik_y\ y), \\
F(x,y,t) &= \sum_{k_x=-K_{xT}}^{K_{xT}} \sum_{k_y=-K_{yT}}^{K_{yT}} F_{k_x,k_y}(t)\ \exp(ik_x\ x)\ \exp(ik_y\ y),
\end{aligned} \tag{A.6}$$

where $K_{xT},\ K_{yT}$ are the truncation mode numbers, and $\psi_{k_x,k_y},\ \zeta_{k_x,k_y},\ F_{k_x,k_y}$ are the the expansion coefficients. Substituting the expansions (A.6) into Eq.(3.1), multiplying $\exp(-ik'_x\ x)\ \exp(-ik'_y\ y)$ to both hand sides of the equation, and integrating it in a whole domain, we obtain

$$\frac{\partial \zeta_{k_x,k_y}}{\partial t} + \left[J(\psi,\zeta)\right]_{k_x,k_y} + \left[\beta\frac{\partial \psi}{\partial x}\right]_{k_x,k_y} = F_{k_x,k_y} - \nu\ ({k_x}^2 + {k_y}^2)\ \zeta_{k_x,k_y}, \tag{A.7}$$

where $[J(\psi,\zeta)]_{k_x,k_y}$ and $[\beta\partial\psi\ \partial x]_{k_x,k_y}$ are the double Fourier expansion coefficients of $J(\psi,\zeta)$ and $\beta\partial\psi/\partial x$, respectively.

Noticing $\zeta = \nabla^2\psi$ so that

$$\frac{\partial \psi}{\partial x} = -ik_x\left[({k_x}^2 + {k_y}^2)\right]^{-1}\zeta_{k_x+k_y}$$

holds, and introducing the phase velocity of the Rossby wave

$$v_R(\beta,k_x,k_y) \equiv -\beta k_x\left[({k_x}^2 + {k_y}^2)\right]^{-1}$$

and

$$-\nu^* \equiv -\nu\ ({k_x}^2 + {k_y}^2),$$

Eq.(A.7) is rewritten as

$$\frac{\partial \zeta_{k_x,k_y}}{\partial t} = -\left[J(\psi,\zeta)\right]_{k_x,k_y} - iv_R(\beta,k_x,k_y)\zeta_{k_x,k_y} + F_{k_x,k_y} - \nu^*\zeta_{k_x,k_y}. \quad \text{(A.8)}$$

Now we introduce

$$\hat{\zeta}_{k_x,k_y}(t) \equiv \zeta_{k_x,k_y}(t)\ \exp[(iv_R(\beta,k_x,k_y) + \nu^*)\ t\ ], \quad \text{(A.9)}$$

then the left and right hand sides of (A.8) become

$$-\ (iv_R(\beta,k_x,k_y) + \nu^*)\ \hat{\zeta}_{k_x,k_y}\ \exp[-(iv_R(\beta,k_x,k_y) + \nu^*)\ t$$
$$+\ \frac{\partial \hat{\zeta}_{k_x,k_y}}{\partial t} \exp[-(iv_R(\beta,k_x,k_y) + \nu^*)\ t,$$

and

$$-\left[J(\psi,\zeta)\right]_{k_x,k_y} + F_{k_x,k_y}$$
$$-\ (iv_R(\beta,k_x,k_y) + \nu^*)\ \hat{\zeta}_{k_x,k_y}\ \exp[-(iv_R(\beta,k_x,k_y) + \nu^*)\ t$$

respectively. Consequently, from Eq.(A.8), we obtain

$$\frac{\partial \hat{\zeta}_{k_x,k_Y}}{\partial t} = \Big(-\left[J(\psi,\zeta)\right]_{k_x,k_y} + F_{k_x,k_y}\Big) \exp[(iv_R(\beta,k_x,k_y) + \nu^*)\ t. \quad \text{(A.10)}$$

After all, what we have to do for the time integration of Eq.(3.1) is calculating $\hat{\zeta}_{k_x,k_y}(t)$ by performing the time integration of Eq.(A.10), and obtain $\zeta_{k_x,k_y}(t)$ through Eq.(A.9) in every time step.

A.4 Convergence of the numerical calculations in §3.2

The convergence of the numerical simulations in §3.2 has been checked by performing calculations with different parameters; $\Delta t = 0.025$, which is half of the one used here; the truncation wavenumber $K_{xT} = K_{yT} = 340$ and the spatial grid points 1024×1024 which realises twice higher resolution than the original one.

Temporal developments of $x-$mean $x-$direction velocity $\overline{[u_x]}$ for the case of $k_f = 20, \beta = 20.0$ with different conditions numerical simulation are shown in Fig.A.2. Although the details of the temporal development of zonal jets are different, the general tendency, the appearance of zonal-band structure in the first stage of time integration and the realisation of an asymptotic state with two zonal jets through mergers of eastward jets and disappearances of westward jets, are common for three simulations. This suggest that these common properties are independent of conditions of numerical simulation. Note that which where is covered by an eastward jet in the asymptotic state strongly depends on the random force given to the system so that it is natural that different region is covered by an eastward jet for the different numerical simulations. In addition, as we are using double periodic condition for numerical simulation, the $y-$position of each zonal jet has no physical meaning.

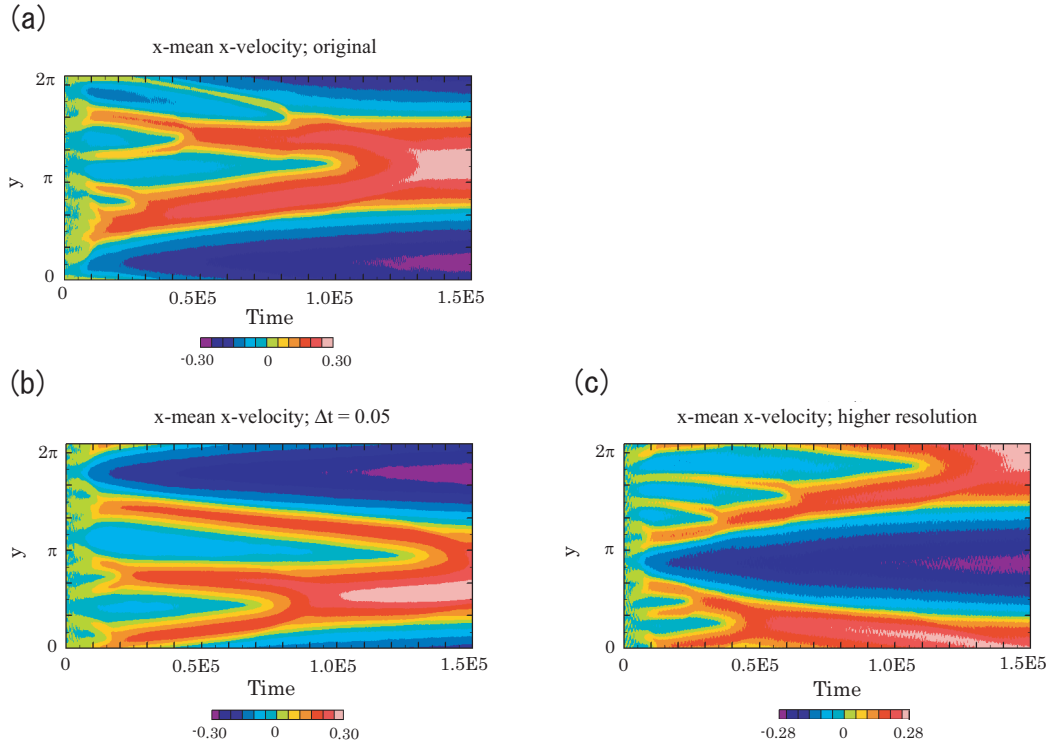

Figure A.2: Long-time development of the $x-$mean $x-$velocity $\overline{[u_x]}$ by calculations with different time step width Δt, the truncation mode numbers K_{xT}, K_{yT} and the number of spatial grid points. Rest of the parameters are $k_f = 20$, $\beta = 20.0$ and $\parallel F \parallel = 1.412 \times 10^{-2}$. (a): The original calculation. (b): $\Delta t = 0.025$, which is half of the one used in the original calculation. (c): $K_{xT} = K_{yT} = 340$ and the spatial grid points 1024×1024 which realise twice higher resolution than the original calculation.

A.5 Symmetry of the characteristic equation (3.38)

Here, we show that it is sufficient to investigate U_{0east} with $\gamma \geq 0$ to know the linear stability of all steady solutions $U_0(\eta)$. For the sake of convenience, we divide the parameter region which realises U_0 into four sectors:

$$\begin{aligned}
\mathcal{R}^{+}_{east} &\equiv \{(\gamma, U_W) \mid \gamma - 2\sqrt{6(\gamma^2+2)} < U_W < \gamma - \frac{1}{2}\sqrt{2(\gamma^2+2)},\ \gamma \geq 0\},\\
\mathcal{R}^{-}_{east} &\equiv \{(\gamma, U_W) \mid \gamma - 2\sqrt{6(\gamma^2+2)} < U_W < \gamma - \frac{1}{2}\sqrt{2(\gamma^2+2)},\ \gamma \leq 0\},\\
\mathcal{R}^{+}_{west} &\equiv \{(\gamma, U_W) \mid \gamma + 2\sqrt{6(\gamma^2+2)} > U_W > \gamma + \frac{1}{2}\sqrt{2(\gamma^2+2)},\ \gamma \geq 0\},\\
\mathcal{R}^{-}_{west} &\equiv \{(\gamma, U_W \mid \gamma + 2\sqrt{6(\gamma^2+2)} > U_W > \gamma + \frac{1}{2}\sqrt{2(\gamma^2+2)},\ \gamma \leq 0\}.
\end{aligned} \tag{A.11}$$

$\mathcal{R}^{+}_{east}$, $\mathcal{R}^{-}_{east}$, $\mathcal{R}^{+}_{west}$, and $\mathcal{R}^{-}_{west}$ correspond to U_{0east} with $\gamma \geq 0$, U_{0east} with $\gamma \leq 0$, U_{0west} with $\gamma \geq 0$, and U_{0west} with $\gamma \leq 0$ respectively.

Now, take an arbitrary combination $(\gamma, U_W) \in \mathcal{R}^{+}_{east}$, and consider $(-\gamma, U_W - 2\gamma)$, which is in the sector $\mathcal{R}^{-}_{east}$. Then, from the definitions (3.32), (3.33), (3.35b), and (3.35a), the relations

$$\begin{aligned}
U^{-}_{Eeast} &= U^{+}_{Eeast} - 2\gamma,\\
U^{-}_{Reast} &= U^{+}_{Reast} - 2\gamma,\\
a^{-}_{east} &= a^{+}_{east},\\
U^{-}_{0east} &= U^{+}_{0east} - 2\gamma,
\end{aligned} \tag{A.12}$$

hold. Subscripts $_{east}$, $^{+}$ and $^{-}$ above represent eastward jet, $\mathcal{R}^{+}_{east}$, and $\mathcal{R}^{-}_{east}$ respectively; for example, U^{-}_{Eeast} means U_E at $(-\gamma, U_W - 2\gamma) \in \mathcal{R}^{-}_{east}$. Using Eq.(A.12), the characteristic equation (3.38) for U^{-}_{0east} can be written as

$$\begin{aligned}
\sigma g &= \left[-(2-\gamma^2) + \left(2\left(U^{-}_{0east}\right)^2 - 4\gamma U^{-}_{0east}\right)\right]\frac{d^2 g}{d\eta^2} - 3\frac{d^4 g}{d\eta^4}\\
&= \left[-(2-\gamma^2) + \left(2\left(U^{+}_{0east}\right)^2 - 4\gamma U^{+}_{0east}\right)\right]\frac{d^2 g}{d\eta^2} - 3\frac{d^4 g}{d\eta^4},
\end{aligned}$$

which is the same characteristic equation for U^{+}_{0east}. Hence, investigating the stability of U^{+}_{0east} will certainly tell the stability of U_{0east}.

Next, take an arbitrary combination $(\gamma, U_W) \in \mathcal{R}^+_{east}$ again, and consider $(-\gamma, -U_W)$, which is easily show to be in the sector $\mathcal{R}^-_{west}$. Then, from the definitions (3.32), (3.33), (3.35b), and (3.35a), the relations

$$\begin{aligned} U^-_{Ewest} &= -U^+_{Reast}, \\ U^-_{Rwest} &= -U^+_{Eeast}, \\ a^-_{west} &= a^+_{east}, \\ U^-_{0west} &= -U^+_{0east} \end{aligned} \tag{A.13}$$

hold. Using Eq.(A.13), the characteristic equation (3.38) for U^-_{0west} appears to be written as

$$\begin{aligned} \sigma g &= \left[-(2-\gamma^2) + \left(2\left(U^-_{0west}\right)^2 - 4\gamma U^-_{0west}\right)\right]\frac{d^2g}{d\eta^2} - 3\frac{d^4g}{d\eta^4} \\ &= \left[-(2-\gamma^2) + \left(2\left(U^+_{0east}\right)^2 - 4\gamma U^+_{0east}\right)\right]\frac{d^2g}{d\eta^2} - 3\frac{d^4g}{d\eta^4}, \end{aligned}$$

which is the same characteristic equation for U^+_{0east}. Hence, investigating the stability of U^+_{0east} will also certainly tell the stability of U_{0west}. Consequently, it is sufficient to investigate $U_{0east} \in \mathcal{R}^+_{east}$ to know the linear stability of all the U_0.

A.6 Linear stability of an uniform flow in a Manfroi-Young model

Linear stability of a uniform flow $U = U_W$ for the Manfroi-Young equation (3.20).

Let us consider a small perturbation u to the uniform flow. Substituting the total flow $U = U_W + u$ into Eq.(3.20) and linearising the equation with respect to u yield

$$\frac{\partial u}{\partial \tau} = -(2-\gamma^2)\frac{\partial^2 u}{\partial \eta^2} - 3\frac{\partial^4 u}{\partial \eta^4} - 4\gamma U_W \frac{\partial^2 u}{\partial \eta^2} + 2U_W^2 \frac{\partial^2 u}{\partial \eta^2}.$$

If we consider the perturbation to be in the form $u = u_0 \exp(\sigma\tau + ik\eta)$, the characteristic equation

$$\sigma = k^2\left[(2-\gamma^2+4\gamma U_W - 2U_W^2) - 3k^2\right] \tag{A.14}$$

is obtained. The uniform flow $U = U_W$ is linearly stable for the set of parameters (γ, U_W) where

$$(2-\gamma^2+4\gamma U_W - 2U_W^2) - 3k^2 = 0$$

does not have $k \in \mathbb{R}$. The parameter regions where flow $U = U_W$ become linearly stable are

$$U_W \le \gamma - \frac{1}{2}\sqrt{2(\gamma^2+2)} \quad \text{or} \quad \gamma + \frac{1}{2}\sqrt{2(\gamma^2+2)} \le U_W,$$

and this is includes the parameter regions which realise one-bump steady solution U_0 ((3.28) and (3.30), shown in Fig.3.5).

Hence, the uniform flow U_W obtained from the instability of U_0 of a parameter set (γ, U_W) in an infinite domain is always linearly stable, and this may be the final state of perturbed U_0.

Acknowledgements

I would like to express my most sincere respect and gratitude to Prof. Michio Yamada., who has supported me in both academic and personal matters throughout my studentship at Kyoto University. He has not only introduced me to the important ideas and technique of nonlinear science but also taught me how to see the world in an academic way.

I am also deeply grateful to Prof. Shin-ichi Takehiro for guiding me with great attentiveness and patience. I have derived much inspiration from his approaches to research problems.

Dr Yoshitaka Saiki and Dr Miki U. Kobayashi have given me valuable comments on my research project. I would also like to thank my colleagues at the Research Institute for Mathematical Science, Masanobu Inubushi, Keiji Kimura, Eiichi Sasaki, and Kenta Ishimoto, for fruitful discussions.

My special thanks go to my friends and families, who have always supported me during my university life.

Lastly, I am grateful to the RIMS for providing me a stimulating and brilliant research environment. I sincerely treasure the experience of working in this wonderful institute. I will always be proud of having been a member of the RIMS.

Some of the data analyses and the visualisations in this thesis were done with the ISPACK (http://www.gfd-dennou.org/library/ispack/), gt4f90io (http://www.gfd-dennou.org/libgary/gtool/), spmodel [27] (http://www.gfd-dennou.org/library/spmodel/) and the software products of the GFD Dennou Ruby project (http://ruby.gfd-dennou.org/). The numerical calculations were performed by the computer systems of the Institute for Information Management and Communication (IIMC) of Kyoto University and of the Research Institute for Mathematical Sciences, Kyoto University.

References

[1] F. H. Busse, "A simple model of convection in the Jovian atmosphere," *Icarus*, **29** (1976) 255-260

[2] Z-P. Sun, G. Schubert, and G. A. Glatzmaier, "Banded Surface Flow Maintained by Convection in a Model of the Rapidly Rotating Giant Planets," *Science*, **260** (1993) 661-664

[3] M. Heimpel, J. Aurnou, and J. Wicht, "Simulation of equatorial and high-latitude jets on Jupiter in a deep convection model," *Nature*, **438** (2005) 193-196

[4] P. B. Rhines, "Waves and on a beta-plane," *J. Fluid Mech.*, **69** (1975) 417-443

[5] R. K. Kraichnan, "Inertial ranges in two-dimensional turbulence," *Phys. Fluids*, **10** (1967) 1417-1423

[6] G. K. Vallis and M. E. Maltrud, "Generation of mean flows and jets on a beta plane and over topography," *J. Phys. Oceanogr.*, **23**, (1993) 1346-1362

[7] G. P. Williams, "Planetary circulations:1. barotropic representation of Jovian and Terrestrial turbulence, " *J. Atmos. Sci.*, **35**, (1978) 1399-1426

[8] A. Chekhlov, S. A. Orszag, S. Sukoriansky, B. Galperin, and I. Staroselsky, "The effect of small-scale forcing on large-scale structures in two-dimensional flows," *Physica D*, **98**, (1996) 321-334

[9] H-P. Huang and W. A. Robinson, "Two-dimensional turbulence and persistent zonal jets in a global barotropic model," *J. Atmos. Sci.* **55**, (1998) 611-632

[10] A. M. Balk, "Angular distribution of Rossby wave energy," *Phys. Lett. A*, **345**, (2005)

[11] S. Yoden and M. Yamada, "A Numerical experiment on two-Dimensional Decaying turbulence on a rotating sphere," *J. Atmos. Sci.*, **50**, (1993) 631-643

[12] S. Takehiro, M. Yamada, and Y. Hayashi, "Energy accumulation in easterly circumpolar jets generated by two-dimensional barotropic decaying turbulence on a rapidly rotating sphere," *J. Atmos. Sci.*, **64**, (2007)

[13] T. Nozawa and S. Yoden, "Formation of zonal band structure in forced two-dimensional turbulence on a rotating sphere," *Phys. Fluids*, **9**, (1997) 2081-2093

[14] H-P. Huang, B. Galoerin, and S. Sukoriansky, "Anisotropic spectra in two-dimensional turbulence on the surface of a rotating sphere," *Phys. Fluids* **13**, (2001) 225-240

[15] K. Obuse, Takehiro S., and M. Yamada, "Long-time asymptotic states of forced two-dimensional barotropic incompressible flows on a rotating sphere," *Phys. Fluids.*, **22** (2010) 156601

[16] A. J. Manfroi, W. R. Young, " Slow evolution of zonal jets on the beta plane," *J. Atmos. Sci.*, **56**, (1999) 784-800

[17] J. W. Cahn, J. E. Hilliard, "Free energy of a nonuniform system. I. interfacial free energy," *J. Chem. Phys.*, **28** (1958) 258-267

[18] I. Silberman, "Planetary waves in the atmosphere," *J. Meteor.* **11**, 27 (1953) 27-34

[19] S-I. Ei, "The motion of weakly interacting pulses in reaction-diffusion systems," *J. Dynam. Diff. Eqs.*, **14** (2002) 85-137

[20] J. S. Langer, "Theory of spinodal decomposition in alloys," *Annals of Physics*, **65** (1971) 53-86

[21] A. Novick-Cohen, L. A. Segel, "Nonlinear Aspects of the Cahn-Hilliard equation," *Physica D*, **10**, (1984) 277-298

[22] D. Bettinson, G. Rowlands, "Stability of the one-dimensional kink solution to a general Cahn-Hilliard equation," *Phys. Rev. E.*, **54** (1996) 6102-6108

[23] M. Argentina, M. G. Clerc, R. Rojas, E. Tirapegui, "Coarsening dynamics of the one-dimensional Cahn-Hilliard model," *Phys. Rev. E.*, **71** (2005) 046210

[24] S. Villain-Guillot, "1D Cahn-Hilliard equation: Ostward ripening and modulated phase s," *IJBC* , **10** (2009) 3541-3552

[25] K. Obuse, Takehiro S., and M. Yamada "Linear stability of steady zonal jet flows induced by a small-scale forcing on a β plane," *Physica D*, **240** (2011) 1825-1834

[26] L. D. Landau, E. M. Lifshitz, Quantum mechanics: non-relativistic theory, third ed., Oxford, Pergamon Press, 1977 pp. 73-74

[27] S. Takehiro, Odaka, M., Ishioka, K., Ishiwatari, M., Hayashi Y.-Y., and SPMODEL Development Group, "A series of hierarchical spectral models for geophysical fluid dynamics," *Nagare Multimedia* (2006) Available on-line at: http://www.nagare.or.jp/mm/2006/spmodel/